



Technische Universität München

TUM School of Engineering and Design

**Parallel Configuration of Battery Cells:
Determining Influencing Factors of an Inhomogeneous Current
Distribution**

Philipp Jocher, M.Sc.

Vollständiger Abdruck der von der TUM School of Engineering and Design der Technischen Universität München zur Erlangung eines

Doktors der Ingenieurwissenschaften (Dr.-Ing.)

genehmigten Dissertation.

Vorsitz: Prof. Dr.-Ing. Hans-Georg Herzog
Prüfende der Dissertation: 1. Prof. Dr.-Ing. Andreas Jossen
2. Prof. Dr.-Ing. Jan Philipp Schmidt

Die Dissertation wurde am 22.04.2024 bei der Technischen Universität München eingereicht und durch die TUM School of Engineering and Design am 20.08.2024 angenommen.

Abstract

In a battery system, up to several hundred cells are interconnected to provide the required energy and performance. The behavior of each component in the system is of interest to achieve a long energy storage life. Most scientific studies are carried out at individual cell level to quantify their influencing variables. Meanwhile, the current can be distributed unevenly between the cells in parallel configurations. Understanding the factors influencing current distribution is essential for profoundly understanding battery system behavior.

A battery management system usually monitors the cell voltages in serial-connected cells. In contrast, in parallel-connected cells, each cell would require a current sensor to measure the current. As this would lead to high costs, monitoring each cell current is generally not realized. Instead, different methods are used in studies to quantify the factors leading to a homogeneous or an inhomogeneous current distribution. The aim is to identify parameters that lead to convergent or divergent behavior across the cells connected in parallel.

This work presents three studies that aim to analyze the behavior of battery systems. The first study quantifies the factors that influence the measurement of electrical contacts. A simulation- and mathematically-based analysis was used to identify inhomogeneities in the electrical measurement that affect its accuracy and validity. Based on this, the distribution of the current in area-based connections was investigated. This knowledge can be used to optimize the design of electrical connections from an electrical point of view. Consequently, electrically conductive adhesives are analyzed alongside well-established joining techniques. In a quantitative comparison with well-established joining techniques, the mechanical and electrical parameters show the same order of magnitude. Regarding economic considerations, however, adhesive connections cannot keep up with well-established joining techniques.

A second study presents a novel measurement technique to virtually connect cells in parallel with defined boundary conditions. This makes it possible to measure the current distribution between battery cells without the influence of parasitic elements such as contacts and measuring equipment. Using the novel measurement method, clearly defined boundary conditions could be investigated, such as different contact resistances and cell temperatures between cells connected in parallel.

In a final study, these influencing factors are quantified for three different state-of-the-art cells. To facilitate comparability among the three cell technologies, sensitivity factors are introduced, which measure how sensitive the current distribution of the respective cell technology reacts to the imposed inhomogeneities. It was concluded that the current distribution mainly depends on the open-circuit voltage characteristic, the temperature sensitivity and the resistance of the corresponding cell technology.

Kurzfassung

In Batteriesystemen werden bis zu mehreren hundert Zellen miteinander verschalten um die geforderte Energie und Leistung erbringen zu können. Das Verhalten eines jedes Komponentes im System ist dabei von Interesse, um eine möglichst langlebigen Energisepeicher zu erhalten. Die meisten wissenschaftlichen Studien werden dabei auf Einzelzellebene durchgeführt, um deren Einflussgrößen zu quantifizieren. In der Parallelschaltung hingegen, kann sich der Strom ungleichmäßig auf die Zellen aufteilen. Die Kenntnis der Einflussfaktoren für eine inhomogene Stromaufteilung hierfür essential, um ein tiefgründiges Verständnis von Batteriesystemen zu erhalten.

Während die Zellspannungen einer Serienschaltung in der Praxis vom Batteriemanagementsystem aufgezeichnet wird und somit überwacht werden kann, ist eine Strommessung in jedem parallelen Pfad aufgrund vom hohen Aufwand und Kosten in der Regel nicht möglich. Anstattdessen wird mittels Testverbänden nach neuen Methoden gesucht, um die Faktoren zu quantifizieren, welche in eine homogenen sowie inhomogenen Stromaufteilung resultieren. Das Hauptziel ist die Identifikation von Kenngrößen, welche eine Konvergenz oder Divergenz über die parallel geschalteten Zellen hervorrufen können.

Diese Arbeit zielt im Rahmen von drei Studien darauf ab, das Verhalten von parallelen Batteriesystemen zu analysieren. In einer ersten Studie werden die Einflussfaktoren hinsichtlich der Messung von elektrischen Kontaktwiderständen quantifiziert. Durch eine simulations- und mathematisch basierte Analyse konnten Inhomogenitäten auf die elektrische Messung identifiziert werden, welche die Messgenauigkeit sowie deren Aussagekraft beeinträchtigen können. Es wurde die Stromaufteilung in flächenbasierten Verbindungen untersucht, welche sich in Abhängigkeit der Widerstände inhomogen über die Fläche aufteilen kann. Dieses Wissen kann genutzt werden, um elektrische Verbindungen aus elektrischer Sicht optimiert auslegen zu können. Darauf aufbauend werden neben konventionellen Kontaktierungsarten, elektrische Klebeverbindungen analysiert. Im quantitativen Vergleich mit den konventionellen Kontaktierungsarten zeigen die mechanischen sowie die elektrischen Parameter die gleiche Größenordnung. Aus ökonomischer Sicht hingegen können Klebeverbindungen mit herkömmlichen Verbindungsmethoden nicht konkurrieren.

Im Anschluss wird eine neue Messmethode zur Vermessung der Stromaufteilung in parallel geschalteten Zellen vorgestellt. Diese ermöglicht es, die Stromaufteilung in Batteriezellen zu messen, ohne einen Einfluss von parasitären Elementen wie Kontaktierungen und Messequipment. Mittels der neuen Messmethode konnten eindeutig definierte Randbedingungen wie unterschiedliche Kontaktwiderstände sowie Zelltemperaturen zwischen parallel geschalteten Zellen untersucht werden.

In einer abschließenden Studie werden diese Einflussfaktoren anhand von drei kommerziellen Zelltechnologien analysiert. Um Vergleichbarkeit zwischen den drei Zelltechnologien zu schaffen, werden Sensitivitätsfaktoren eingeführt. Diese quantifizieren, wie sensibel die Stromverteilung der jeweiligen Zelltechnologie auf die aufgeprägten Inhomogenitäten reagiert. Es konnte gezeigt werden, dass die Stromaufteilung dabei hauptsächlich von der Ruhespannungskennlinie, der Temperatursensitivität sowie des Widerstandes der Zelltechnologie abhängig ist.

Contents

Abstract	c
Kurzfassung	e
List of Publications	III
Abbreviations	V
1 Introduction	1
1.1 Scope and Outline	3
2 Fundamentals and Methodology	7
2.1 Fundamentals of Battery Systems	8
2.1.1 Electrical Boundaries	9
2.1.2 Thermal Boundaries	10
2.2 Fundamentals of the Current Distribution within a Parallel Battery System	11
2.2.1 Intrinsic Causes for an Inhomogeneous Current Distribution	12
2.2.2 External Causes for an Inhomogeneous Current Distribution	14
2.3 State of the Art of Electrical Contact Resistances and the Measurement of the Current Distribution	15
2.3.1 Electrical Contact Resistances	15
2.3.2 Measurement of the Current Distribution	16
2.4 Developed Methods	19
2.4.1 Measurement of Electrical Low-Contact-Resistances	19
2.4.2 Virtual Parallel Connection	25
3 Measurement and Determination of the Contact Resistance of Planar Contacts	29
4 A Novel Measurement Technique for Parallel-Connected Battery Cells	61
5 Comparing Lithium-Ion and Sodium-Ion Technologies in Parallel Configuration by Sensitivity Factors	75
6 Conclusion	93
References	95
List of Figures	109
List of Tables	111

List of Publications

Peer-reviewed journal paper contributions (lead author)

- a **Jocher, P.**; Steinhardt, M.; Ludwig, S.; Schindler, M.; Jonathan, M.; Jossen, A.: *A novel measurement technique for parallel-connected lithium-ion cells with controllable interconnection resistance*, in: *Journal of Power Sources* 503 (2021) 230030, doi.org/10.1016/j.jpowsour.2021.230030, 2021
- b **Jocher, P.**; Kick, K.M.; Rubio Gomez, M.; Himmelreich, A.V.; Gruendl, A.; Hoover, E.; Zaeh, M.F.; Jossen, A.: *Determination of the Contact Resistance of Planar Contacts: Electrically Conductive Adhesives in Battery Cell Connections*, in: *Batteries* 2023, 9, 443, doi.org/10.3390/batteries9090443, 2023
- c **Jocher, P.**; Roehrer, F.; Rehm, M.; Idrizi, T.; Himmelreich, A.; Jossen, A.: *Scaling from Cell to System: Comparing Lithium-ion and Sodium-ion Technologies Regarding Inhomogeneous Resistance and Temperature in Parallel Configuration by Sensitivity Factors*, in: *Journal of Energy Storage* 98 (2024) 112931, https://doi.org/10.1016/j.est.2024.112931, 2024

Self-written sections of peer-reviewed lead author journal paper contributions are partially contained in this doctoral thesis without further reference in the text.

Selection of conference contributions

- a **Jocher, P.**; Steinhardt, M.; Ludwig, S.; Schindler, M.; Jonathan, M.; Jossen, A.: *Experimental Validation of Parallel-Connected Lithium-Ion Cells with Controllable Interconnection Resistance*, in: *Advanced Battery Power - Kraftwerk Batterie 2021*, poster [online], 2021
- b **Jocher, P.**; Steinhardt, M.; Ludwig, S.; Schindler, M.; Jonathan, M.; Jossen, A.: *A Novel Measurement Technique for Parallel-Connected Lithium-Ion Cells with Controllable Interconnection Resistance.*, in: *241st ECS Meeting*, Vancouver, lecture, 2022
- c **Jocher, P.**; Roehrer, F.; Rehm, F.; Idrizi, T.; Himmelreich, A.; Jossen, A.: *Strengths and Challenges of Sodium-Ion and Lithium-Ion Technology Regarding Scaling from Cell to System*, in: *Batterieforum Deutschland*, Berlin, poster and lecture, 2024

Peer-reviewed journal paper contributions (co-author)

- a Schindler, M.; Durdel, A.; Sturm, J.; **Jocher, P.**; Jossen, A.: *On the Impact of Internal Cross-Linking and Connection Properties on the Current Distribution in Lithium-Ion Battery Modules*, in: *Journal of The Electrochemical Society*, 2020 167, doi.org/10.1149/1945-7111/abad6b, 2020
- b Schindler, M.; **Jocher, P.**; Durdel, A.; Jossen, A.: *Analyzing the Aging Behavior of Lithium-Ion Cells Connected in Parallel Considering Varying Charging Profiles and Initial Cell-to-Cell Variations*, in: *Journal of The Electrochemical Society*, 2021 168, doi.org/10.1149/1945-7111/ac2089, 2021

Abbreviations

Please note that the list below is based on the main part of this thesis and does not fully cover the abbreviations used in the papers.

R_C	electrical contact resistance
np	n parallel
$2p$	two parallel
BEV	battery electric vehicles
BMS	battery management system
BTMS	battery thermal management system
CC	constant current
ECA	electrically conductive adhesives
ECM	electrical circuit model
EP	external parallel connection
EV	electric vehicle
FEM	finite element method
IP	internal parallel connection
LCO	lithium cobalt oxide
LFP	lithium iron phosphate
LIB	lithium-ion battery
NCA	nickel cobalt aluminium oxide
NMC	nickel manganese cobalt oxide
OCV	open-circuit-voltage
PHEV	plug-in hybrid electric vehicles
SIB	sodium-ion battery
SoC	state-of-charge
SoH	state-of-health
UTF	ultimate tensile force
VPC	virtual parallel connection

1 Introduction

In the 19th century, the first battery electric vehicles (BEV) were introduced [1]. While in the 20th century, particularly petrol and diesel vehicles dominated the market, the sale of battery-powered electric vehicles (EVs) has increased significantly since the 2010s, see Figure 1.1 a). This is primarily due to three major drivers: decreasing battery costs and increasing energy density, government policies, and the so-called Tesla effect [2]. Since its commercialization in the early 1990s, the lithium-ion battery (LIB) is now the state-of-the-art technology; due to its high energy and power density, it is used in many applications, as EV and stationary electrical energy storage [3; 4]; to achieve emission goals, governments try to increase the EV sales [5]; especially, Tesla managed to change the image of EV through high performance and aesthetics [6]. Figure 1.1 represents the share of sales of new EV. In

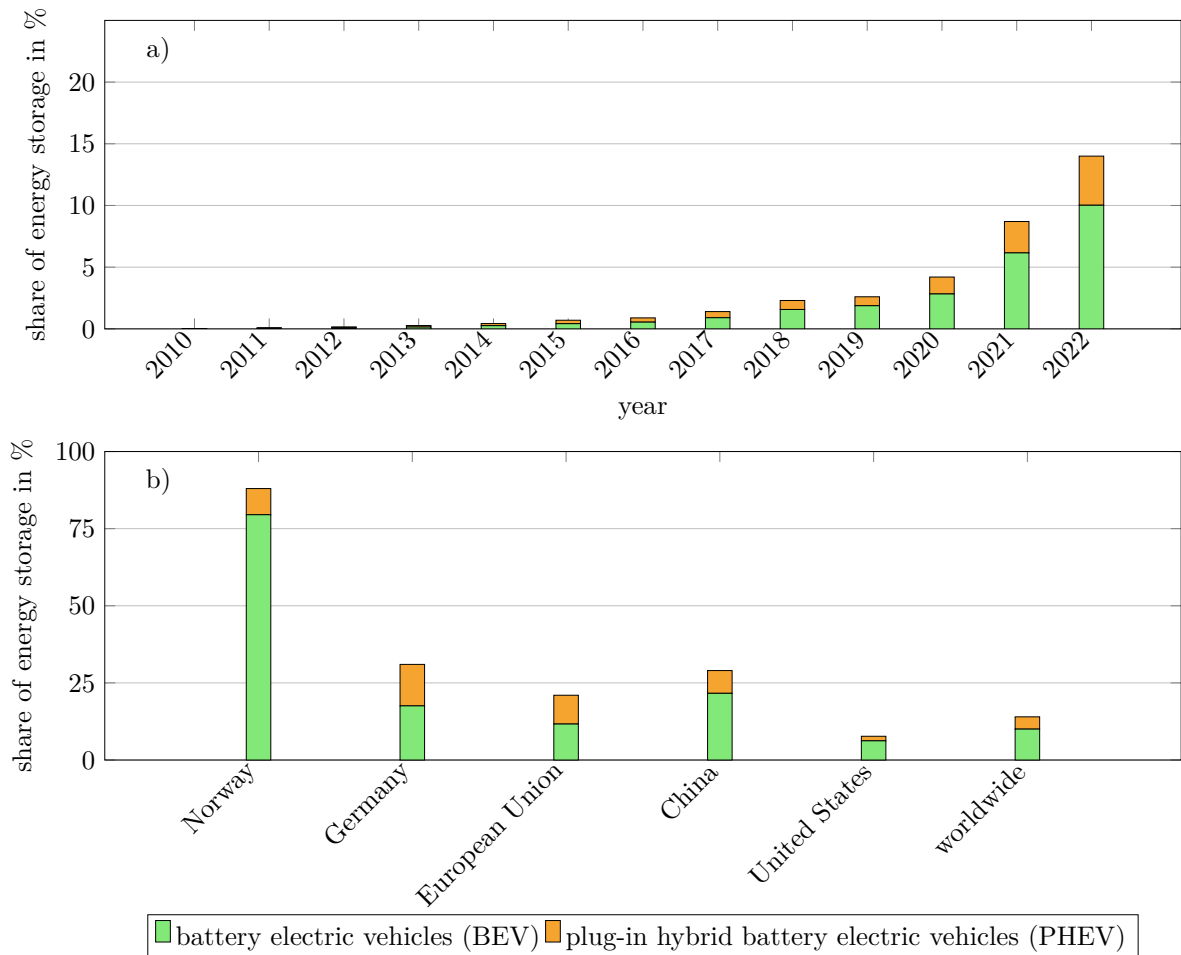


Figure 1.1: Share of sales of new passenger vehicles according to the electrical energy sources. a) worldwide sales between 2010 and 2022. b) vehicle sales in Norway, Germany, the European Union, China, the United States, and worldwide for 2022. Data based on [7].

particular, Figure 1.1 a) shows the worldwide sales of new EV from 2010 to 2022. In 2022, global

sales of plug-in hybrid electric vehicles (PHEV) and BEV reached almost 14%. In this context, the proportion of BEV has grown significantly, from just under 3% in 2020 to over 6% in 2021 and more than 10% in 2022. Figure 1.1 b) represents the vehicle sales in Norway, Germany, the European Union, China, the United States, and worldwide for 2022. Among all regions, regional differences are visible. Whereas in the United States BEV currently contributes only to 6%, and in Germany with 18%, in Norway already a share over 79% of BEV is reached.

Recently, Peng et al. [8] presented a comparative study of the EV market share in the European Union and the United States. Regional differences and similarities were investigated by using statistical and spatial models. Several factors, such as charging infrastructure, age, income, and level of education play a role in the acceptance of EV. Targeted political measures, such as affordability and accessibility, are of high priority. [8] As the sales of EV is developing differently in different regions, the expansion has great potential.

Batteries play an important role in many applications. Cells are connected in a battery system to provide the required power and energy for consumer electronics, mobility, and stationary applications. By comparing the worldwide battery demand between 2020 and a prognosis of up to 2030, the share of the mobility sector plays a crucial role. Figure 1.2 shows a mobility share of over 70% in 2023 and over 85% in 2030.

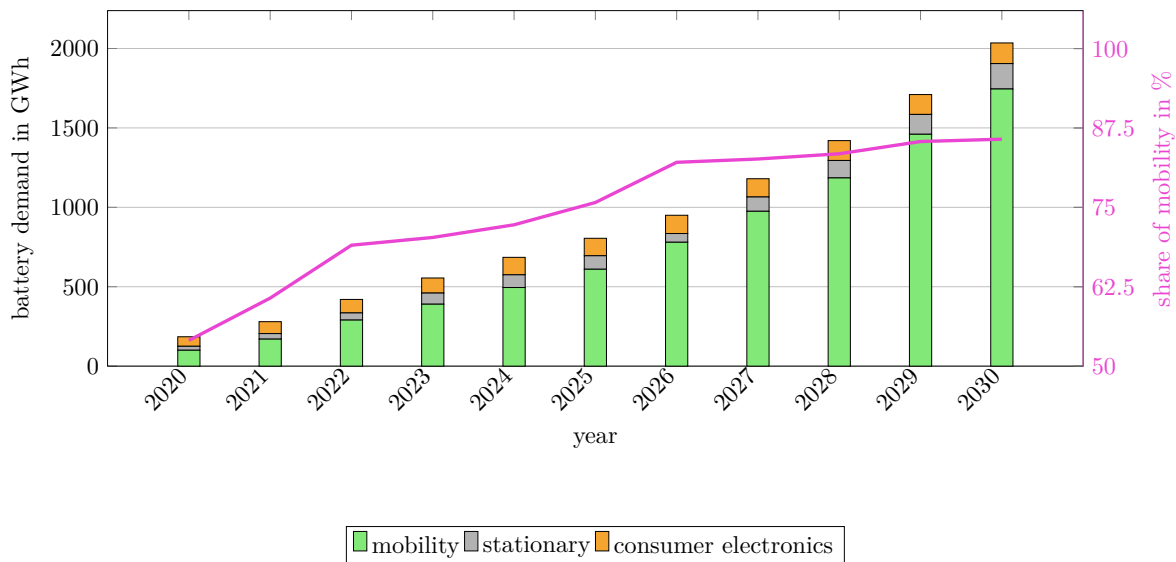


Figure 1.2: Worldwide battery demand and mobility share between 2020 and a prognosis up to 2030. Data based on [9].

Based on the data of [9], the overall energy demand for batteries will rise. In addition to the increased demand for energy, more efficient and powerful batteries are of interest. Understanding and optimizing each component of the battery system is therefore essential.

The number of cells in a battery pack can differ depending on the application; they can be connected in different ways to achieve the required voltage and energy. Additionally, a variety of cell chemistries, formats, and capacities can be used. For example, the first generation Nissan Leaf 24 kWh battery pack consists of 33 Ah pouch cells in 96s2p configuration. In comparison, highly parallelized battery packs are used in Tesla EVs. The Model S 85 kWh uses a 74s96p configuration. [10] Whereas Tesla uses cylindrical cells with nickel cobalt aluminium oxide (NCA) or lithium iron phosphate (LFP) cathode material [11], BYD focuses on blade battery design with LFP chemistry as cathode material [12]. In

addition, in China, the first EV with sodium-ion battery (SIB) cell technology was presented [13]. Therefore, various approaches are used to design the energy storage system.

A battery system is a system of interrelated subsystems. It consists of electrical contacting, cells, a battery thermal management system (BTMS), and a battery management system (BMS). To understand the system's behavior, it is essential to understand the individual components. Numerous scientific studies are being carried out to achieve this. With an accurate determination of electrical contact resistance, various joining technologies are compared against one another. In addition, the behavior of different cell technologies in battery systems is of interest. In particular, the factors that influence homogeneous aging across the whole battery system. The existing research examines well-established joining techniques and factors such as cell variance, the number of cells, and their topology and chemistry combinations on the system behavior through simulation and experimental studies. Moreover, it investigates the temperature behavior, including the optimal cell temperature and the influence of temperature gradients. This work extends the current literature and provides insight into accurately determining electrical contact resistance. In addition, the sensitivity against resistance and temperature of three cell technologies will be examined.

1.1 Scope and Outline

This work investigates the behavior of parallel-connected battery cells, focusing on cell connections and their current distribution. The research addresses the factors influencing the experimental measurement and the current distribution within an electrical connection. Understanding the current distribution within an electrical connection allows for the optimization of the design from an electrical point of view. Furthermore, the study compares different types of interconnections, considering their electrical, mechanical, and economic properties. Based on this, the impact of an inhomogeneous contact resistance and an inhomogeneous path temperature on various cell technologies is investigated by measuring the current distribution. This leads to the following research questions:

- Q1 How can electric contact resistance be measured accurately?*
- Q2 Is there an optimal design for cell connections to minimize electrical contact resistance?*
- Q3 Which resistances result from electrically conductive adhesives (ECA) in comparison to well-established joining techniques?*
- Q4 How can the current distribution be measured efficiently in the presence of inhomogeneous contact resistances and path temperature?*
- Q5 How does an inhomogeneous contact resistance or path temperature influence the system performance in a parallel configuration?*

This thesis is structured into the following chapters to answer these five central questions. Figure 1.3 gives a general overview of the structure.

Chapter 1 gives an overview of the topic.

Fundamentals of the battery system are included in chapter 2. After defining the electrical and thermal boundaries, the state-of-the-art electrical joining techniques and the measurement of the current distribution are discussed. This is followed by the methodology to determine the electrical contact resistance of area-based connections. Further, the influence of the current injection is presented. Finally, a novel measurement technique, the virtual parallel connection (VPC), is introduced to measure the

current distribution of parallel-connected battery cells.

Chapter 3 consists of the research paper “Determination of the Contact Resistance of Planar Contacts: Electrically Conductive Adhesives in Battery Cell Connections” [14]. First, the factors that influence the measurement will be discussed. After defining a methodology for determining planar contacts, ECA are compared with conventional joining techniques. The research questions Q1, Q2 and Q3 will be addressed.

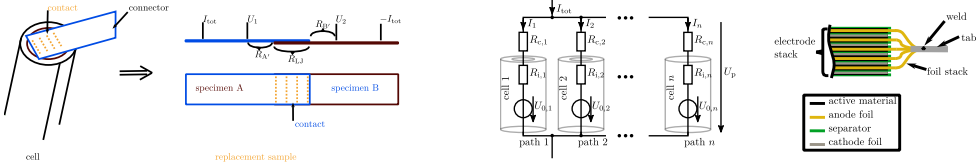
Chapter 4 addresses research question Q4. The paper “A novel measurement technique for parallel-connected lithium-ion cells with controllable interconnection resistance” [15] presents a concept and a validation using a conventional test-bench. Within the novel method, influencing factors such as inhomogeneous contact resistance, as presented in Chapter 3, and inhomogeneous path temperatures can now be investigated in parallel connection.

Finally, research question Q5 is discussed in chapter 5. This part is based on the two previously mentioned publications. An inhomogeneous contact resistance and path temperature in a two parallel (2p) configuration are investigated for LIB and SIB cell technologies. The paper “Scaling from cell to system: Comparing Lithium-ion and Sodium-ion technologies regarding inhomogeneous resistance and temperature in parallel configuration by sensitivity factors” [16] is representing it.

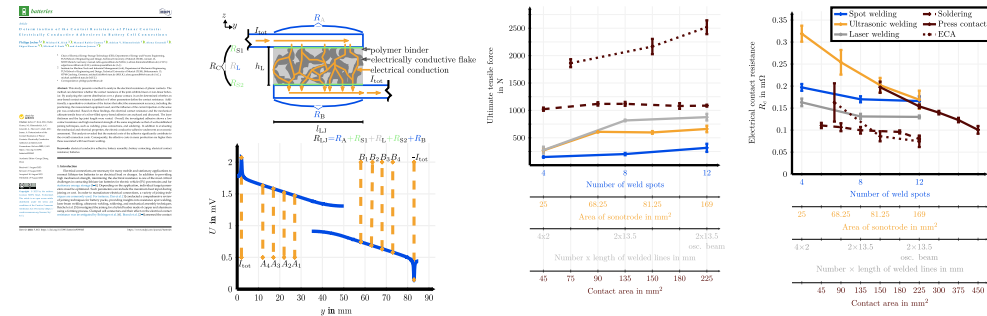
Finally, Chapter 6 concludes the main findings of this work and gives an outlook.

Chapter 1: Introduction

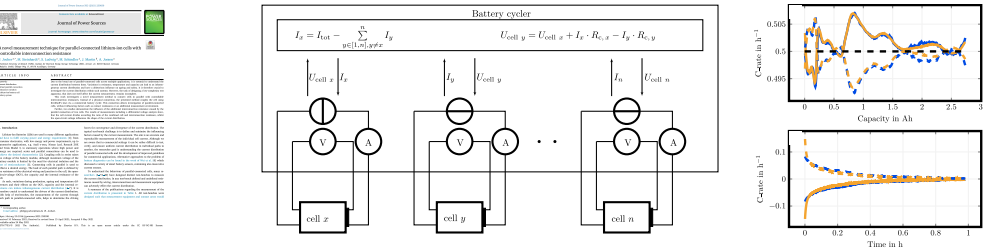
Chapter 2: Fundamentals and Methodology



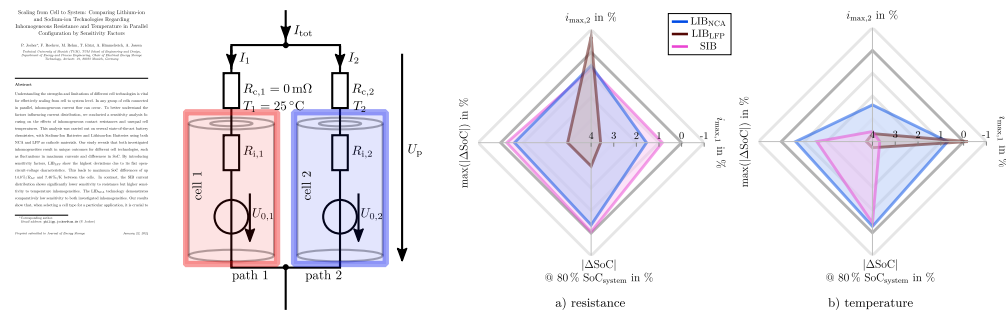
Chapter 3: Measurement and Determination of the Contact Resistance of Planar Contacts



Chapter 4: A Novel Measurement Technique for Parallel-Connected Battery Cells



Chapter 5: Comparing Lithium-Ion and Sodium-Ion Technologies in Parallel Configuration by Sensitivity Factors



Chapter 6: Conclusion and Outlook

Figure 1.3: Structure and overview of this thesis.

2 Fundamentals and Methodology

This chapter focuses on the fundamentals of a battery system. Commencing with an overview on electrical and thermal boundary conditions in Chapter 2.1. Chapter 2.2 goes on to discuss these variables in parallel connections. Special attention is drawn to the intrinsic and external factors influencing the current distribution. Based on a literature research of the electrical contact resistance and the measurement techniques of the current distribution as shown in Chapter 2.3, Chapter 2.4 presents the developed methods to measure electrical resistances and the current distribution. In particular, the influence of inhomogeneities, the determination of area-based electrical contact resistances, and the methodology of the VPC are discussed.

The main part of the battery system consists of the battery cell. In this thesis, as depicted in Figure 2.1 a), each battery cell is represented in a simplified manner by a voltage source and an internal resistance, denoted as U_0 and R_i respectively. The voltage source, U_0 , represents the cell voltage, which is defined as the voltage difference between the cathode and the anode. This difference depends on the degree of lithiation within both electrodes and therefore, determines the cells state-of-charge (SoC). Specific anode and cathode materials characterize various cell parameters. Such as the energy and power density and the voltage range of the cell. [17]

The open-circuit-voltage (OCV) is an internal voltage of the cell. It can be measured at the cell's terminals after a certain rest period, specifically when all internal processes have reached equilibrium. However, under non-equilibrium conditions and a current flow, $I_{\text{load}} \neq 0$, the measured voltage, $U_{\text{cell},x}$, is the sum of the internal cell voltage, $U_{0,x}$, and the overpotentials. Overpotentials result due to internal cell processes under current flow and can be expressed by time-dependent resistances. In a cell, these include the ohmic overpotential U_{Ω} , the charge transfer overpotential, U_{CT} , and the diffusive overpotential, U_{diff} . [18–20] The ohmic overpotential occurs instantaneously and depends on R_{Ω} and I_{load} . It is present at the current collector, the active material, and the electrolyte. [21] Charge transfer overpotential, which is caused by electrons being transferred to ions, can be described with the Butler-Volmer equation within a time range from milliseconds to one second [22]. The diffusion overpotential describes the diffusion of ions in the liquid and solid-phase and is dominant at time constants of > 1 s [23].

Therefore, the total overpotential can be described as the difference of OCV to the measured cell voltage, $U_{\text{cell},x}$. This can be represented in a current- and time-dependent cell resistance, which is denoted by R_i in this thesis. It is, therefore, important to specify the operation point of the resistance determination. In this thesis the R_{AC} is measured at a current amplitude of 140 mA and a frequency of $f = 1$ kHz, and the R_{DC} is measured after a $0.67C$ current pulse of $t = 10$ s.

In summary, overpotentials describe how well electrochemical processes take place within a cell. The lower the overpotential, the better the charging and discharging performance.

Besides the cell's intrinsic parameters, the system's performance can be influenced by temperature and contact resistance. In this work, a distinction between parameters and influencing factors is made. Internal parameters refer to the parameters of the cell, while external parameters refer to the

contacting between cells. Influencing factors are boundary conditions, such as the temperature. They can influence both internal and external parameters.

In this work four different cell technologies are investigated, including three LIBs with differing cathode chemistries, nickel manganese cobalt oxide (NMC), NCA and LFP, and a SIB with layered oxide as cathode material. Table 2.1 summarizes the specific cell data, either taken from data sheets or measured at 25 °C.

Table 2.1: Specifications of the investigated cells. The measurements were carried out at 25 °C; resistance measurements were taken at 50 % SoC.

Parameter	Symbol	LIB _{NMC}	LIB _{NCA}	LIB _{LFP}	SIB
Identifier ^{a)}	-	INR18650-MJ1	INR18650-35E	HDCF18650-1800	NA18650-1250
Manufacturer ^{a)}	-	LG Chem	Samsung SDI	HAIDI Energy Group	Shenzhen Mushang
Format ^{a)}	-	18650	18650	18650	18650
Weight ^{b)} in g	-	47	48.6	41.9	37.2
Nominal capacity in Ah ^{a)}	C_N	3.35	3.35	1.80	1.25
Nominal voltage in V ^{a)}	V_N	3.635	3.6	3.2	3.0
Lower voltage limit in V ^{a)}	$U_{\text{discharge}}$	2.5	2.65	2	1.5
Upper voltage limit in V ^{a)}	U_{charge}	4.2	4.2	3.65	3.8
$Z_{AC, Z_{\text{Im}=0}}$ in m Ω ^{b)}	R_{AC}	28.4	20.2	27.9	25.4
$R_{DC, 10s}$ in m Ω ^{b)}	R_{DC}	32.9	37.12	58.4	84.99
nominal volumetric energy in Wh/l ^{a)}	-	736.2	729.1	348.2	226.7
nominal gravimetric energy in Wh/kg ^{a)}	-	259.1	248.1	137.5	100.8

^{a)} data extracted from datasheet ^{b)} measured data

2.1 Fundamentals of Battery Systems

Battery systems are defined as the combination of cells via electrical connections. They are commonly denoted with the following notation, $ms\ np$, where m represents the number of cells connected in series and n represents the cells connected in parallel.

Various types of cell formats such as pouch, cylindrical and prismatic exist. The cell format influence the design of the battery system [24]. Kerler [25] presented an electrical, thermal, cost and safety-based method to determine the optimal battery cell size for electric vehicles. There, the optimal battery cell format and size are defined by distinct boundary conditions and vary for each application [25]. Several different assembly strategies exist, for example small cells with a high number of parallel-connected cells, e.g., Tesla Model S, or large-size prismatic or pouch cells with no or few parallel connections e.g., BMW i3 and Nissan Leaf [26].

In a battery system, cells are traditionally connected into modules, which in turn can be connected in series to form a pack [27]. The module level is used to provide a lower voltage for manufacturing purposes and to control mechanical stability [28]. Recently, the cylindrical format, with an increased diameter of 46 mm, has been recognized as the new standard for cells in the automotive sector [29]. Due to the high mechanical stability of the cylindrical cell format, the cell-to-pack approach is being pursued. This bypasses the module and allows a higher energy density of the system. [30]

There are three important interactions need to be considered in a battery system, the electrical, thermal and mechanical interaction between cells, which have an influence on the system's behavior. This thesis focuses on the electrical and thermal influences on the system's behavior, which will be explained in the following chapters.

2.1.1 Electrical Boundaries

To achieve the desired energy and power for different applications, cells are connected in series and parallel. Connecting cells in series, results in a voltage increase of the system. The sum of all in series connected cell voltages defines the system voltage, see Equation 2.1.

$$U_{\text{serial}} = \sum_{s=1}^m U_s \quad (2.1)$$

Today, EVs are commonly based on a 400 V system, however, manufacturers are beginning to shift to a 800 V system [31]. Equation 2.2 shows the relationship between current, voltage and charging time.

$$E_{\text{charge}} = P_{\text{charge}} \cdot t_{\text{charge}} = U_{\text{charge}} \cdot I_{\text{charge}} \cdot t_{\text{charge}} \quad (2.2)$$

Consequently, increasing the voltage can reduce the current to reach the same power. This results in a reduction of ohmic losses, $I^2 \cdot R$, and an increase of electromagnetic compatibility at high switching frequencies, which increases the performance. Furthermore, the current is the same through all cells in a serial connection. A disadvantage of serial connections is the system's capacity, which is defined by the minimum cell capacity over all cells, see Equation 2.3.

$$C_{\text{serial}} = \min_{s=1 \dots m} (C_s) \quad (2.3)$$

Additionally, battery packs with a higher voltage require better insulation and more spacing between components [32].

In contrast to the serial connection, cells connected in parallel result in an increase of capacity. This can be achieved by two means: first, a higher number of cells can be connected in parallel, and second, larger cells with higher capacity content can be used. Figure 2.1 shows the external parallel connection (EP) and the internal parallel connection (IP). The EP is represented exemplarily with cylindrical cells. The contact resistance, $R_{c,x}$, represents the combined resistances from the cell to the terminal of path x , $x \in 1, n$. The IP is represented by a pouch cell. There, each layer consists of a cathode and anode foil, each double-sided coated with active material. The electrodes are separated by an electrical insulating separator. An electrode stack results, if several layers are welded together on the respective electrode tab. Increasing the number layers in an EP results in a higher capacity and a lower resistance of the battery. The capacity increases linearly with the active electrode area. [33] Some researchers investigate the behavior of IP by modifying the cell. However, only a few experimental studies specifically address the IP, as the experimental setup can affect the cell's behavior and is associated with high effort [35–38]. A more significant number of researchers focus on EP. One aim of these studies is to provide valuable insights into understanding the IP behavior.

The capacity of a parallel string is defined as the sum of all parallel-connected cells, see Equation 2.4.

$$C_{\text{tot}} = \sum_{p=1}^n C_p \quad (2.4)$$

In a parallel circuit the current, I_p , is distributed across all parallel paths. The sum of all currents

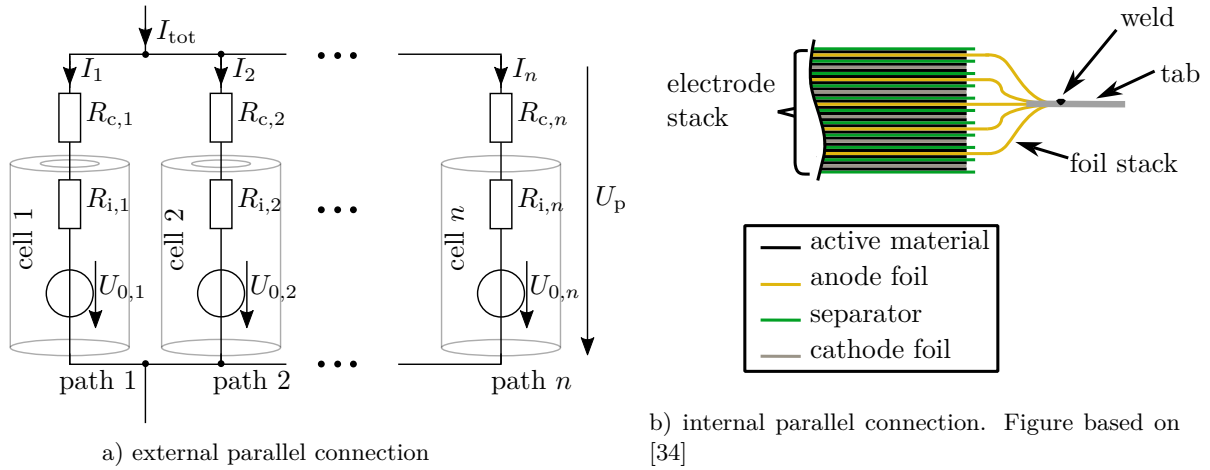


Figure 2.1: Example of a parallel connection. a) n parallel (np) connection within round cells, defined as an external parallel connection. b) electrode stack with parallel connection inside a pouch cell defined as internal parallel connection.

results in the total current of the system, I_{tot} , see Equation 2.5.

$$I_{\text{tot}} = \sum_{p=1}^n I_p \quad (2.5)$$

If the parallel paths differ in their parameters, an unequal current distribution can occur [39–41].

A limitation of parallel connection is, that due to the increased total current, high-current plugs have to be used. In addition, cells connected in parallel must have parameters that are as identical as possible in order to achieve a homogeneous current distribution [42]. Besides that, cells connected in parallel must be as close together as possible to reduce connection resistances. [25]

A battery system in this work is defined according to Figure 2.1 a). Each parallel path x consists of a contact resistance, $R_{c,x}$, and a battery cell, represented by a voltage source, $U_{0,x}$, and an internal resistance $R_{i,x}$. The contact resistance, $R_{c,x}$, represents the resistance of the contact and connectors.

2.1.2 Thermal Boundaries

The performance, safety and aging of a battery cell are significantly influenced by the temperature of the cell [43–47]. It is therefore necessary to monitor the temperature of the battery cells using a BMS. Passive and active cooling methods are used to control the temperature within a battery. Environmental air can be used as a passive cooling method. A disadvantage is, that the air temperature must be within the operating range of the battery [48]. The Nissan Leaf, for example, uses this climatization method [49]. Passive cooling systems are simpler and with lower costs. Active cooling methods, on the other hand, use a heat exchanger and coolant. Additional energy is used to heat or cool to the battery the optimal temperature range. However, due to the higher density and conductivity of a liquid or a refrigerant compared to air, active cooling methods are used for high-performance applications. [48; 50; 51]

In addition to the cooling method, the connection to the cell also influences the cooling performance. A distinction is made between side, tab and immersion cooling [52]. Side cooling, for example, is used by the Tesla Model 3 [53]. In this system, the through-plane conductivity of the electrode-separator stack, k_{\perp} , limits the effective cooling power. A more efficient but also more challenging cooling method is tab cooling. Tab cooling utilizes the in-plane conductivity k_{\parallel} . Due to thermal contact resistances between the layers, the in-plane conductivity k_{\parallel} shows higher thermal conductivity compared to the through-plane conductivity k_{\perp} . [54] Another cooling method is immersion cooling, where the battery cells are immersed in an electrically insulating and thermally highly conductive liquid and can therefore be optimally climated [55].

Furthermore, to the used cooling method, energy consumption, costs, weight, safety, and reliability are quality indicators of a BTMS [56]. When deciding on a cooling strategy, a compromise must be found between costs and performance. High-performance applications, like fast charging of EVs, necessitate advanced thermal management. The aim is to charge the maximum amount of energy in the shortest feasible time. Conversely, home storage systems typically do not need such complex cooling mechanisms. The design goal is often maximum internal temperature gradients up to 2°C at cell level [57; 58]. Within a battery system, the goal is to keep the temperature differences below 5°C [59–61]. Good thermal management of the cells results in an equal and slower aging [43; 44].

Different researchers investigated the influence of temperature gradients within a cell [62–64] and within a pack [35; 65–71]. For instance, Dai et al. [62] investigated the impact of internal temperature gradient on impedance characterization, defining the total impedance of the cell as the mean impedance of the different tempered regions inside the cell.

Series and parallel connection with forced temperature gradients were investigated on pack level. Zilberman et al. [69] applied a forced temperature gradient on six NMC cells connected in series. This temperature variation led to differing rates of degradation and voltage drifts among the cells [69].

Naylor Marlow et al. [70] and Klein and Park [71] conducted aging studies of parallel connected cells with thermal gradients. These are explained in more detail later.

Especially in parallel-connected battery systems, thermal management is indispensable and defines the overall system’s performance. Whereas due to inhomogeneous temperatures across parallel-connected cells, an inhomogeneous behavior can be the result [65; 70; 71].

2.2 Fundamentals of the Current Distribution within a Parallel Battery System

The current and voltage of an electrical circuit are defined by Kirchhoff’s loop and node law. According to Kirchhoff’s loop law, see Equation 2.7, the voltage of two parallel paths is equal. In contrast, the current divides according to the Kirchhoff node law, following Equation 2.5. Consequently, differences between both parallel paths result in a compensating inhomogeneous current to reach the voltage equilibrium. The following introduces the definition of voltages and currents of parallel-connected batteries. Figure 2.1 a) is used as a basis for the following equations.

The sum of the overpotentials and the $U_{0,x}$, which represents the OCV, defines the voltage of a cell x , $U_{\text{cell } x}$. All overpotentials are represented with the time-dependent internal resistance, $R_{i,x}$. The corresponding equation is given in Equation 2.6.

$$U_{\text{cell } x} = U_{0,x} + I_x \cdot R_{i,x} \quad (2.6)$$

The voltage U_p of each parallel path x is then defined by the sum of the cell voltage, $U_{\text{cell } x}$, and the voltage over the contact resistance, $R_{c,x}$, see Equation 2.7. The same voltage lies across path y .

$$U_p = U_{\text{cell } x} + I_x \cdot R_{c,x} = U_{\text{cell } y} + I_y \cdot R_{c,y} \quad (2.7)$$

Consequently, in an np connection the current through path x can be calculated as follows, see Equation 2.8.

$$I_x = \frac{I_y \cdot R_{c,y} + I_y \cdot R_{i,y} - U_{0,x} + U_{0,y}}{R_{c,x} + R_{i,x}} \quad (2.8)$$

Equation 2.8 can be divided into internal and external influencing factors, see Equation 2.9. Internal parameters are the cell resistance, $R_{i,x}$, cell capacity, C_{cell} , and the OCV. External parameters are the contact resistances, $R_{c,x}$.

$$I_x = \frac{1}{\underbrace{R_{c,x}}_{\text{external}} + \underbrace{R_{i,x}}_{\text{internal}}} \cdot \left(I_y \cdot \underbrace{R_{c,y}}_{\text{external}} + I_y \cdot \underbrace{R_{i,y} - U_{0,x} + U_{0,y}}_{\text{internal}} \right) \quad (2.9)$$

Consequently, each parallel connection of cells can lead to an inhomogeneous current distribution due to different parameters, such as U_0 and resistances, R_i and R_c [70; 72; 73].

2.2.1 Intrinsic Causes for an Inhomogeneous Current Distribution

The intrinsic causes for an inhomogeneous current distribution between parallel-connected cells can be divided into influences caused by the OCV, the internal resistance, $R_{i,x}$, and capacity, $C_{i,x}$. The shape of the OCV, the internal resistance, $R_{i,x}$, and capacity, $C_{i,x}$ have a significant influence on the current distribution between cells connected in parallel. [73–75]

Open Circuit Voltage

The most significant part of the cell voltage is carried by $U_{0,x}$. The shape of the OCV across the SoC depends on the composition of the electrodes [76; 77]. In addition to material-related influencing factors and temperature, the OCV also depends on the aging condition, especially in the case of anodes containing silicon [78; 79].

Figure 2.2 a), b) and c) represent the OCV of three investigated cell technologies, as listed in Table 2.1. In addition to different voltage levels at which the cells can be operated, the voltage changes differently over the SoC for all cell technologies. This can be analyzed with the derivative of the voltage according

to the charge, also called differential voltage. The differential voltage is plotted in subfigures d), e) and f) and corresponds to the voltage measured during the 2p charge process. Figure 2.2 shows exemplarily the resulting SoC imbalance between the parallel-connected cells during a current distribution with a resistance inhomogeneity in the order of around 20-25% R_{AC} . The extent of this imbalance can be correlated with the slope of the OCV.

The LIB_{LFP} cell, in particular, shows a very flat characteristic voltage curve over the SoC. This flat characteristic curve results in the highest Δ SoC. The most significant discrepancies are observed in parts of the OCV where almost no change in the voltage is visible. Across all examined cell technologies, the overall lowest points of the differential voltage, indicating areas with minimal OCV fluctuation, align with the points of fastest change SoC divergence between the two cells.

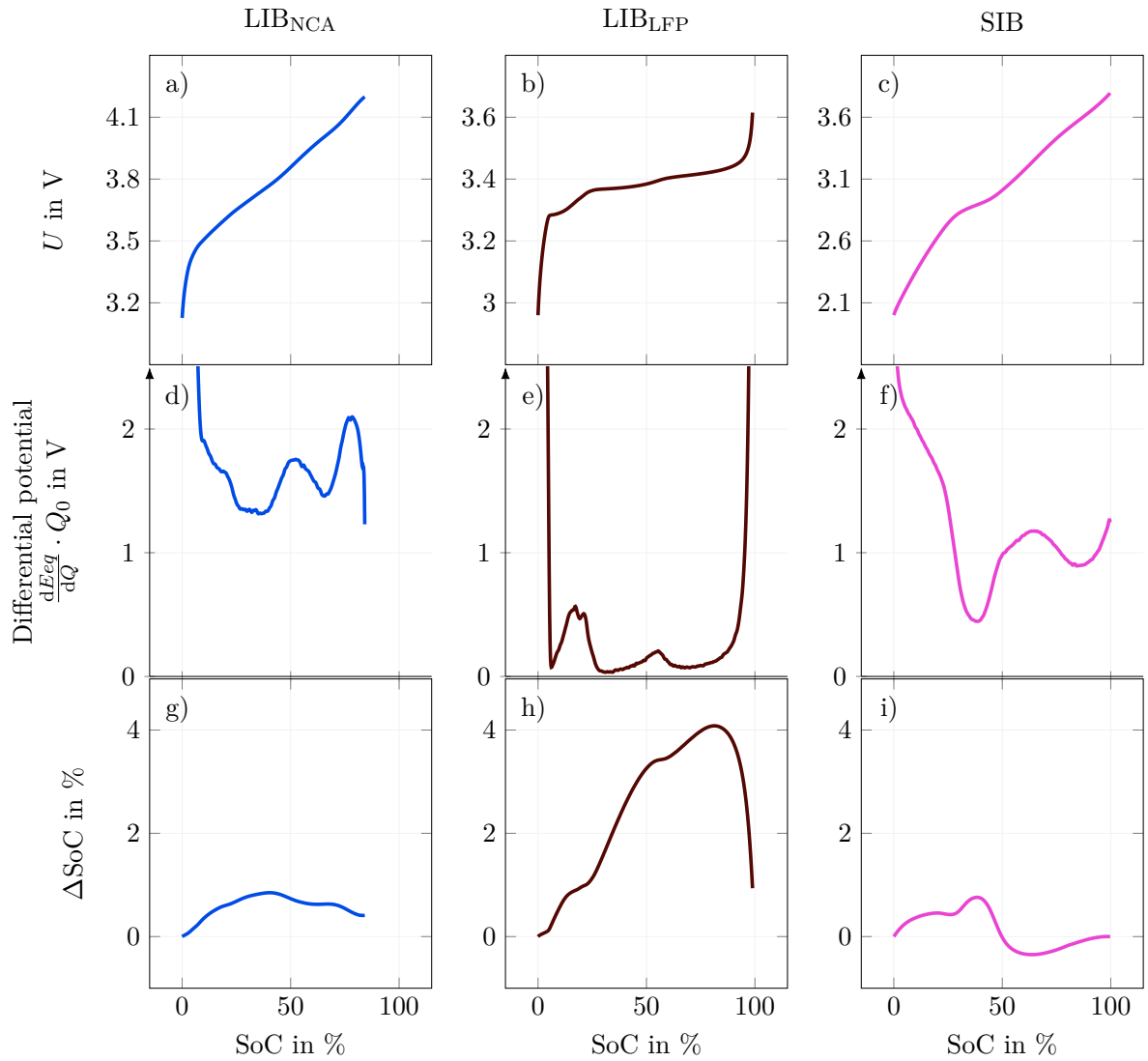


Figure 2.2: Influence of the OCV on the current distribution and resulting SoC difference for different cell technologies. All measurements are carried out at 0.5 C and 25 °C. Subfigures a), b) and c) show the voltage during constant current (CC) charging. The resulting differential potential is plotted in subfigures d) e) and f). The resulting SoC differences at an inhomogeneous contact resistance in the order of about $R_{c,2} = 5 \text{ m}\Omega$ are plotted in subfigures g), h) and i). The measurements are carried out with the VPC, which is explained in Chapter 2.4.2.

Resistance and Capacity

Another factor contributing to the cell voltage is the overpotential, which is determined by the time-dependent internal resistance, $R_{i,x}$. This internal cell resistance, as explained on page 7, depends on the current level, the temperature, and the pulse duration. The voltage drop over the internal resistance influences the path voltage, U_p . Intrinsic resistance and capacitance variations between cells can arise due to differences in cell production. Varying active material compositions and fluctuating material components can influence cell quality [80; 81]. Schindler et al. [80] found variations of capacity and resistance of cells within different cell batches. A reproducible experimental study by isolating and examining changes in internal resistance or differences in capacitance is challenging. Only a few research groups have carried out parallel-connected aging studies within initial cell-to-cell variations [73; 82–85]. Due to the relatively more minor effort, most of the isolated parameter variations are carried out within a simulation [75; 86–92]. According to Brand et al. [85], the initial current distribution can be approximated within the current divider. Initially, where both cell voltages are on the same level, and all electrochemical processes are relaxed, the resistance difference defines the current distribution. [85] On the other hand, the capacity of a cell can have an indirect influence on the current distribution. In a first approximation, it does not affect the cell voltage. However, over a longer load time, a lower capacity results in a faster change of the OCV which results in differences within the current distribution. [85]

This is in correlation with the findings of Hust [74]. The current distribution in flat OCV segments is predominantly influenced by deviations in resistance between parallel-connected cells. This can be demonstrated by comparing LIB_{NCA} with SIB. The SIB cell technology shows a less differential potential compared to LIB_{NCA}, see Figure 2.2 d) and f). However, the greatest difference in SoC of LIB_{NCA}, is the same that is observed with SIB. Comparing the R_{DC} of both cell technologies, the SIB cell shows a 2.3 times larger resistance than the LIB_{NCA} cell. The R_{DC} , therefore, also plays a role in determining the impact of imposed contact resistance on current distribution, and, as a result, influences the difference in SoC.

2.2.2 External Causes for an Inhomogeneous Current Distribution

External causes for an inhomogeneous current distribution are the electrical contacting of the cells, which leads to a higher path resistance, and a temperature inhomogeneity across the parallel-connected cells.

The electrical contacting includes both the cell contacts and the cell connectors. The resistance of cell connectors can be calculated by the geometric dimensions and the specific resistance. In order to utilize as much space as possible in a battery storage system, different locations can result in different connector resistances between cells connected in parallel. The resistance of cell contacts varies due to different contacting techniques.

Besides constant influences, dynamic influences, such as the temperature of the cell, influence the cell behavior and, therefore, the current distribution. Hence, it is essential to manage the temperature with a BTMS, since a change in the cell's temperature influences the cell's parameters, such as the transport, kinetic and mass-transfer properties [93]. The cell resistance decreases with an increasing temperature according to the Arrhenius equation [94].

Most studies were carried out with external factors influencing the current distribution. Problematic

are production issues such as cells scattering within the same batch [80], and reproducibility within cell-to-cell variation. Additionally to the research aim of a specific influencing parameter, a clean and defined test-bench is required [15]. An experimental setup's inaccuracies and influencing factors must be significantly smaller than the cells' scattering to generate reliable results.

2.3 State of the Art of Electrical Contact Resistances and the Measurement of the Current Distribution

2.3.1 Electrical Contact Resistances

The electrical connection between cells defines the serial and parallel connection. High mechanical stability and low electrical resistance are the basic requirements of an electrical connection. [28]

High electrical resistance results in two main influencing factors on the battery system. A larger electrical resistance will dissipate more energy and generate more heat [95]. This additional heat can result in a temperature increase in the cell [96; 97]. In addition, Offer et al. [98] concluded that the connection resistance causes more effect of the inhomogeneous current distribution than an inhomogeneous internal resistance. A similar result was demonstrated by Wu et al. [99] by investigating the effect of inhomogeneous contact resistance. While inhomogeneity in constant current operation should rebalance itself over long cycles, in dynamic pulse loads, inhomogeneous contact resistances result in current inhomogeneities and, consequently, temperature imbalances within a pack. [99] The influence of connection resistance on the current distribution is, therefore, an important topic.

A review of joining methods such as tungsten inert gas welding, resistance welding, magnetic pulse welding, ultrasonic welding, laser beam welding, soldering, and mechanical assembly was carried out by Zwicker et al. [28] and Das et al. [100]. According to Das et al. [100] four interdisciplinary requirements have to be fulfilled: electrical and thermal requirements with low electrical resistance with low scatter and low thermal input during the joining process; material and metallurgical requirements with low corrosion risk, the possibility of joining dissimilar materials, and the adaptability to a variety of surface conditions and materials; mechanical requirements with high ultimate tensile force (UTF) and low vibrational damage; the economic requirements for mass production and low production costs. Additionally, Brand et al. assessed the electrical contact resistance (R_C) and UTF of welding [101], soldering [102] and press contacts [103] in three publications. These joining techniques will now be introduced shortly.

Well-established joining techniques

Press contacts, screwed joints, and electrically conductive pads can be used as a detachable joining technique. Due to the possibility of recontacting, this joining technique is well-suited for electrical connections at the module level. This has the advantage that defective modules can be easily replaced. There are also battery pack manufacturers who connect all cells with electrically conductive pads [104]. Moreover, mechanical assembly eliminates the need for heat input during manufacturing, enhancing the attractiveness of detachable contacts for battery assemblies and systems that include heat-sensitive electrical components. Mostly aluminum, copper, brass, and hilumin are used for press contacts. [103; 105]

Soldering represents another joining technique, which involves introducing a third material into the joint through heat input. Heat input from soldering can induce high temperatures, which limits the potential for temperature-sensitive applications such as battery cells. [102; 106–108]

Welding is a crucial joining method, offering high mechanical robustness and low electrical resistance [101]. Various welding techniques, such as resistance spot welding, ultrasonic welding, and laser beam welding, are available, each with unique features. Resistance spot welding is highly effective for joining relatively thin connections. It utilizes a weld current to quickly heat the contact points to a melting state, affecting only a minimal amount of the material. Insufficient weld energy will fail to produce a weld, whereas too much energy can lead to the electrodes sticking together. [100; 105; 109; 110] Most resistance spot welding devices use a dual pulse. The first pulse is used to remove oxides and contaminants from the surface. The second is used for the welding process. [111–113]

An alternative to resistance spot welding is ultrasonic welding. Using ultrasonic vibrations, objects are scrubbed into one another until they are joined together. Due to the vibrations, which remove oxides and contaminants from the weld surface, this is an advantage to other joining techniques [114–117]. Another benefit is the low process temperature [101]. When implementing ultrasonic welding, especially in applications involving battery cell contact, it is important to consider the risk of component damage during manufacturing. Ultrasonic welding can potentially harm the cell. [118]

One of the most used welding techniques for battery application is laser beam welding. It melts the joining material with an exact weld seam [119; 120]. By modifying the trajectory of the weld seam and by adjusting the trajectory [121], the temporal [122] or spatial power distribution [123] a broad range of materials with varying thicknesses and desired weld seam properties can be joined.

Brand et al. investigated the joining techniques mentioned above in terms of their electrical and mechanical performance. In their research, R_C and UTF were evaluated as key electrical and mechanical performance indicators.

Additionally, area-based connections by means of ECA were investigated in this thesis, see Chapter 3. During the voltage measurement, two inhomogeneities were noticed: firstly, at the current injection point and secondly, at the contact connection. Doubling the contact area of the connector does not necessarily lead to a reduction of the contact resistance by 50%. These inhomogeneities are explained in more detail in Chapter 2.4.1.

2.3.2 Measurement of the Current Distribution

In industrial applications, mainly only one current sensor is used to quantify the current over the whole battery pack. To understand the influencing factors for a convergent or divergent current distribution, scientific research aims to quantify the current of each parallel path. Therefore, many researchers designed different test-benches to measure the current of parallel-connected batteries and understand the impact factors of inhomogeneous behavior.

The aim is to measure the current distribution as precisely as possible while minimizing the influence on the system. Different current sensors from contactless, e.g., hall- and fluxgate sensors, up to contacting sensors, e.g., shunt resistance, are used. The advantage of contactless sensors the location outside the current path. These sensors do not influence the current distribution. In contrast, contacting sensors located inside the current path can influence the current distribution. In addition to the possible influences of the current sensor, the measurement setup can have an impact on the current distribution.

Most tests are conducted using fixed connections such as soldering or welding. Only a few implemented detachable connections in their test-benches [70; 73]. A detachable connection allows the monitoring of individual cell aging over time. A possible influencing factor of a detachable connection is a different path resistance after recontacting the cells.

Some researchers have quantified the additional resistance due the measurement equipment [35; 66; 70; 71; 74; 85; 124–128]. In contrast, others have not [38; 39; 72; 83; 129–133]. Fill et al. [66] for instance, presented a measurement test-bench with an adjustable thermal connection for pouch cells. The current was determined using load cables as a shunt resistance with an additional resistance of $0.3\text{ m}\Omega$ [66].

Summarized, there are two challenges with conventional test-benches. One challenge is the reproducibility of a measurement on a second test-bench, and the other is tracking individual cell behavior. The first can be reached with a high technical effort. By experimenting with several modules, a reliable statement can be achieved. During an aging study, the parallel circuit must be separated to achieve the second and track the individual OCV, capacitance and resistance. Consequently, the check-up is carried out in the 1p1s network and then reconnected in the parallel network.

The influence of the recoupling of the individual cells before and after a check-up should be considered. For example, Naylor Marlow et al. [70] found variations in the current distribution due to differences in the contact resistance caused by the repeated assembly and disassembly of the packs. This problem is minimized by the VPC methodology described in Chapter 2.4.2. Figure 2.3 shows the influence of the recontacting of a conventional test-bench and the VPC, which will be presented in Chapter 2.4.2. Within copper clamps, the detachable connection of the conventional test-bench was realized. The

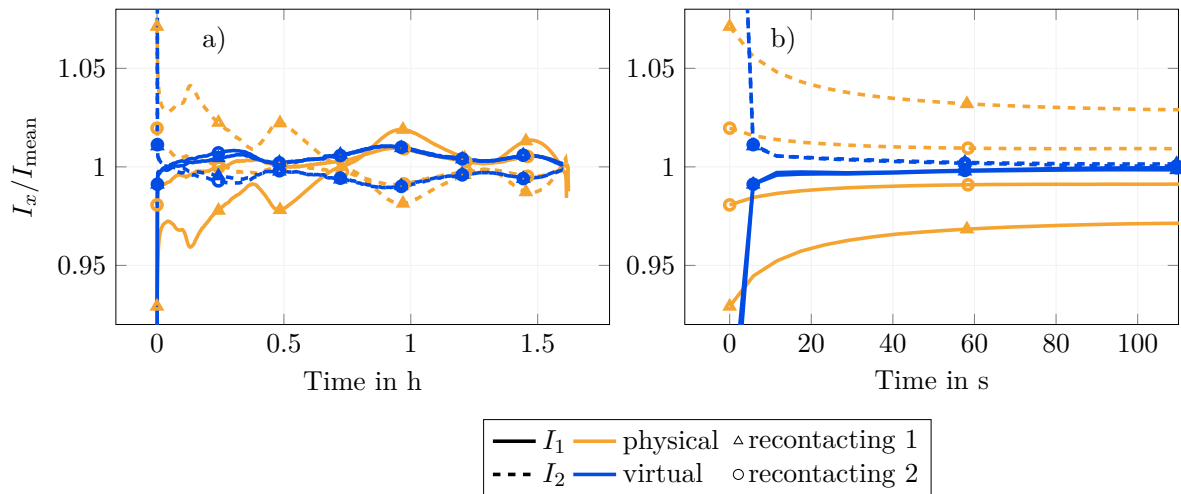


Figure 2.3: Current distribution of 2p connection measured with a conventional test-bench and the virtual parallel connection (VPC). Between two full cycles, the cells were recontacted, and the current distribution was measured to determine the influence of recontacting. The cells are resistance welded to hilumin stripes. In the conventional test-bench these are clamped between two copper clamps. Conventional test-bench was used by [134] and is explained briefly in Fig. 2 in Chapter 4. Subfigure a) shows the current distribution cells during CC charging at 0.5 C and $25\text{ }^\circ\text{C}$. Exemplary, the influence of a faulty contact is shown. Subfigure b) presents a detail-view within the first 100 s.

recontacting can have a significant influence on the current distribution. Especially within a faulty contact, the current distribution differs between a recontacting of the physical test-bench. Therefore, different path resistance can result, leading to a distinct current distribution. The virtual parallel-

connected cells result from a current distribution without path resistances, and consequently, the cell parameters determine the current distribution.

Besides the test-bench, various investigations were carried out, such as thermal gradients [65; 70; 71], different chemistry combinations [135], influence of pressure [136], inhomogeneous connection resistances [15; 66; 137], number of cells in parallel [90; 138] and different connection typologies [127; 139; 140].

Prior research studies focused on different impact factors on an inhomogeneous current distribution, such as intrinsic cell-to-cell variations [39; 73; 82–85; 89; 92; 126; 129; 130; 141; 142], aging [40; 67; 68; 70; 73; 83; 84; 141] and external influencing factors e.g. temperature [65; 67; 68; 70–72]. Most of the experimental studies in literature were carried out in a 2p connection, with only some researchers investigating higher parallel-connected setups [37; 70; 71; 74; 125; 128; 132].

The aim is to understand influencing factors for a divergence or a convergence of the current distribution over time. In the literature, there is disagreement regarding the existence of a convergence among parallel-connected cells over aging. While some researchers affirm this theory [84; 125], others find a divergence behavior [92; 131; 143–145].

Influence of path temperature

Naylor Marlow et al. [70] conducted an aging study within NMC and lithium cobalt oxide (LCO) cells, focusing on how thermal gradients impact the performance of cells connected in parallel. A divergent capacity fade between parallel-connected LIB cells was observed in a temperature gradient of 20 to 45 °C [70]. Al-Amin et al. [68] investigated the aging effect of four parallel-connected NMC cells with a forced temperature gradient. The cell exposed to the highest temperature degraded the fastest, which is attributed to the combined effects of higher temperature and current throughput. Klein and Park [71] investigated five LFP and NMC cells in parallel. Within a temperature gradient between 5 to 20 °C, current differences of up to 1.8 times the nominal current occurred.

Cavalheiro et al. [67] conducted an aging study on a stack of five chemically non-identified pouch LIB cells connected in parallel at an ambient temperature of 25 °C. The study found that the cell positioned at the center of the stack underwent a notably faster capacity fade and an increase in resistance. Higher local temperatures up to 8 °C led to this behavior. The cell located at the center reached peak values of up to 1.5 times the nominal current, whereas the current profiles of the outer cells remained relatively stable. [67]

Influence of path resistances

In contrast to studies on inhomogeneous temperatures, the impact of path resistances in parallel circuits has been not been extensively explored at an experimental level. According to Brand et al. [85] the current initially divides according to the current divider. The resistance difference defines the current distribution, as also visible in Figure 2.3 by the use of a conventional test-bench. A study investigating the aging behavior of parallel-connected NMC cells based on initial cell-to-cell variation of internal resistance and capacity as well as charging profiles was presented by Schindler et al. [73]. The data of Schindler et al. [73] showed, that neither matching by internal resistance nor by capacity has a benefit for the aging behavior of cells connected in parallel. [73]

2.4 Developed Methods

This section presents the developed methods from the papers present in Chapter 3 and Chapter 4. Here, a short introduction is provided.

2.4.1 Measurement of Electrical Low-Contact-Resistances

Usually, representative replacement samples are manufactured to determine the electrical resistances of battery connections with the aim of measuring in a homogeneous area. The benefit of a representative replacement sample is that there is enough space to carry out the measurement. The representative replacement samples should have the same materials to quantify the electrical connection. Figure 2.4 shows a schematic with four laser-welded lines.

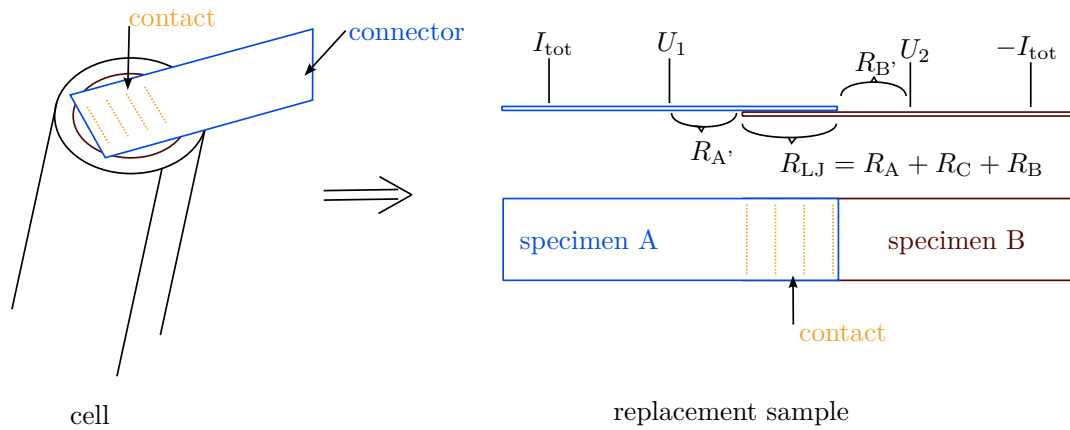


Figure 2.4: Schematic view of a cylindrical cell with a cell connection. For the measurement of the electrical contact resistance, the cell connection is transformed into a representative replacement sample. The resistance over the lap joint consists of the sum of R_A , R_B and R_C . The figure is based on [146].

In the homogeneous area, simple equations can be used to solve the problem. If a linear voltage drop across the measurement object is apparent, the resistance can be calculated using geometric variables, length l and area A , and the specific resistance, ρ , according to Equation 2.10.

$$R = \rho \frac{l}{A} \quad (2.10)$$

By knowing the material parameters and geometry dimensions and by measuring the resistance over a defined length, the resistances of the lap joint R_{LJ} and the specimens $R_{A'}$ and $R_{B'}$ can be determined.

Due to the analysis of the electrical contact connection in a simulation, two inhomogeneities were identified: the influence of the current imprinting point, see Figure 2.7, and, the current distribution in area-based connections, see Fig. 4 in Chapter 3.

Contact resistances are usually determined using a 4-wire measurement. In the 4-wire measurement, a current pulse is applied to the power lines, I_{tot} , while the voltage response is measured over the sense lines, $U_1 - U_2$. The voltage measurement requires a very low measuring current, to be able to neglect the resistance across the measuring line. This means that the pure resistance of the object can be determined. The resulting measured resistance, $R_{measured}$, is the sum of the resistances $R_{A'}$,

$R_{B'}$ and R_{LJ} , see Figure 2.4 and Equation 2.11. The resistance over the lap joint, R_{LJ} , is defined as the sum of both specimen resistances inside the lap joint, R_A and R_B , and the contact resistance R_C . According to Holm [147], the R_C is defined as the sum of film or layer resistance, and the resistances of the surfaces where the electrical conduction takes place.

$$R_{\text{measured}} = R_{A'} + \underbrace{R_A + R_C + R_B}_{R_{LJ}} + R_{B'} \quad (2.11)$$

A sensitivity analysis was performed using LTspice simulations. Consequently, the issue was simplified into a two-dimensional problem by simplifying the surface. The analysis proceeded with two samples, specimen A and specimen B, being in contact with each other. These two are defined with identical geometric and electrical values. This results in an identical resistance for both, $R_A = R_B$. For the contact resistance, R_C is assumed to be homogeneous along the contact surface and the current can flow only vertically through the contact. Four equally distributed laser-welded lines result in the following resistance network of Figure 2.5. The following variables, R_A , R_B and R_C are defined in Equation 2.12. k corresponds to the amount of contact paths between the specimens. In this case $k = 4$.

$$R_A = (k - 1) \cdot r_a; \quad R_B = (k - 1) \cdot r_b; \quad R_C = \frac{1}{k \cdot r_c} \quad (2.12)$$

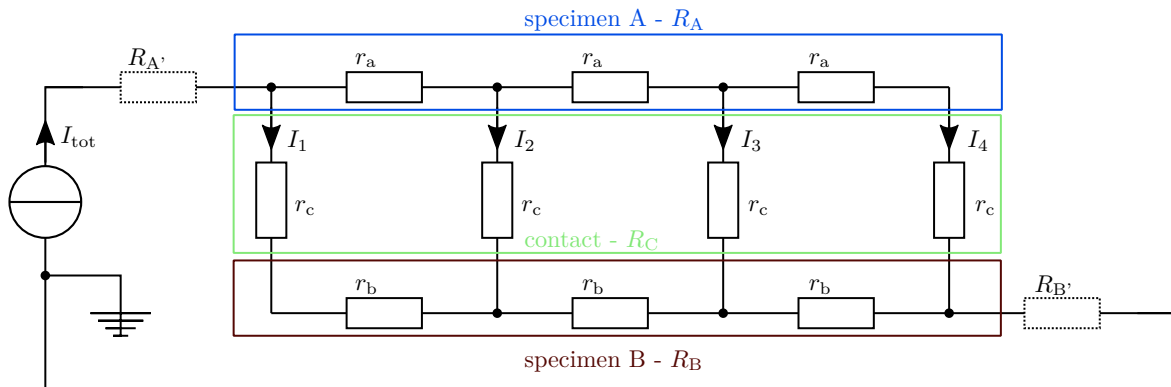


Figure 2.5: Electrical circuit model (ECM) of the LTspice simulation with two specimens, A and B, according to Figure 2.4. Each welded line is represented by a contact path, r_c .

Three cases are considered within a sensitivity analysis, with the current through each path being analyzed, see Table 2.2. A different amount of current flows through each path depending on the ratio of r_a to r_c .

- High contact resistance: a high contact resistance compared to the specimen's resistance results in a linear current distribution through the contact area. Through all paths, almost the identical current flow occurs.
- Low contact resistance: a low contact resistance compared to the specimen's resistance results in a current flow at the beginning and the end of the lap joint.
- Medium contact resistance: an equal contact resistance compared to the specimen's resistance results in a non-linear current distribution.

Table 2.2: Current distribution according to the connection in Figure 2.5. The simulation was carried out with LTspice, and three cases were considered.

case	I_1	I_2	I_3	I_4	I_{tot}
a) $r_a = r_b = 0.01 \cdot r_c$	25.25 %	24.75 %	24.75 %	25.25 %	100 %
b) $r_a = r_b = 100 \cdot r_c$	49.75 %	0.25 %	0.25 %	49.75 %	100 %
c) $r_a = r_b = 1 \cdot r_c$	37.5 %	12.5 %	12.5 %	37.5 %	100 %

Summarizing, the macro perspective of the current distribution in electrical connections depends on the ratio between R_C and R_A . The relationship between contact resistance and contact area is not linear. In other words, doubling the contact lines does not result in half the contact resistance. To analyze the problem more generally, the next section will present the methodology to determine the contact resistance of area-based connections.

Determination of Area-based Electrical Contact Resistances

An area-based resistance is of interest to quantitatively compare the contact resistances with the parameterization of the simulations. A homogeneous resistance over the whole area is assumed, $k \rightarrow \infty$. However, as indicated by Figure 2.5, the current can be distributed inhomogeneously over this area as the current splits to reach the path of least resistance.

To analyze this, the measured resistance over the lap joint, R_{LJ} and the resistance of the two specimens, R_A and R_B , are defined as known quantities. R_C is the variable of interest. In order to compute the R_{LJ} for an arbitrary kP circuit, Δ -star transformations can be used to transform a kP into a $(k-1)P$ circuit. The following reciprocal formula is the result, see Equation 2.13. The derivation is given in Chapter 3 [14].

$$\begin{aligned}
 R_{LJ}^k(r_a^k, r_b^k, r_a, r_b, r_c) &= s_a + R_{LJ}^{k-1}(\tilde{r}_a^{k-2}, \tilde{r}_c^{k-1}, r_a, r_b, r_c) \\
 &\text{with } \tilde{r}_a^{k-2} = r_a^{k-2} + s_b \text{ and } \tilde{r}_c^{k-1} = s_c \\
 &= \frac{r_a^k(r_b + r_c)}{r_a^k + r_b + r_c + r_c^k} + R_{LJ}^{k-1}(\tilde{r}_a^{k-1}, \tilde{r}_c^{k-1}, r_a, r_b, r_c) \\
 &\text{with } \tilde{r}_a^{k-1} = r_a + \frac{r_a^k r_c}{r_a^k + r_b + r_c + r_c^k} \text{ and } \tilde{r}_c^{k-1} = \frac{r_c(r_b + r_c^k)}{r_a^k + r_b + r_c + r_c^k}
 \end{aligned} \tag{2.13}$$

s_a , s_b , and s_c represent resistances after a Δ -star transformation. A convergence analysis showed that after $k > 82$ iterations, the reciprocal solution approaches the theoretical solution by less than 1 %.

A similar problem was found by Euler and Nonnenmacher [148] within the current distribution in porous electrodes. The following analytical solution was found by solving differential equations. Equation 2.14, extracted from [148], represents the solution of plate-shaped electrodes, the superposition of two counteracting hyperbolic cosine functions.

$$W = \frac{a \cdot b \cdot L}{a + b} \left[1 + \frac{2 + \left(\frac{a}{b} + \frac{b}{a}\right) \cosh\left(\sqrt{(a+b)c} \cdot L\right)}{\sqrt{(a+b)c} \cdot L \sinh\left(\sqrt{(a+b)c} \cdot L\right)} \right] \quad (2.14)$$

Substituting the variables from Equation 2.14 with the variables defined in this thesis, $a = r_a, b = r_b, c = r_c, L = k$ leads to Equation 2.15.

$$R_{LJ} = \frac{r_a \cdot r_b \cdot k}{r_a + r_b} \left[1 + \frac{2 + \left(\frac{r_a}{r_b} + \frac{r_b}{r_a}\right) \cosh\left(\sqrt{(r_a + r_b)r_c} \cdot k\right)}{\sqrt{(r_a + r_b)r_c} \cdot k \sinh\left(\sqrt{(r_a + r_b)r_c} \cdot k\right)} \right] \quad (2.15)$$

To determine r_a, r_b and r_c Euler and Nonnenmacher [148] used an integral instead of the discrete approach according to Equation 2.12 leading to Equation 2.16.

$$R_A = k \cdot r_a; \quad R_B = k \cdot r_b; \quad R_C = \frac{1}{k \cdot r_c} \quad (2.16)$$

In the case of both specimens having the same resistance, $R_A = R_B$, and consequently $r_a = r_b$ the following simplification can be used.

$$\sqrt{2 \cdot r_a \cdot r_c} \cdot k = \sqrt{2 \cdot \frac{R_a}{k} \cdot \frac{R_c}{k}} \cdot k = \sqrt{2 \cdot \frac{R_a}{R_c}} \quad (2.17)$$

Equation 2.18 gives the analytical approach to determine the resistance.

$$R_{LJ} = \frac{R_A}{2} \left[1 + \frac{2 + 2 \cosh \sqrt{2 \frac{R_A}{R_C}}}{\sqrt{2 \frac{R_A}{R_C}} \sinh\left(\sqrt{2 \frac{R_A}{R_C}}\right)} \right] \quad (2.18)$$

Both approaches and the asymptotic behavior are plotted in Figure 2.6. It represents the relation between R_{LJ} and R_C . Contact resistances in the order of $R_C < 0.01 \cdot R_A$ results in an almost ideal parallel circuit while the ratio of R_{LJ}/R_A is approaching 0.5. At high contact resistances in the order of $R_C > 0.4 \cdot R_A$, the reciprocal and the analytical solution approach the asymptote, and a linear relationship result. A larger contact area results in a lower contact resistance in this linear relationship through all paths k , where the same amount of current flows. In contrast, a larger contact area does not result in a smaller contact resistance in the non-linear relationship. The distance between the contact area's start and end point primarily defines the contact resistance.

If $R_A \neq R_B$, the current is divided according to the path with the lower resistance for as long as possible. The current is divided according to the resistance ratios of the two resistors, R_A and R_B .

Furthermore, it was assumed that the current in specimen A and B can only flow horizontally whilst it can flow only vertically within the contact. In other words, the above mentioned mathematical

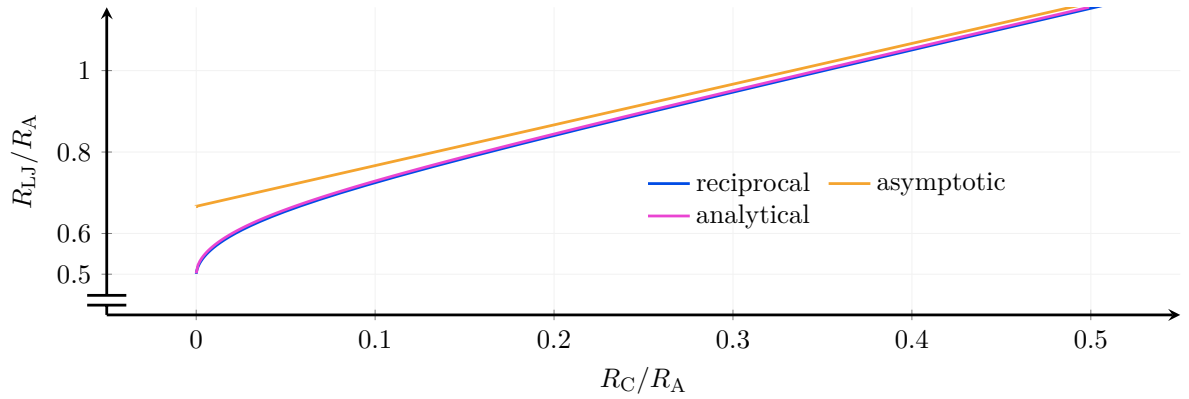


Figure 2.6: Graphical analysis of the current distribution in area-based connections. The analytical solution of Euler and Nonnenmacher [148] and the reciprocal, with $k = 10\,000$, show the ratio of R_{LJ} to R_C . Contact resistances in the order of $R_C < 0.01 \cdot R_A$ results in an almost ideal parallel circuit, i.e., the ratio of R_{LJ}/R_A approaches 0.5. In contrast, contact resistance in the order of $R_C > 0.4 \cdot R_A$, both theoretical methods approach the asymptote and a linear relationship results.

equations are only correct when the current does not flow horizontally through the contact. This statement is valid under the condition that a thin contact layer is utilized and the conductivity of the specimen material exceeds that of the adhesive. However, if the contact layer is thicker and possesses conductivities significantly higher than the specimens, the ratio may drop below 0.5. Under such circumstances, current will flow in a horizontal direction.

Considering the case of four welded lines and an excellent contact, refer to the Figure 2.4 and $R_C < 0.01 \cdot R_A$. In such a scenario, the outer lines at the ends of the contact surface are sufficient to ensure optimal electrical connectivity. An additional weld seam does not lower electrical resistance between these two lines. Consequently, the positioning of the two weld seams should be as orthogonal as possible to the direction of the current. Schmidt [149] demonstrated a similar result using an optimization algorithm. In the optimization algorithm, the number of spot welds was set as a boundary condition, with the goal to determine the optimum position of the spot welds. The electrically and mechanically optimized algorithm selected the welding points orthogonally to the current flow.

Phenomena at the Current Injection

Resistance measurements are usually carried out by using the 4-wire technique. This subsection discusses the impact of the current injection of the power lines on the voltage measurements. The extent of inhomogeneous behavior was quantified through a finite element method (FEM) simulation. It specifically examines the effect of the current injection, as illustrated in Figure 2.7. Additionally, inhomogeneities near the contact area are identified.

The simulation was carried out with a brass sample with a greater side length of $x = 15$ mm and a current injection at $x = 7.5$ mm and $y = 2$ mm. A radially symmetrical equipotential field is formed near the current injection point. When moving away from this point along the y -axis, the theoretical potential approaches the linear potential; see Figure 2.7 b).

Taking measurements in the inhomogeneous area, results in a different resistance. This resistance can be used to compare samples with each other, but the material parameters cannot easily be identified.

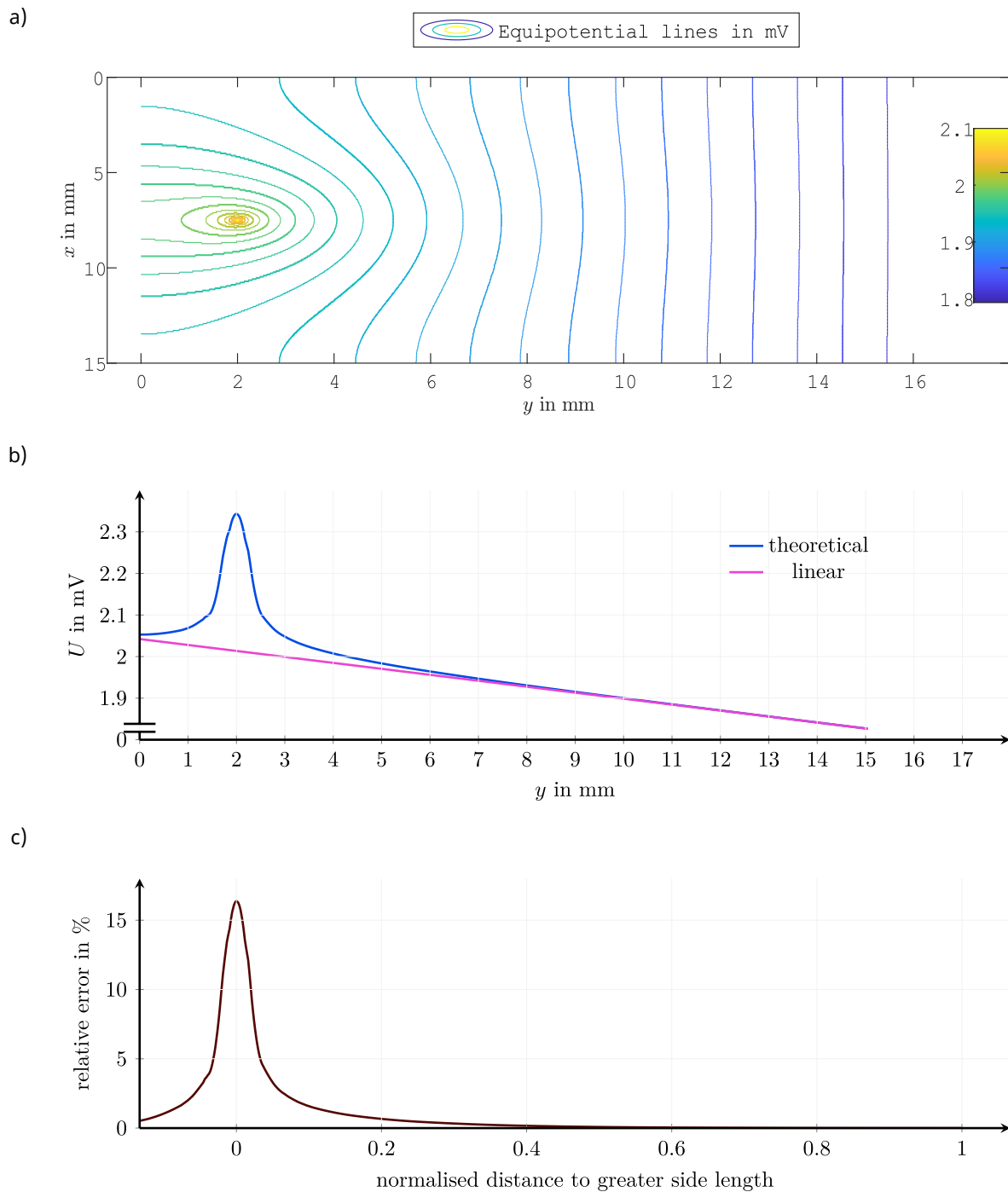


Figure 2.7: Influence of the current injection on the equipotential lines via an FEM simulation. The current was injected at $x=7.5$ mm and $y=2$ mm. a) Top view of the sample, including the electric equipotential lines. Around the current injection point, an inhomogeneity results. b) Resulting theoretical potential through a horizontal line at the sample at 7.5 mm and a comparison considering a linear potential drop. c) Relative error between the theoretical and the linear voltage curve normalized to the longest side length of the specimen's contact area (A). Figure is based on the publication presented in Chapter 3 [14].

The closer the voltage measurement is located at the current impingement point, the greater the effect of a position inaccuracy on the measurement accuracy, see Figure 2.7 c).

The problem can be described using Gauss's law. Gauss's law describes the electric field from a positive to a negative charge. The resulting electrical potential is orthogonal to the electric field. Consequently, an electric potential with radially symmetrical behavior results in an infinite plate. This phenomenon is known in the field of electrical engineering when calculating earthing rod resistances [150]. The earth represents the infinitely large surface. The resistance can be determined as a function of the radius.

In a geometrically limited conductor the electric field and the resulting electric potential are constricted, as represented in Figure 2.7. The radial behavior only occurs in the vicinity of the current application point. The problem can be analytically solved using mirror sources to fulfill the boundary conditions [151; 152].

The error between theoretical and linear potential decays to zero based on the dimensions of the sample. The gap between the power and sense pins should be at least half the length of the longest side of the sample's contact area. An inhomogeneous potential can also occur in the vicinity of the contact. A distance must also be maintained in order to measure in the linear range. A voltage measurement in the linear range is also necessary for the parameterization of simulations, where the effective contact resistance and the exact material parameters are required as input.

An analogy was found in mechanics with the principle of Saint Venant. The principle of Saint Venant states that the inhomogeneity caused by a load on a long cuboid depends on its geometry. After a distance of at least half the longest side length of the specimen's contact area, the relative magnitude of the inhomogeneity is less than 0.85 % and therefore negligible. In this case the behavior becomes linear [153; 154].

2.4.2 Virtual Parallel Connection

This section presents the methodology of the VPC. The problem with conventional test setups is that defined and undefined parasitic resistances in the measurement path are unavoidable, as shown in Chapter 2.3.2. In addition, a measurement setup to determine the current distribution involves much effort. The following discusses the methodology of the VPC and its advantages and disadvantages.

In any n parallel connection of battery cells, the current is divided according to Kirchhoff's node and loop law. The following equations are based on the schematic of Figure 2.1 a). To calculate the current in path x , $x \in [1, n]$, one must subtract the sum of currents flowing through the other $n - 1$ parallel paths from the system's total current, I_{tot} , as per Kirchhoff's node law, see Equation 2.19.

$$I_x = I_{\text{tot}} - \sum_{y \in [1, n], y \neq x}^n I_y \quad (2.19)$$

Kirchhoff's loop law determines the voltage of each parallel path, see Equation 2.7. The voltage of each cell y can be calculated as follows, see Equation 2.20.

$$U_{\text{cell } y} = U_{\text{cell } x} + I_x \cdot R_{c, x} - I_y \cdot R_{c, y} \quad (2.20)$$

Assuming that a battery cycler can regulate cells in both current and voltage modes, and given that each channel can access the real-time values of voltage and current from the other channels, a VPC

can be established. Figure 2.8 represents the schematic of the VPC for an n channel battery cycler.

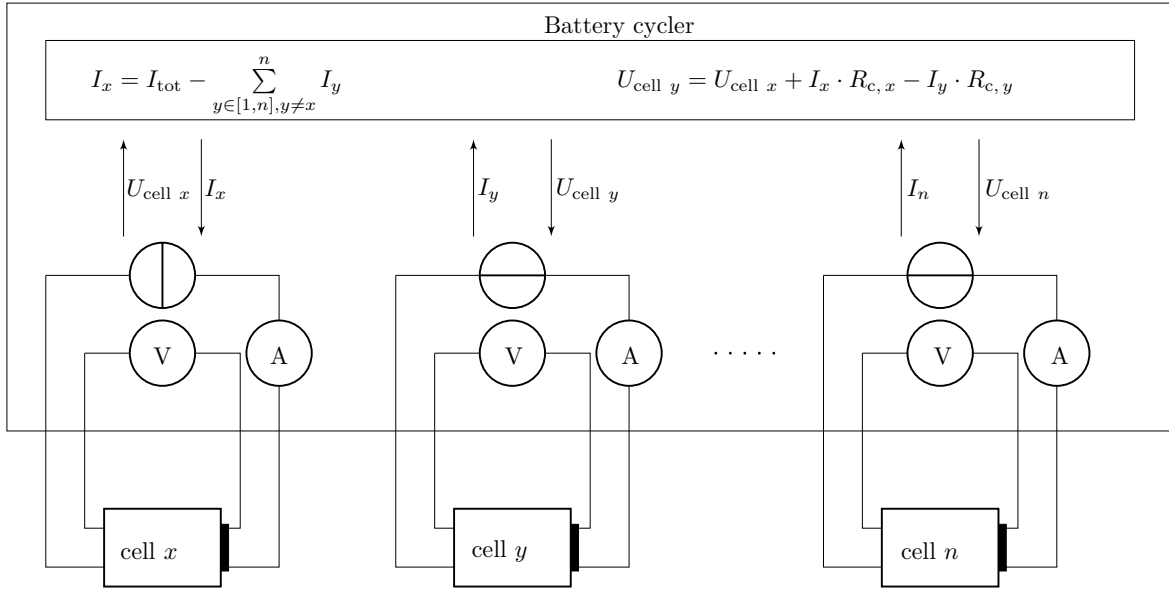


Figure 2.8: Schematic of the VPC within a n -channel battery cycler. Channel x corresponds to the master and is current-controlled. All other $n-1$ channels are voltage-controlled. The figure is based on the publication presented in Chapter 4 [15].

Specifically, there is one master and $n-1$ slave channels. The $n-1$ slave channels are voltage-controlled and have the task of maintaining the voltage of the master cell minus any contact resistances according to Equation 2.20. Depending on the voltage level and the cell parameters, a current I_y results. The master cell x , on the other hand, is current-controlled according to Equation 2.19.

Due to the parallel connection over equations, it is straightforward to scale from $2p$ to np . In addition, the interconnection can be carried out several times within a battery cycler to generate reproducible results simultaneously. This is particularly advantageous for aging studies to identify possible measurement outliers and make the results more reliable. Due to the virtual connection of the cells, it is possible to place them in different positions. This makes it very easy to investigate specific external influencing variables such as temperature on the system's behavior. Besides, each cell is connected with a 4-wire connection, therefore no undefined contact resistance occurs. If a resistance input is still desired, virtual resistances can be introduced according to Equation 2.20.

The VPC studies shown in this thesis were carried out with a Basytec CTS system. No changes were made to the software or hardware; the VPC was carried out using existing software tools. The method of the VPC should, therefore, be possible on all Basytec CTS devices.

The transient response to current steps is particularly a control engineering challenge. In Figure 2.3 b) the step response of the VPC shows an overshooting in the first calculation cycles. To eliminate this, the maximum currents were limited, in this case, to $130\% \cdot I_{\text{mean}}$. The transient response could be quantified within 3s for a $2p$ interconnection. For this thesis, all studies were carried out with a maximum current of $I_{\text{tot}} = 1\text{C}$. Over the entire SoC range, the influence of the transient behavior thus corresponds to less than 0.1%. It was, therefore assumed that this has no significant influence on the study's validity. However, this should be considered for fast charging studies where depending on the SoC, several current ranges are approached.

A disadvantage is the step response from a current step. To keep this to a minimum, it is advantageous to implement the methodology directly in the microcontroller and to design the control for a parallel circuit. Furthermore, as with all experimental studies, the battery cycler's accuracy must be considered. When applying inhomogeneous contact resistances, attention must be paid to whether the battery cycler can regulate the resulting voltage drop. It should also be noted that the contact resistance is applied virtually and only reflects the electrical behavior. This measurement methodology does not consider thermal influences from an inhomogeneous contact resistance.

3 Measurement and Determination of the Contact Resistance of Planar Contacts

The electrical contacts define a battery system. In order to understand and simulate the current distribution in parallel-connected cells, knowledge of the contacting is essential. The expected value, variances, and error cases should be known for different joining techniques.

An overview of well-established joining techniques was presented in Chapter 2.3.1. Electrical resistance, mechanical stability, heat input and possible damage during joining are essential for battery applications. Besides, the economic effort is a critical factor in choosing a joining technique.

Based on the publications of Brand et al. [102], this chapter adds a fourth joining technique using ECA. To investigate of copper and brass samples in dependence to the contact area, the adhesive's layer thickness, the R_C and UTF are analyzed and compared with well-established joining techniques. Overall, the examined adhesive exhibits both low contact resistance and high mechanical strength comparable to well-established joining methods like welding, detachable connections, and soldering. The mechanical and electrical parameters of the electrically conductive adhesives were assessed and economically evaluated in this thesis. This analysis highlighted that the material expenses of the adhesive substantially impact the total connection expenses. As a result, the effective costs in mass production are higher than those associated with laser beam welding. Thus, answering research question Q3: → *Q3 Which resistances result from ECA in comparison to well-established joining techniques?*

A quantitative evaluation of the factors that affect the measurement's accuracy, including the positioning, the measurement equipment, and the influence of the current injection on the sense pin, was conducted to achieve reliable measurement results. This evaluation addresses Q1: → *Q1 How can electric contact resistance be measured accurately?*

Two physical-based inhomogeneities were discussed in more detail: Firstly, fluctuations during the voltage measurement near the current injection point and contact connection, and secondly, the contact area of the connector is not necessarily resulting in a proportional decrease of the contact resistance.

Both inhomogeneities were first visualized within FEM simulation. After a mathematical analysis based on Poisson's equation and Gauss's law, the inhomogeneity near the current injection point can be determined. In summary, when considering the influence of the voltage distribution near the current injection, it is recommended to uphold a minimum distance between power and sense points equal to half the longest side length of the cross-sectional area of the specimen. Outside this area, a linear dependence results. In order to minimize measurement inaccuracies such as positional inaccuracies, measurements should be carried out outside this range. In addition, material-specific and geometric variables can only be determined in the linear range.

A recursive formula based on a branched ECM was defined to quantify the effective contact resistance to investigate the second inhomogeneity. Chapter 2.4.1 presents the developed method. In summary, the current distribution connections rely on the ratio between R_C and R_A . The correlation between contact resistance and contact area is non-linear. For very low contact resistances as $R_C < 0.01 \cdot R_A$,

the area does not define the effective contact resistance. Instead, the positioning of outer contacting lines should be as far away and as orthogonal as possible to the direction of the current. In contrast, for very high contact resistances $R_C > 100 \cdot R_A$, the area defines the contact resistance. In this case, an area-based contact resistance is justified. This answer Q2: \rightarrow *Q2 Is there an optimal design for cell connections to minimize electrical contact resistance?*

Authors Contribution

The study was designed and executed by Philipp Jocher with the help of Edgar Hoover, who was involved in the preliminary tests. Philipp Jocher conducted the electrical experiments and evaluated the experimental data. Michael Kick investigated the mechanical experiments. Manuel Rubio Gomez, Adrian Himmelreich and Alena Gruendl supported with mathematical and economic assessments. The manuscript was written by Philipp Jocher with the help of Michael Kick. Andreas Jossen and Michael Zaeh supervised the work. All authors discussed the data, commented on the results and reviewed the manuscript.

Determination of the Contact Resistance of Planar Contacts: Electrically Conductive Adhesives in Battery Cell Connections

Joher P., Kick K.M., Rubio Gomez M., Himmelreich A.V., Gruendl A., Hoover E., Zaeh M.F., and
Jossen A.

Batteries 2023, 9, 443

Permanent weblink:

<https://doi.org/10.3390/batteries9090443>



Reproduced under the terms of the Creative Commons Attribution 4.0 License (CC BY, <http://creativecommons.org/licenses/by/4.0/>), which permits unrestricted reuse of the work in any medium, provided the original work is properly cited.



Article

Determination of the Contact Resistance of Planar Contacts: Electrically Conductive Adhesives in Battery Cell Connections

Philipp Jocher ^{1,*}, Michael K. Kick ², Manuel Rubio Gomez ¹, Adrian V. Himmelreich ¹, Alena Gruendl ², Edgar Hoover ¹, Michael F. Zaeh ² and Andreas Jossen ¹

¹ Chair of Electrical Energy Storage Technology (EES), Department of Energy and Process Engineering, TUM School of Engineering and Design, Technical University of Munich (TUM), Arcisstr. 21, 80333 Munich, Germany; manuel.rubio-gomez@tum.de (M.R.G.); adrian.himmelreich@tum.de (A.V.H.); edgar.hoover@tum.de (E.H.); andreas.jossen@tum.de (A.J.)

² Institute for Machine Tools and Industrial Management (iwb), Department of Mechanical Engineering, TUM School of Engineering and Design, Technical University of Munich (TUM), Boltzmannstr. 15, 85748 Garching, Germany; michael.kick@iwb.tum.de (M.K.K.); alena.gruendl@iwb.tum.de (A.G.); michael.zaeh@iwb.tum.de (M.F.Z.)

* Correspondence: philipp.jocher@tum.de

Abstract: This study presents a method to analyze the electrical resistance of planar contacts. The method can determine whether the contact resistance of the joint exhibits linear or non-linear behavior. By analyzing the current distribution over a planar contact, it can be determined whether an area-based contact resistance is justified or if other parameters define the contact resistance. Additionally, a quantitative evaluation of the factors that affect the measurement accuracy, including the positioning, the measurement equipment used, and the influence of the current injection on the sense pin was conducted. Based on these findings, the electrical contact resistance and the mechanical ultimate tensile force of a silver-filled epoxy-based adhesive are analyzed and discussed. The layer thickness and the lap joint length were varied. Overall, the investigated adhesive shows a low contact resistance and high mechanical strength of the same magnitude as that of well-established joining techniques, such as welding, press connections, and soldering. In addition to evaluating the mechanical and electrical properties, the electric conductive adhesive underwent an economic assessment. This analysis revealed that the material costs of the adhesive significantly contribute to the overall connection costs. Consequently, the effective costs in mass production are higher than those associated with laser beam welding.

Keywords: electrical conductive adhesive; battery assembly; battery contacting; electrical contact resistance; batteries



Citation: Jocher, P.; Kick, M.K.; Rubio Gomez, M.; Himmelreich, A.V.; Gruendl, A.; Hoover, E.; Zaeh, M.F.; Jossen, A. Determination of the Contact Resistance of Planar Contacts: Electrically Conductive Adhesives in Battery Cell Connections. *Batteries* **2023**, *9*, 443. <https://doi.org/10.3390/batteries9090443>

Academic Editor: George Zheng Chen

Received: 1 August 2023

Revised: 23 August 2023

Accepted: 26 August 2023

Published: 29 August 2023



Copyright: © 2023 by the authors. Licensee MDPI, Basel, Switzerland. This article is an open access article distributed under the terms and conditions of the Creative Commons Attribution (CC BY) license (<https://creativecommons.org/licenses/by/4.0/>).

1. Introduction

Electrical connections are necessary for many mobile and stationary applications to connect lithium-ion batteries to an electrical load or charger. In addition to providing high mechanical strength, minimizing the electrical resistance is one of the most critical challenges in contacting lithium-ion batteries for electric vehicle (EV) powertrains and for stationary energy storage [1–4]. Depending on the application, individual target parameters must be optimized. Such parameters can include the maximum heat input during joining or cost. In order to manufacture electrical connections, a variety of joining techniques are commonly used. For instance, Das et al. [1] conducted a comprehensive review of joining techniques for battery packs, providing insights into resistance spot welding, laser beam welding, ultrasonic welding, soldering, and mechanical assembly techniques. Reichel et al. [5] investigated the joining for a hybrid busbar made of copper and aluminum using a forming process. Clamped cell connectors and their effect on the electrical contact resistance was investigated by Bolsinger et al. [6]. Brand et al. [2–4] assessed the contact

resistance (R_C) and ultimate tensile force (UTF) of welded, soldered, and press-contacted battery packs. Additionally, Wassiliadis et al. [7] investigated the influence of electrical contact resistance on lithium-ion battery testing for fast-charge applications.

Functional adhesives are an alternative to these well-established contacting techniques. They are generally defined as adhesives that fulfill a role beyond the adhesive's primary function of creating a mechanical bond between two substrates. They are typically thermally conductive adhesives (TCA) or electrically conductive adhesives (ECA). Due to their low processing temperatures, their ability to join dissimilar materials, and their reduced complexity for processing, ECA may have the potential as an alternative to currently widespread joining processes regarding R_C and UTF [8].

This paper aims to analyze the viability of functional adhesives for creating electrically conductive connections, with a particular emphasis on the current distribution in planar (area-based) contact resistances. Furthermore, this paper highlights the importance of quantifying and minimizing influencing factors of the measurement setup to achieve precise and reproducible results. Based on these findings, an ECA is quantitatively evaluated by geometrically simplified samples and compared to well-established joining techniques. The research objectives of this work are summarized as follows:

1. How does the setup influence the contact resistance measurement accuracy?
2. How can the contact resistance be determined as a function of the contact area?
3. How do the electrical and mechanical properties of the investigated ECA differ from those of welding, soldering, and press contacts as shown by Brand et al. [2–4]?

In this paper, planar contact refers to an electrical connection between two surfaces. The relationship between contact area and resistance is defined as an area-based quantity.

Electrical Joining Techniques

Welding is a vital joining technique for EV powertrains because it can provide mechanically robust electrical connections with low resistances [2]. Applicable welding techniques for battery applications include resistance spot welding, ultrasonic welding, and laser beam welding. Resistance spot welding generates a weld seam by passing a current from two electrodes through the joined components, rapidly heating the contact surface and melting the joining partners. It is best-suited for applications that require relatively thin connections. During the ultrasonic welding process, ultrasonic vibrations lead to the objects being scrubbed into each other until they are joined together. An advantage of this process is that the metal surface is exposed to the induced vibrations, which remove oxides and contaminants from the welding surface [9]. Furthermore, low process temperatures are needed for ultrasonic welding, which provide a significant benefit to weld battery terminals [2]. In addition, dissimilar materials can be joined using ultrasonic welding [10,11]. However, the joining components can be damaged during this process when materials with high hardness are used [2,9,12]. Laser beam welding uses laser radiation, which melts the joining components with a very precise weld seam at high welding speeds [13]. By adapting the weld seam trajectory [14], the temporal [15] or spatial [16] power distribution, or the wavelength of the laser radiation [17], a broad range of materials with varying thicknesses and desired weld seam properties can be joined.

Besides welding processes, electrical connections can also be manufactured by mechanical assembly. Press contacts and screwed joints provide a detachable alternative to welding and establish contacts by direct mechanical contact of the current-carrying members. Detachable joining techniques are desirable because of their reparability and ease of manufacturing, contributing to more sustainable EV powertrain systems and reducing the level of training required for personnel in manufacturing facilities [18]. Due to the reparability enabled by press contacts, this joining method is suitable for creating electrical connections at the battery-pack level. In addition, mechanical assembly typically does not require any heat input during manufacturing, further increasing the appeal of detachable contacts for battery assemblies and systems containing heat-sensitive electrical components [3,18].

Finally, soldering represents another joining technique. An additional material is melted into the joint by applying heat [19,20]. This third material is referred to as solder. Soldering is commonly applied in microelectronics applications and represents a proven process for creating connections between dissimilar materials [1]. Soldering has limited suitability for temperature-sensitive applications, such as lithium-ion batteries, as heat is necessary for this process to melt the solder.

A general comparison between welding, press contacts, and soldering concerning their electrical and mechanical performance was conducted by Brand et al. [2–4]. In their studies, contact resistance (R_C) and UTF were assessed as representative quantities for electrical and mechanical performance.

2. Basics of Electrically Conductive Adhesives

As defined in DIN EN 923, an adhesive is a non-metallic substance connecting two materials via surface adhesion. A sufficiently strong bond between the materials is created and maintained through cohesion [21]. Adhesives are polymeric materials composed of hydrocarbon-based monomer units that combine to form long polymer chains with a high degree of interconnection.

ECAs are composite materials comprised of a polymer adhesive matrix and electrically conductive fillers. Figure 1a shows a schematic of an isotropically conductive adhesive (ICA) joint cross section with a polymer binder, electrically conductive flakes, and resulting electrical conduction between two specimens. The resistances mentioned are categorized as follows: R_A and R_B represent the resistances of the specimens along the length of the lap joint, R_L denotes the resistance of the layer, and R_{S1} and R_{S2} represent the resistances of the surfaces. The combined sum of these resistances is defined as the lap joint resistance, denoted as R_L . According to Holm [22], the contact resistance (R_C) is defined as the sum of film or layer resistance (R_L), and the resistances of the surfaces (R_{S1} and R_{S2}) where the electrical conduction takes place within a-spots. While the polymer matrix provides the ECA with its mechanical properties, the conductive filler is responsible for enabling the electrical conductivity of the ECA [23,24]. In order to better understand how adhesives become electrically conductive, it is necessary to refer to the percolation theory of conduction [23]. Based on this theory, the conductivity of the ECA remains constant at low filler concentrations, providing only minimal conductivity of the bulk material. However, once the percolation threshold, as indicated by the vertical dashed line in Figure 1b, is reached, the conductivity increases dramatically. Increasing the filler material content beyond the percolation threshold typically yields diminishing returns and can lead to worse mechanical properties of the ECA [23]. The percolation threshold typically occurs at a volume fraction of 15–25%, although this value is dependent on the size and shape of the flakes [23]. Due to this behavior, ECAs can be categorized based on their placement within the graph shown in Figure 1b, where anisotropically conductive adhesive (ACA) and ICA represent the dominant categories of ECA. In contrast to ACAs and ICAs, non-conductive adhesives (NCAs) do not contain conductive fillers but provide a direct mechanical bond between contacting surfaces instead.

ACAs differ from ICAs in the direction of their conductive properties. While ACAs only conduct electricity in one direction, ICAs conduct electricity in all three dimensional directions. Below the percolation threshold, electricity cannot be conducted throughout the polymer matrix due to the low filler content.

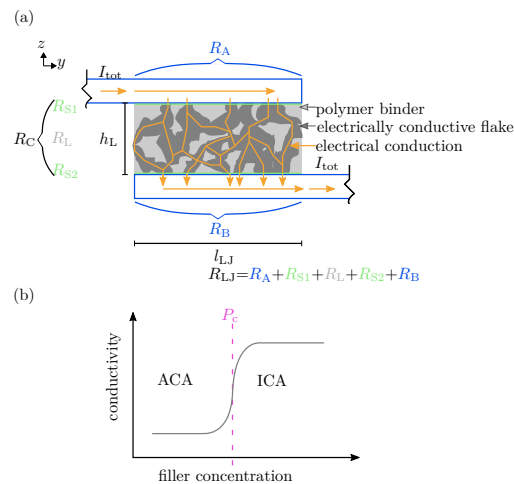


Figure 1. (a) Schematic of an isotropically conductive adhesive (ICA) joint cross-section with a polymeric binder, electrically conductive flakes, and the resulting electrical conduction between two specimens. I_{tot} : total current; h_L : adhesive layer thickness; l_{LJ} : layer length; R_A and R_B : specimen resistance over the lap joint length; R_L : layer resistance; R_{S1} and R_{S2} : surface resistance; R_{LJ} : lap joint resistance. (b) Qualitative percolation curve for electrically conductive adhesives (ECA), indicating the filler content regions for anisotropically conductive adhesive (ACA) and ICA, as well as the percolation threshold (P_c).

Above the percolation threshold, however, the filler particles create a three-dimensional conductive network, forming an ICA [23,25].

Besides the conductivity, another drawback of the application of an ACA is that heat and pressure are required during the curing process to ensure proper contact [23]. An ICA, however, does not necessarily require heat and pressure to form an adequate electrical contact. Depending on the properties of the polymer matrix of the ICA, the adhesive can be cured at room temperature, and the process can be accelerated by applying higher temperatures. For example, the silver-filled epoxy-based ICA from Polytec PT GmbH (PT EC 244) has a curing time of 24 h at room temperature, while curing can also occur in 15 min at 80 °C. This property of ICAs provides a significant advantage in scenarios where high-temperature curing is not feasible or desired. In the past, studies of ECA as an alternative to soldering in microelectronics were published, [24–30]. The present study, on the other hand, deals with high-current applications, which are also found in battery systems. Measurements are used to verify whether an area-based contact resistance is justified or whether other parameters determine the contact resistance. These findings can be applied to all contact techniques and to the design and optimization of contact connections. Additionally, R_C and UTF are compared with well-established joining techniques, such as welding, press connections, and soldering.

3. Experimental

Based on the studies of Brand et al. [2–4], two rectangular specimens, denoted as A and B and forming a lap joint, were investigated. Each specimen had dimensions of 50 mm × 15 mm and a lap joint length (l_{LJ}) with another specimen across a $l_{LJ} \times 15$ mm area. The adhesive layer thickness between the two specimens is defined by h_L . In comparison to Brand et al. [2–4], the sample thickness of the brass samples was increased to 2 mm to achieve a better measurement of the contact resistance ratio. Furthermore, four sense pins were used on each specimen, denoted as $A_{m=1\dots4}$ and $B_{n=1\dots4}$. Figure 2a shows the sample

layout. In order to achieve defined testing conditions between the two specimens, the layer thickness (h_L) was varied between 38, 89, and 124 μm , and the layer length (l_{LJ}) was varied between 5, 10, and 15 mm. Spacer particles in the above defined layer thicknesses from Rock West Composites Inc. were used. In a preliminary study, several adhesives were examined. These included PC 3001 from Heraeus and EC 262 and EC 244 from Polytec PT GmbH. EC 262 exhibited excessive resistance and was excluded from further investigations in this study. EC 244 and PC 3001 both showed very low contact resistance and high mechanical strength. However, PC 3001 was unsuitable for battery applications because it requires a curing temperature above 120 °C. Therefore, the silver-filled epoxy-based isotropically and electrically conductive adhesive from Polytec PT GmbH (PT EC 244) was used for all investigations reported in this paper.

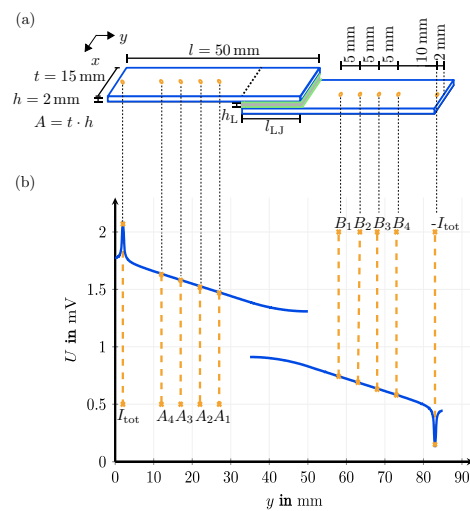


Figure 2. (a) Schematic view of the sample with current input and output points denoted by $\pm I_{tot}$, measurement points on specimens (A and B) denoted by A_m and B_n , where $m, n = 1 \dots 4$ are the dimensions of the specimens and relative locations of the current input and output, as well as measurement points; the dimensions in this schematic are not scaled. This figure is based on [2–4]. (b) finite element method (FEM) simulated voltage curve at $x = 7.5$ mm over y with resulting voltages at the measurement positions (A_m and B_n). The simulation was performed with a current of $I_{tot} = 5$ A across the sample. h_L : adhesive layer thickness; l_{LJ} : layer length.

3.1. Measurement of Electrical Contact Resistance

For an accurate and reproducible measurement, the influence of the measurement equipment, the positions of the sense pins, and the presence of inhomogeneities on the measurement must be known.

Therefore, measurements were carried out using an electrical contact tester developed by Li.plus GmbH based on the four-wire measurement principle. Each measurement contained a pulse series of five pulses, with a pulse duration of 25 ms. The two power and sense lines were twisted separately from to minimize electromagnetic interference. A current of 5 A was applied to the power lines, and the voltage was measured with the sense lines. In order to minimize position inconsistencies, a custom-made test fixture including gold-plated spring-loaded contact pins with a continuous plunger by Feinmetall GmbH was used, based on the geometry shown in Figures 2a and A1. This fixture contained two power pins to apply the measurement current ($\pm I_{tot}$) and eight sense pins on both speci-

mens, denoted by the subscripts $A_{m=1...4}$ and $B_{n=1...4}$, to measure the potential distribution between every combination of measurement pins (U_{A_m, B_n}). Therefore, all measurements had identical distances between the sense and power pins. With this high amount of sense points, position inconsistencies can be minimized, and the specific resistance of both specimens can be determined (see Section 3.1.3 Performing the Measurement). Furthermore, the measurements were performed automatically via a multiplexer (MUX).

As part of this experiment, the capability of the measurement process is proven according to the standards specified in German Association of the Automotive Industry (VDA) Volume 5. The accuracy of the contact tester without recontacting the power and sense pins was identified to a standard deviation of less than $3.634 \cdot 10^{-9} \Omega$ at an expected value of $70.47 \cdot 10^{-6} \Omega$ over 25 measurements. An additional influencing factor is the recontacting of the measurement pins to the same sample. Throughout 25 recontacting measurements, a standard deviation of less than $26.29 \cdot 10^{-9} \Omega$ was determined. This corresponds to a relative standard deviation of less than 0.0373%. With this measurement quality, the contact resistance in the expected order of magnitude of $1 \cdot 10^{-5}$ to $1 \cdot 10^{-3} \Omega$ can be reliably measured and analyzed. Hence, the commercial electrical contact tester developed by Li.plus GmbH was suitable. However, other electrical contact testers could also be employed, provided they demonstrate the same level of accuracy. Furthermore, at least five test samples were tested and averaged to achieve high accuracy and certainty.

Additionally, a simulation based on finite element method (FEM) was carried out to verify the influences of the measurement setup. Based on the experimental investigations, a model of a sample was implemented in COMSOL Multiphysics. The modeled brass sample ($\sigma_{brass_{A,B}} = 15.5 \cdot 10^6 \text{ S/m}$) consisted of a contact area of $15 \text{ mm} \times 15 \text{ mm}$, a homogeneous surface resistance of $2.25 \cdot 10^{-8} \Omega\text{m}^2$, and a third layer ($\sigma_L = 2 \cdot 10^5 \text{ S/m}$), which represents ECA. A current of 5 A across the surface ($\pm I_{tot}$) was applied. The ground potential of the simulation was set to the top of the negative power pin, which was modeled as a cylinder with a height of 0.1 mm and a radius of 0.1 mm. The specific surface resistance of the power pins was set to $675 \cdot 10^{-18} \Omega\text{m}^2$, and that of the layer was set to $2.25 \cdot 10^{-8} \Omega\text{m}^2$. The objective of the simulation was to demonstrate the effects of the measurement setup rather than to parameterize it based on the measurement outcomes.

All materials and contact conditions were assumed to be homogeneous and isotropic. The resulting voltage drop across $x = 7.5 \text{ mm}$ over y and the positions of the sense pins (A_m and B_n), as well as the current injection ($\pm I_{tot}$) are illustrated in Figure 2b. The voltage curve over y in Figure 2b shows two peaks. The first appears at the current injection at $\pm I_{tot}$, and the second appears around the contact area.

3.1.1. Phenomena at the Current Injection

The voltage peaks near the current injection point (I_{tot}) are now considered. Around this point, $x = 7.5 \text{ mm}$ and $y = 2 \text{ mm}$, a radially symmetrical equipotential field is formed. Figure 3a illustrates the equipotential lines on the sample's surface. The equipotential lines change from radially symmetrical to linear behavior as the distance from the point of current impingement increases (in the y direction in this case). An infinitely large surface is considered for the theoretical view of this phenomenon. As discussed by Precht [31], when a current is injected at any point on an infinitely large surface, an electric field with radially symmetrical behavior results. Therefore, the radially symmetrical behavior of the equipotential lines never ends. The resulting potential (ϕ) depends on the specific resistance (ρ), the injected current (I), and the radial distance (r), as illustrated in Equation (1) [31].

$$\phi = \frac{\rho I}{2\pi r} \quad (1)$$

If one dimension is finite, this behavior cannot be observed. Figure 3b represents the resulting potential from the FEM simulation along the y axis at $x = 7.5 \text{ mm}$. For a

comparison with linear behavior, according to Equation (2), the linear drop of the potential is depicted in Figure 3b.

$$R = \rho \frac{l}{A} \quad (2)$$

The greater the distance from the current impingement point (see Figure 3b), the closer the potential approaches the linear function. If the relative error is considered, as shown in Figure 3c, it is evident that this behavior of the potential is independent of the specific resistance of the investigated material but depends on the geometry of the specimen. An analogy was found in mechanics with the principle of Saint Venant. The principle of Saint Venant states that the inhomogeneity caused by a load on a long cuboid depends on its geometry. After a distance of at least half the longest side length of the specimen's cross-sectional area (A ; variable t in Figure 2a), the magnitude of the inhomogeneity is negligible, and the behavior becomes linear [32,33]. The same results are represented in Figure 3b. A mathematical analysis of the decaying behavior of the inhomogeneity is provided within Poisson's equation in Appendix C.1. The analytical equation represents how inhomogeneity influences the voltage curve concerning the geometrical dimensions (see Equation (A8)). The Transmission line model proposed by Murrmann and Widmann [34], as well as Berger [35], can demonstrate a similar phenomenon when modeling semiconductors.

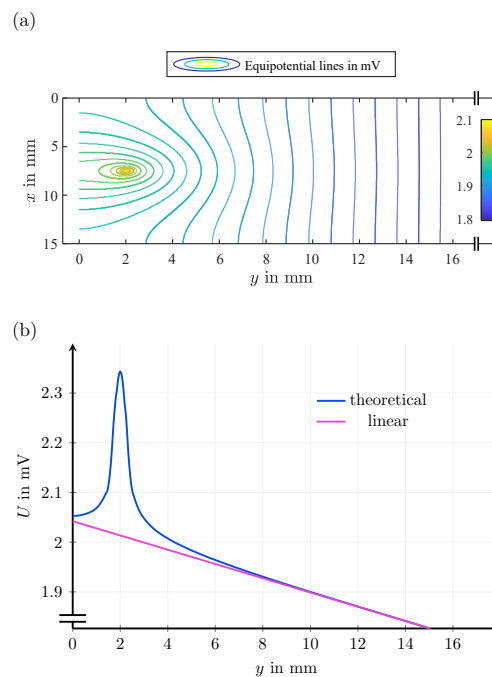


Figure 3. Cont.

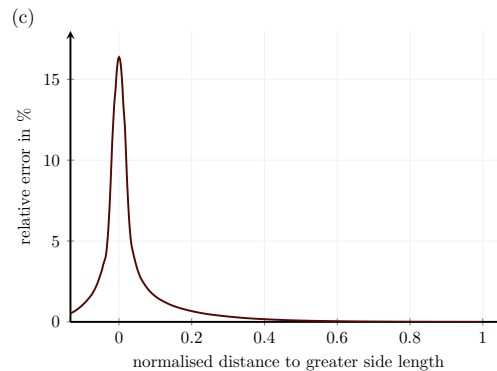


Figure 3. (a) Detailed view of a sample including the resulting electric equipotential lines with inhomogeneity at the current injection point at $x = 7.5$ mm and $y = 2$ mm, where inhomogeneous behavior results. The y axis is not completely displayed. (b) Detailed view of Figure 2, where the resulting potential and a theoretical linear voltage curve are represented across the horizontal axis at $x = 7.5$ mm. The voltage curve is affected inhomogeneously by the current impingement following the principle of Poisson's equation. (c) Relative error between the linear and theoretical voltage curve of (b) normalized to the longest side length of the specimen's cross-sectional area (A). According to the analytical solution, the error decays to zero for an increasing distance of greater side length than the specimen's cross-sectional area (A).

In summary, special attention must be paid to this influence when determining geometrical and electrical quantities. The linear equation of the resistance calculation according to the length (l), area (A), and specific resistance (ρ) (Equation (2)) can therefore only be used if the assumption is made that the material to be investigated is homogeneous and isotropic. Furthermore, the geometrical parameters of the sample are finite, and the measurement must be taken at a sufficient distance from the point of a current impingement.

The distance of the voltage measurement to the current injection point is essential to determine and compare the electrical contact resistance. Considering the impact of voltage distribution during current injection, it is advisable to maintain a minimum distance between power and sense points equivalent to half the longest side length of the cross-sectional area (A) of the specimen. This helps to minimize the error resulting from contacting below 0.05%, as illustrated in Figure 3c. Therefore, the measurements were carried out in the linear area to optimize the measurement results.

In order to compare samples to each other, a smaller distance between the power and sense pins can be chosen. As the distance to the point of current impingement decreases, as shown in Figure 3c, the local derivative of the voltage increases. However, special attention must be paid to the positioning of the voltage measurement. The closer the voltage measurement is located to the current impingement point, the greater the effect of a position inaccuracy on the measurement accuracy. The area of the power pin defines the maximum voltage peak at the current injection point. A thinner power pin results in a higher voltage peak. In contrast, a large homogeneous area-based current injection results in a lower voltage peak.

Another factor that must be considered to determine the contact resistance is the ratio between the contact resistance and the measured total resistance, which should be close to 1. If the ratio is too small, slight variations in the geometry, material, and positioning of the measurement pins can significantly impact the quality of the measurement. In order to keep the quality of the results high, thicknesses of 2 mm and 0.2 mm were chosen for the brass and copper samples, respectively.

3.1.2. Method to Calculate the Electrical Connection Resistance within Planar Contacts

After having defined a measurement procedure and having identified the influences on the measurement, the calculation method within planar contacts for electrical connection resistance is discussed. For this purpose, the first step is to answer the questions as to how the contact resistance is obtained and how it can be determined. Similarly to soldered connections, a third conductive material is added between two specimens for adhesive connections. With the additional conductive partner, the resistance is split into the resistances of the specimens, (R_A and R_B); the contact resistance (R_C), which is the sum of the surface resistance between the specimens and conductive adhesive; R_{S1} and R_{S2} ; and the resistance of the conductive adhesive layer (R_L). The value of R_C can be determined based on the values of R_A , R_B and R_L , which are known parameters.

Additionally, as a planar contact is obtained when using an adhesive, the current distribution over this planar area needs to be investigated. To justify an area-based contact resistance, a parameter study in an FEM-simulation was performed. For all studies, a homogeneous surface resistance was used.

Figure 4 shows the normalized current through specimen *A* over the normalized lap joint (l_{LJ}) in the *y* direction. Four different values for the contact resistance (R_C), which depend on R_A and R_B , were chosen. Additionally, it is assumed that the current does not flow across the third partner. This phenomenon results when the layer thickness is small and the specific resistance of the third conductive partner is sufficiently high. As shown in Figure 4, three cases were investigated to demonstrate the influence of low, high, and two different medium contact resistances on the current distribution over the lap joint.

For this simulation analysis, the previously defined parameters were used ($\sigma_{\text{brass}_{A,B}} = 15.5 \cdot 10^6 \text{ S/m}$ and $A_{A,B} = 2 \text{ mm} \times 15 \text{ mm}$).

High contact resistance: A high specific contact resistance ($R_{C_A} = 1 \cdot 10^{-8} \Omega\text{m}^2$) results in a linear current distribution through the contact area, indicated by the orange line in Figure 4. The current through specimen *A* decreases linearly. The current flows homogeneously through the contact area, and a larger contact results in a lower contact resistance. In this case, the contact area determines the magnitude of the contact resistance.

Low contact resistance: A low specific contact resistance, e.g., $R_{C_A} = 1 \cdot 10^{-11} \Omega\text{m}^2$, results in two separate current flows: one at the beginning and one at the end of the lap joint, as represented by the brown line in Figure 4. Although an electrical connection is present over the whole area between the specimen and the adhesive, only a minimal current flows through the middle of the specimen. This leads to the current remaining within the specimen and remaining constant. The current is divided according to the resistance of the specimens and forms an ideal parallel connection, resulting in non-linear behavior between the contact area and the resulting resistance. The distance between the contact area's start and end primarily defines the contact resistance.

Medium contact resistance: Specific contact resistance in the range between the two cases discussed above ($R_C = 1 \cdot 10^{-9} \Omega\text{m}^2$ and $R_{C_A} = 1 \cdot 10^{-10} \Omega\text{m}^2$) results in a non-linear current distribution through the contact area, as represented by the pink and blue lines in Figure 4, respectively. Additionally, the current through the middle of the lap joint at $l_{LJ} = 7.5 \text{ mm}$ in Figure 4 is divided according to the resistance ratio of both specimens (R_A and R_B).

In summary, no straightforward relation between contact resistance and contact area exists. However, the contact resistance does depend on the resistance ratio (R_C/R_A). The assumption of Brand et al. [4] to use a simplified version of the Equivalent Circuit Diagram (ECD) for area-based resistance is only valid if the contact resistance is lower than the resistance of the specimens. Additionally, Schmidt [36] analyzed the influence of the weld seam's position on electrical properties. The connection showed the lowest resistance with two weld seams that were aligned as far apart as possible. This can be extended analogously to low contact resistance.

Generally, it cannot be stated that a larger contact area leads proportionally to a lower contact resistance. For the geometry investigated in this work, the primarily target is not to contact a large surface but to place the contact points as far apart as possible and to establish a parallel connection. The results of this study are relevant to all types of joining techniques and can be utilized to optimize and design the joining layout. For other geometries, such as cylindrical cells, the inner structure of the geometry has a significant influence. In this case, the contact points should be selected depending on the internal current flow. Lin et al. [37] defined this phenomenon at the end of the contact region as “current crowding” by investigating the wafer bonding process of microelectromechanical systems.

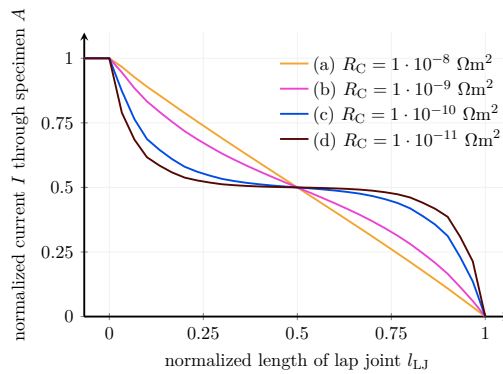


Figure 4. Detailed view of the normalized current through specimen A. Four different values for the specific contact resistance (R_{C_A}) concerning the resistance of the specimens ($R_A = R_B$) and the resistance of the added layer show their influence on the current distribution over the lap joint (l_{LJ}) in the y direction.

Nevertheless, the question of how to determine the contact resistance (R_C) remains. For the analytical solution, the measured resistance over the lap joint (R_{LJ}) and the resistance of the two specimens (R_A and R_B) are defined as known quantities, and the contact resistance is defined as the desired quantity. The branched electrical circuit model (ECM) relationship and the following simplified recursive formula (see Equation (3)) are derived in Appendix D.

$$\begin{aligned}
 R_{LJ}^k(r_a^k, r_b^k, r_a, r_b, r_c) &= s_a + R_{LJ}^{k-1}(\tilde{r}_a^{k-2}, \tilde{r}_c^{k-1}, r_a, r_b, r_c) \\
 &\quad \text{with } \tilde{r}_a^{k-2} = r_a^{k-2} + s_b \text{ and } \tilde{r}_c^{k-1} = s_c \\
 &= \frac{r_a^k(r_b + r_c^k)}{r_a^k + r_b + r_c + r_c^k} \\
 &\quad + R_{LJ}^{k-1}(\tilde{r}_a^{k-1}, \tilde{r}_c^{k-1}, r_a, r_b, r_c) \\
 &\quad \text{with } \tilde{r}_a^{k-1} = r_a + \frac{r_a^k r_c}{r_a^k + r_b + r_c + r_c^k} \\
 &\quad \text{and } \tilde{r}_c^{k-1} = \frac{r_c(r_b + r_c^k)}{r_a^k + r_b + r_c + r_c^k}
 \end{aligned} \tag{3}$$

Variables s_a , s_b , and s_c represent resistance after a Δ -star transformation (see Appendix D). Equation (3) is only valid if it is assumed that no current flows across the third partner in the y direction. The resistors (r_c) correspond to the equivalent circuit of a conductive adhesive joint, as illustrated in Figure A6.

Figure 5b depicts an example of the graphical determination of the contact resistance (R_C) in the case of $R_A = R_B$ based on Equation (3). With a contact resistance of $R_C = 0$, an ideal parallel connection results and the R_{LJ}/R_A ratio is equal to 0.5. Furthermore, linear behavior results at high contact resistance (R_C). For a better understanding of the cases discussed above, Appendix C.1 discusses the resulting analytical contact resistance of a branched network. A similar result was published by Euler and Nonnenmacher [38].

3.1.3. Performing the Measurement

A fixture over an extruded aluminum rail was constructed to minimize possible position fluctuations. A picture is provided in Figure A1. Additionally, the distance between the power and sense pins for this investigation was set to a minimum of 10 mm to achieve an error below 0.05%. The distances between A_m and $B_{n=1...4}$ were set to 5 mm, (c.f. Figure 2). Finally, all reasonable combinations of the sense pins (A_m and B_n) were measured via an MUX. Figure 5a exemplarily illustrates the measured resistances used within a linear interpolation to l_{LJ} to determine R_{LJ} . The distance (d_{LJ}) is defined as the difference in the spacing between the sense pins (A_m and B_n) and the overlap length (l_{LJ}). Assuming two identical specimens ($A=B$) are connected to each other, the specific resistance of the material can also be determined via the slope (m) and the specimen's cross-sectional area (A) (see Equation (4) and Figure 5a).

$$\rho_{A,B} = m_{A,B} \cdot A_{A,B} \quad (4)$$

Subsequently, the recursive formula (Equation (3)) is solved based on the material resistance across the lap joint (R_A and R_B) and the resistance (R_{LJ}), as shown in Figure 5b. The contact resistance (R_C) can then be determined via the relationships of R_{LJ} over R_A and R_C over R_A .

Theoretical considerations can be utilized, regardless of the measuring device and joining technique. The subsequent analysis examines and compares electrically conductive adhesives with other well-established techniques. Moreover, the behavior of the ratio between contact resistance and contact area is demonstrated.

As specified by the manufacturer, the adhesive was mixed at a gravimetric ratio of 100:10 (resin (part A) to hardener (part B)), with an additional gravimetric 1% of spacer particles. Each sample was pressed with a weight of 60 g and cured for at least 24 h at room temperature. For each thickness (h_L), a separate batch of the two-component adhesive was mixed. Thus, measurement data with the same adhesive thickness (h_L) can be compared, and a scattering of the adhesive batches among each other can be assumed to be negligible. Before adhesive bonding, each specimen was cleaned with isopropanol to minimize surface inaccuracies between samples.

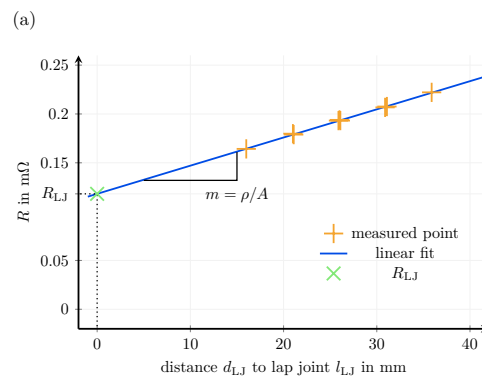


Figure 5. Cont.

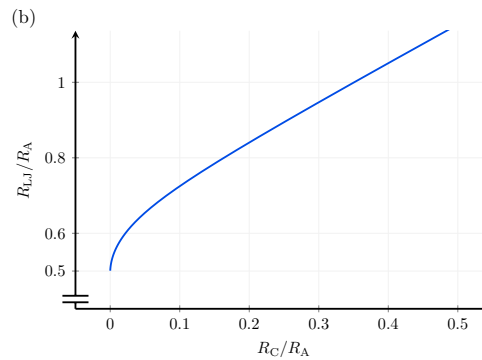


Figure 5. (a) Measured points within a linear interpolation to l_{LJ} and R_{LJ} . The distance (d_{LJ}) is defined as the difference of the spacing between the sense pins (A_m and B_n) and the overlap length (l_{LJ}). (b) Graphical determination of the contact resistance according to Equation (3) when $R_A = R_B$.

In order to determine the UTF of the samples joined with ECA, tensile tests were performed using the a Zwick Roell Z020 universal testing machine (UTM) according to DIN EN 2243-1. Beyond the UTF of the lap joints, tensile tests can also provide additional information. In particular, an analysis of the fracture mechanisms provided insights into the joint's limitations and the quality of the manufactured joint. Adhesive, cohesive, and substrate fracture mechanisms were expected from these tensile tests. While an adhesive fracture is caused by adhesion between the adhesive and substrate being the weakest point, a cohesive fracture results from broken bonds within the adhesive. In the case of a substrate fracture, the specimen material's tensile strength is lower than that provided by the adhesive's adhesion and cohesion. In this context, a substrate fracture provides the least information concerning the adhesive's mechanical properties [39].

4. Results

In order to pursue the research objectives specified in Section 1, a variety of testing methods and materials were used to investigate dependencies in the contact area, the adhesive's layer thickness, and specimen material concerning the R_C and UTF. Table 1 shows the measured properties. The failure mechanism for UTF determination involved either adhesive (A) or cohesive (C) fracture. In addition to the expected value (μ) and 90% confidence interval (CI) of the R_C and UTF, the ratio of R_{LJ}/R_A is also provided in Table 1. The number of test samples for each step was five.

As expected, all measurements demonstrate a low R_C and high UTF for an increased contact area. In addition, the results indicate a significant influence of the used specimen material on the contact resistance. The copper samples exhibit lower R_C and UTF values. This can be attributed to different surface properties of the copper and brass samples, (R_{S1} and R_{S2} [40]). The increasing adhesive layer thickness deteriorated the contact quality, leading to an increase in the R_C and a decrease in the UTF. This was also discovered for the mechanical strength by Habenicht [40].

Among the brass samples, excluding the sample with the thickest adhesive layer (124 μm), a cohesive (C) fracture occurred. The brass samples with a 124 μm adhesive layer thickness and all copper samples showed adhesive failure (A). This is also visible in the UTF measurement results in Table 1. The corresponding force–displacement curves are illustrated in Appendix B, Figure A2. Similar to the results of Habenicht [40], an increased lap joint length enhances the UTF, whereas with higher layer thickness, the UTF decreases. Figure 6b displays an example of a cohesive (C) fracture of silver-filled two-component epoxy-based adhesive with a contact area of $10 \times 15 \text{ mm}^2$ and a layer thickness of 38 μm .

Table 1. Measurement results regarding the dependencies of the contact area, the adhesive's layer thickness, and the specimen material (copper (Cu) or brass (Br)), on the contact resistance (R_C) and the ultimate tensile force (UTF). Results are presented as the expected value (μ) and 90% confidence interval (CI). Additional fracture mechanisms from the tensile tests are indicated as adhesive (A) or cohesive (C) fractures. The number of test samples for each step was five.

Specimen Material	l_{LJ} in mm	h_L in μm	R_C		UTF		Fracture	R_{LJ}/R_A μ
			μ in $\mu\Omega$	CI in $\mu\Omega$	μ in N	CI in N		
Copper	5	38	42.78	29.55	283.6	114.7	A	2.428
	10	38	19.74	12.61	417.0	20.93	A	1.080
	15	38	10.53	3.478	515.7	271.1	A	0.7872
Brass	5	38	162.8	87.09	1862	145.6	C	15.32
	10	38	86.02	22.94	2165	279.0	C	4.536
	15	38	74.62	26.16	2519	252.4	C	2.902
Brass	10	38	86.02	22.94	2165	279.0	C	4.536
	10	88	109.5	58.36	2400	87.54	C	5.591
	10	124	306.5	57.65	2112	165.7	A	14.46

Given that the influences of measurement were quantified and reduced in the preceding section, it is assumed that the sample scatter is substantial, despite the use of isopropanol to clean the surfaces. Furthermore, it can be affirmed that the variation was reduced for a larger area, which may be attributed to the bonding process employed in the laboratory. Nevertheless, it can be concluded that the contact resistance is characterized by low magnitudes of $10.53 \mu\Omega$ and $74.62 \mu\Omega$ when considering the expected values in an area of $15 \times 15 \text{ mm}^2$.

In general, an increased contact area results in lower contact resistance. For both investigated materials, increasing the lap joint length (L_{LJ}) from 5 to 10 mm reduces the R_C by about half its value. This correlation is invalid if the length is increased to 15 mm, which is three times the original length. In this case, the theoretical knowledge from Figure 5b and the R_{LJ}/R_A relation are considered. The linearity of R_C 's behavior depends on R_{LJ}/R_A when non-linear or linear behavior of the R_C is present, assuming a contact-area-related resistance is only justified with a linear ratio, as described in Section 3.1.3. However, this does not hold true for copper and brass substrates. The R_C is not in the linear domain. In this range to a first approximation, the contact resistance is no longer determined by the contact area but by the distance between the first and last contact conditions. An ideal parallel circuit can be assumed as a limiting value, and the R_{LJ}/R_A ratio converges toward 0.5. This statement is valid as long as a relatively thin layer of the ECA is applied and the conductivity of the adhesive is higher than the conductivity of the specimen material. If the third conductive partner is thicker and has very high conductivity with respect to the metal to be joined, the ratio can be less than 0.5. In that case, a current flows through the additional conductive partner in the y direction. The contact conditions keep the resistance low, as is the case when both materials are ideally connected.

In order to assess the layer thickness and the uniformity of the adhesive bonds, microscopic images were captured using a Keyence VR 3100 profilometer. Figure 6a indicates the layer thickness from the intended $124 \mu\text{m}$ spacer. It is apparent, however, that the layer thickness is not entirely uniform across the adhesive layer. In this case, it has a thickness of approximately $130 \mu\text{m}$. Additionally, Figure 6a illustrates that the two specimens were bonded parallel to each other.

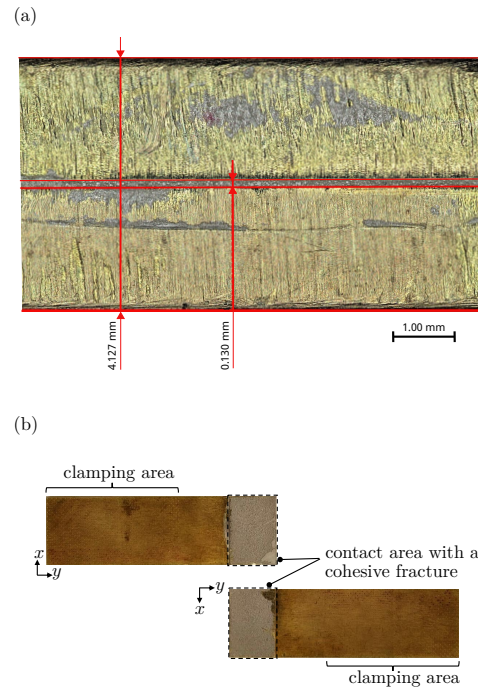


Figure 6. (a) A section of the adhesive layer containing the $124\ \mu\text{m}$ spacer particles along the long edge of a brass sample using a layer thickness measurement. The total thickness of the lap joint was $4.127\ \text{mm}$, and the thickness of the adhesive layer was $130\ \mu\text{m}$. (b) Picture of a brass sample after tensile test. Cohesive (C) fracture of silver-filled two-component epoxy-based adhesive; contact area of $10 \times 15\ \text{mm}^2$ and layer thickness of $38\ \mu\text{m}$. Figure A2 shows the corresponding force–displacement curve.

4.1. Comparison of Joining Techniques in Terms of Electrical Connection Resistance and Ultimate Tensile Force

In this section, the investigated ECA is compared to other electrical joining techniques regarding R_C and UTF, which results from the brass substrate. Figure 7 shows the R_C of ECA in comparison to soldering, spot welding, ultrasonic welding, laser beam welding, and press contact, which were investigated by Brand et al. [4]. The abscissa from Brand et al. [4] was applied to depict the ECA for soldering and press contact. Caution regarding the ECA abscissa is required, as the abscissa exhibits a linear progression up to 225 in 45 increasing intervals. However, starting from 225, the interval between the values increases to 75. The contact areas of the ECA are $5 \times 15\ \text{mm}^2$, $10 \times 15\ \text{mm}^2$, or $15 \times 15\ \text{mm}^2$. According to the investigated brass samples, ECA lies in the range between welding and soldering. With a contact resistance of $74.62\ \mu\Omega$, it exhibits the lowest resistance compared to the connection techniques investigated by Brand et al. [4]. Contrary to Brand et al. [2–4], the brass samples in this study were measured with a thickness of $2\ \text{mm}$ to minimize the measurement errors (see Section 3.1.1). Additionally, Brand et al. [4] conducted experiments with the BT3562 measurement unit of the Hioki E.E. Corp.. The alternating measurement current was set to $100\ \text{mA}$ at a frequency of $1000\ \text{Hz}$.

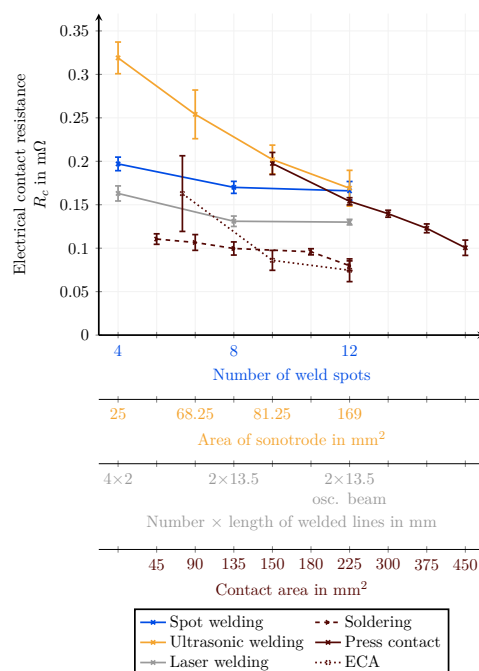


Figure 7. Comparison of brass samples connected by soldering, spot welding, ultrasonic welding, laser beam welding, and press contact with a thickness of and 38 μm electrically conductive adhesives (ECA) concerning contact area. Separate abscissas were necessary due to the different characteristics of each connection technique. Graphs include the 90% confidence interval (CI). Data of soldering, spot welding, ultrasonic welding, laser beam welding, and press contact refer to the publications of Brand et al. [2–4]. Please be aware that the scale is not linear.

In addition, the UTF of well-established joining techniques was compared to the respective ECA. Figure 8 provides a quantitative overview of ECA, soldering, spot welding, ultrasonic welding, laser beam welding, and press contact. Again, Brand et al. [4] provided the data on well-established joining techniques. The soldered specimens fractured due to material fatigue and did not break at the joint. As previously mentioned, specimens ten times thicker were used in this work and reached the highest mechanical tensile force of 2519 N at a contact area of $15 \times 15 \text{ mm}^2$ with ECA.

4.2. Discussion

The present study illustrates that electrically conductive adhesives (ECA) can achieve similar magnitudes of electrical conductivity and mechanical strength as those attained by well-established electrical contacting techniques. While several ECAs were assessed, only PT EC 244 exhibited results comparable to those of well-established joining techniques for battery applications. Consequently, only one adhesive is presented here. Furthermore, while the copper samples exhibited a lower electrical contact resistance than brass, the brass samples had higher mechanical strength. These two characteristics are assumed to depend on the condition between the specimens' surfaces and the adhesive. The characteristics can be transferred with regard to the condition of the specimens. In addition, ECA demonstrates several advantages over well-established electrical joining techniques. Depending on the adhesive, the gluing process does not require heat input for soldering or welding. It is,

therefore, suitable for temperature-sensitive components, such as lithium-ion batteries [4]. Due to the lack of heat input, no residual stresses remain in the connection after the joining process.

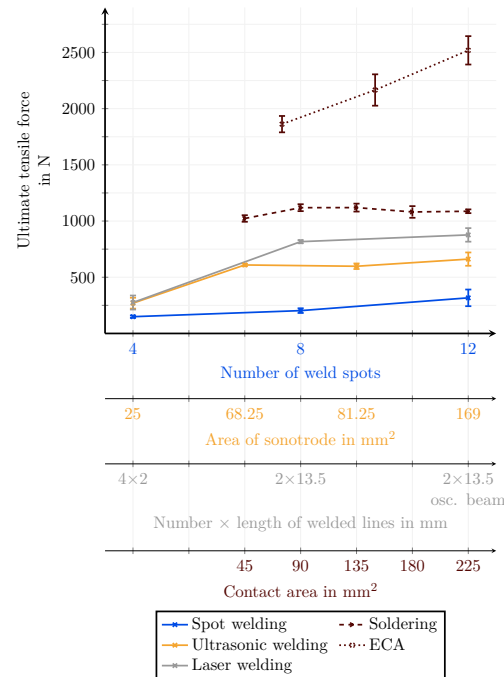


Figure 8. Comparison of ultimate tensile forces for brass samples connected by soldering, spot welding, ultrasonic welding, and laser beam welding with an electrically conductive adhesive (ECA) thickness of and $38\ \mu$. Graphs include the 90% confidence interval (CI). Data on soldering, spot welding, ultrasonic welding, and laser beam welding refer to the publications of Brand et al. [2–4]. Please be aware that the scale is not linear.

However, disadvantages are that the adhesive is cost-intensive, and scattering of the joint's properties can also occur in small quantities. Furthermore, the adhesive requires a resting period for curing, which can be shortened by heat input. The adhesive used in this experiment was cured at room temperature for 24 h. In particular, a pot time of 15 min could make this method problematic in many of the assembly processes for manufacturers. However, if a high temperature does not harm the application, PC 3001 from Heraeus can also be considered as a possible adhesive. An internal preliminary study showed similar electrical resistance and mechanical strength results compared to the investigated EC 244 from Polytec. However, PC 3001 was unsuitable for battery applications because it required a curing temperature of over $120\ ^\circ\text{C}$.

The electrical contact resistance is not just determined by the process and material composition but also by the geometrical and electrical parameters of the elements being connected and the arrangement of the contact points. As demonstrated in this paper, it is not necessarily a larger contact area that is important but the distance between the two outer contact lines. This should be taken into account when evaluating the electrical contact resistance.

4.3. Economic Evaluation

The resulting electrical and mechanical joint properties are visualized in Figures 7 and 8 in comparison to other joining techniques. Since laser beam welding is commonly used for mass production in battery contacting, it was used as a reference for the economic assessment of ECA. To manufacture planar contacts using ECA, a plant producing adhesives worth EUR 50,000 was defined. For laser-based joining, a setup that includes a laser cell, chiller, laser beam source, and scanner optics for EUR 455,000 was assumed. The costs for both systems were requested from the respective manufacturers. For both joining processes, the machine costs per hour were calculated according to VDI guideline 3258 A, where the machine costs per hour, the labor costs, and the cycle times are considered. Appendix E, Tables A1 and A2 provide a detailed overview of the costs. For ECA, there are two different curing approaches. On the one hand, a temperature of 80 °C can be applied for 15 min, whereas, on the other hand, curing can take place at room temperature for 24 h. Since the former may harm the battery cell, the latter was chosen. Regarding the calculation, additional space for curing was considered and approximated by a square that fits a cylindrical cell (18 mm by 18 mm for a 18,650 cell, for example). Figure 9 shows a comparison of the two joining methods.

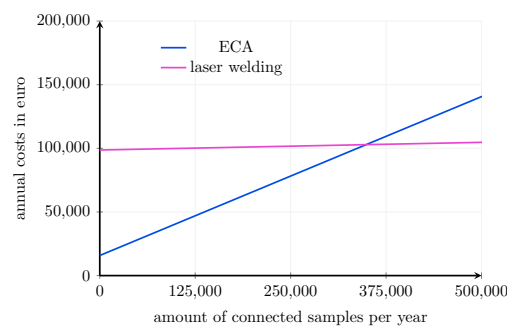


Figure 9. Comparison of the annual costs for the manufacturing of planar contacts using electrically conductive adhesives (ECA) or laser beam welding. For both joining processes, the machine costs per hour were calculated according to VDI guideline 3258 A, where the machine costs per hour, the labor costs, and the cycle times are taken into account. The contact area was calculated based on 90% of the area of a 18650-cell positive pole.

Furthermore, it was considered that the costs of a connection for ECA depend on the joined area. A selection of joining areas for frequently used cell geometries and the accompanying costs for ECA and the spacers are provided in Figure 10. A detailed overview of the calculation is listed in Appendix E, Table A3. A large cost factor is the material costs of the adhesive. In this publication, a price of 5 kg was used for the calculation. It is assumed that this cost will decrease with mass production.

Figure 9 clearly demonstrates that the costs for ECA in series production are significantly higher than those for laser beam welding. Nevertheless, ECAs is competitive with established joining processes concerning physical properties. This is why ECA may be a suitable alternative to manufacturing planar contacts for prototyping and development projects.

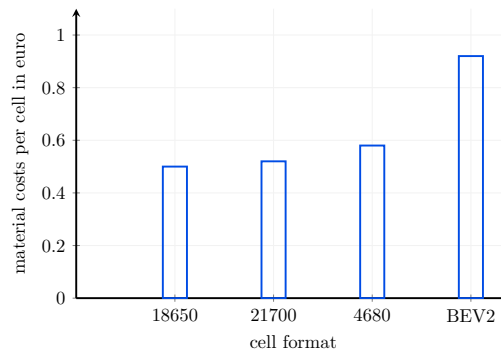


Figure 10. Costs of electrically conductive adhesives (ECA) and spacers for different cell formats per planar contact in EUR. For the calculation, 90% of the area of the positive pole was used for both poles.

5. Conclusions

This study introduces a method to analyze the electrical resistance of planar contacts based on their area. The method allows for identification of whether the contact resistance of the joint demonstrates linear or non-linear behavior. It is suitable for all electrical connection techniques and can help to optimize contact geometries. Based on this, electrical adhesive connections were analyzed based on their electrical and mechanical properties and through an economic assessment and compared with well-established contacting techniques.

Regarding the first research question, it was demonstrated that current injection considerably influences voltage measurement and accuracy. The former is particularly important when determining electrical parameters and when high accuracy is required. Through mathematical consideration, the error between the linear and the theoretical values was determined using Poisson's equation. The error decays to zero depending on the sample's dimensions. The distance between the power and the sense pins should be set to a minimum of half of the longest side length of the specimen's cross-sectional area (A). Concerning the second research question, the current is divided according to the resistance of the specimen and the contact. For this purpose, a correlation was mathematically determined to verify whether the measurement occurs in a non-linear or linear relationship between contact area and contact resistance. According to the derived method, the current is divided by the current divider in the non-linear range. In this case, the contact resistance is primarily affected by the length of the contact area but not by the cross-sectional area. Finally, based on the third research question, epoxy-based silver-filled adhesive joints were compared to other well-established contacting techniques [2–4], such as welding, press connections, and soldering, and were found to have a low contact resistance and a high mechanical strength. For brass samples with a contact area of $15 \times 15 \text{ mm}^2$ and a thickness of $38 \text{ }\mu\text{m}$, an electrical contact resistance of $74.62 \text{ }\mu\Omega$ and an ultimate tensile force of 2519 N were observed.

Moreover, an economic assessment was conducted to compare the investigated ECA and the equipment for laser beam welding. The results indicate that for series production, costs for ECA are significantly higher than for laser beam welding. It is assumed that the cost of ECA will decrease with mass production. However, ECAs is competitive with established joining processes concerning electrical and mechanical properties.

Further studies should be conducted in an attempt to minimize sample scatter in the form of pretreated materials. Other environmental influences, such as humidity and temperature, on the contact resistance (R_C) or the current-carrying capacity should be investigated. Another interesting research topic is the aging behavior of the joints under the influence of the abovementioned environmental aspects.

Author Contributions: Conceptualization, P.J.; methodology, P.J. and M.R.G.; software, P.J.; validation, P.J. and A.V.H.; formal analysis, P.J., M.K.K. and M.R.G.; investigation, P.J., M.K.K., A.G., A.V.H. and E.H.; resources, M.F.Z. and A.J.; data curation, P.J.; writing—original draft preparation, P.J.; writing—review and editing, P.J., M.K.K., M.R.G., A.G., M.F.Z. and A.J.; visualization, P.J.; supervision, A.J.; project administration, A.J.; funding acquisition, M.F.Z. and A.J. All authors have read and agreed to the published version of the manuscript.

Funding: This research was funded by the German Federal Ministry of Education and Research (BMBF) and the German Federal Ministry of Economic Affairs and Climate Action (BMWK) via the OSLiB research project (grant number 03X90330 A) and ultraBatt (grant number 01MV21015D). The projects were overseen by Project Management Juelich (Ptj) and DLR Projektträger, respectively.

Data Availability Statement: Data are available upon request.

Acknowledgments: The authors thank Korbinian Schmidt, Chair of Electrical Energy Technology at the Technical University of Munich, for supporting the investigations with practical workmanship.

Conflicts of Interest: The authors declare no conflict of interest. The funders had no role in the design of the study; in the collection, analyses, or interpretation of data; in the writing of the manuscript; or in the decision to publish the results.

Abbreviations

The following abbreviations are used in this manuscript:

A	adhesive
ACA	anisotropically conductive adhesive
CI	confidence interval
C	cohesive
ECD	Equivalent Circuit Diagram
ECM	electrical circuit model
R_C	contact resistance
ECA	electrically conductive adhesives
EV	electric vehicle
μ	expected value
FEM	finite element method
ICA	isotropically conductive adhesive
UTF	ultimate tensile force
MUX	multiplexer
NCA	non-conductive adhesive
UTF	ultimate tensile force
UTM	universal testing machine
TCA	thermally conductive adhesives
VDA	German Association of the Automotive Industry

Appendix A. Test Bench

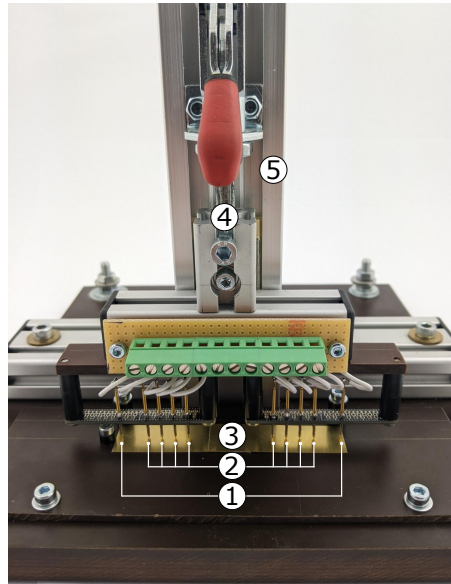


Figure A1. Custom-made test bench including gold-plated spring contact pins with a continuous plunger by Feinmetall GmbH. It contains two power pins ① to apply the measurement current and eight sense pins ② to measure the potential distribution over the sample under test ③. The geometric dimensions of the contact pins can be taken from Figure 2. The fixture ⑤ over the extruded aluminum rail ④ was used in order to minimize fluctuations in position.

Appendix B. Force–Displacement Curve

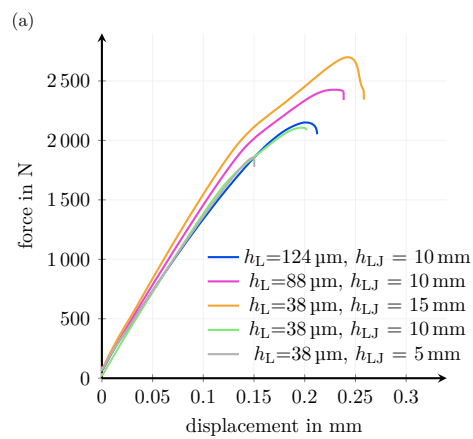


Figure A2. Cont.

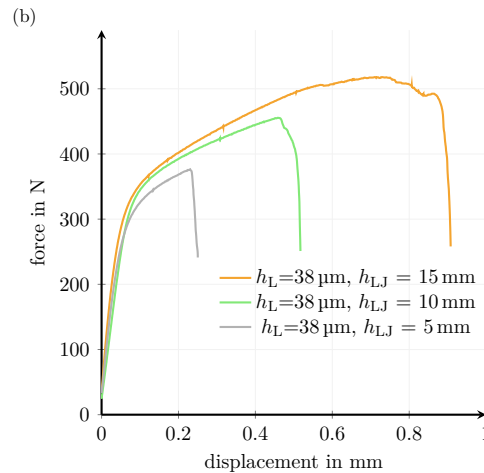


Figure A2. Force–displacement curve of brass (a) and copper (b) samples for different adhesives layer thicknesses and lap joint lengths.

Appendix C. Theoretical Consideration of the Influence of Current Injection on the Voltage Measurement

Appendix C.1. Formulation of the Problem

On an infinitesimally thick conductive plate with a width of w and a length of l at the position $\vec{x}_1 = (x_1, y_1)$, a current (I) is induced into the plate. At another position ($\vec{x}_2 = (x_2, y_2)$), a current of exactly the same strength flows out of the plane. In less abstract terms, this problem involves a metal plate with two needles pressed onto it, which function as contacts to an external ideal current source. Now, the task is to determine the potential field and the current density distribution inside the plate.

Appendix C.2. Governing Equations and the Infinite Plate Problem

Before considering a finite plate, the solution for an infinite plate is presented. Since the induced and extracted currents are constant, the problem can be assumed to be static, i.e., the electrical and magnetic fields (\vec{E} and \vec{B} , respectively) are independent of time ($\dot{E} = \dot{B} = 0$). In this case, the Maxwell equations describing the electric field (E) can be summarized by Poisson's equation

$$\Delta\Phi(\vec{x}) = -\frac{\rho(\vec{x})}{\epsilon}, \quad (\text{A1})$$

where Φ is the electric potential, $\rho(\vec{x})$ is the charge distribution, and ϵ is the permittivity inside the plate. The electric potential can be calculated once the charge density is known using this equation. Now, the charge density in this infinite plate problem is described.

It is generally accepted that a current flow does not result in a charge buildup inside a conductor. The conductor stays neutral. However, if an attempt is made to induce a fixed current through an infinitely small cross section into a plate, the charge density ($\vec{j}(\vec{x})$) is infinitely large. Under this condition, the charge neutrality is no longer valid. Therefore, only at positions (x_1, y_1) and (x_2, y_2) , where the current is being induced and respectively extracted, does the charge density not vanish. Instead, at these two positions, the charge

density is expressed by two parameters: Q_1 and Q_2 . By using two Dirac deltas, the charge density can be mathematically expressed as

$$\rho(\vec{x}) = Q_1\delta(\vec{x} - \vec{x}_1) + Q_2\delta(\vec{x} - \vec{x}_2). \tag{A2}$$

In order to find the as-yet-unknown parameters (Q_1 and Q_2), Ohm’s law is applied:

$$\vec{j} = \sigma\vec{E} \tag{A3}$$

where σ is the conductance of the plate. The integral of the current density around the source needs to be equal to the total current (I) that is being induced into the plate.

$$\begin{aligned} I &= \int_{\partial A} dA\vec{j} = \int_{\partial A} dA\sigma\vec{E} = \\ &= \int_A dV\sigma\nabla\vec{E} = \int_A dV\sigma\frac{\rho(\vec{x}_1)}{\epsilon} = \frac{Q_1\sigma}{\epsilon} \end{aligned} \tag{A4}$$

Gauss’s theorem was used to transform the surface integral to a volume integral. Since this is a 2D problem, the surface is a line, and the volume is an area in this case. The prefactor of the Dirac delta function can be obtained by applying a volume integral enclosing the root of the Dirac delta function, which is position (x_1, y_1) .

If the charge density of a single source, i.e., $\rho(\vec{x}) = \frac{\epsilon I}{\sigma}\delta(\vec{x} - \vec{x}_1)$, is plugged into (A1), the potential of a source on a plate can be computed:

$$\Phi_1(\vec{x}) = -\frac{I}{2\pi\sigma} \ln \sqrt{(\vec{x} - \vec{x}_1)^2} \tag{A5}$$

The potential of a sink, i.e., the point where the current (I) is being extracted, can be computed similarly, with the only difference being a minus sign in the constraint of (A1).

$$\Phi_2(\vec{x}) = \frac{I}{2\pi\sigma} \ln \sqrt{(\vec{x} - \vec{x}_2)^2} \tag{A6}$$

Since the Poisson equation is linear, the total potential of a sink/source system on an infinite plate can be simply determined by the superposition of Φ_1 and Φ_2 .

Appendix C.3. The Finite Plate Problem

In order to solve the finite plate problem, the linearity of Poisson’s equation is used again. Furthermore, because it is a solution for a certain charge distribution ($\rho(\vec{x})$) and a set of boundary conditions is unique, the boundary conditions are determined by the requirement that no current crosses through the boundaries of the plate, i.e.,

$$\vec{j} \cdot \vec{n} = 0, \tag{A7}$$

where \vec{n} represents the normal vectors at the plate boundaries. As long as the boundary conditions are satisfied, charges can be added outside the finite plate without affecting the solution inside the plate. This is true because of the uniqueness of the solution of the Poisson equation. It is also possible to place charges outside the plate in a manner that still fulfills the boundary conditions, as described in more detail by Griffiths [41].

If the plate with the sink and source were only constrained in one direction, such as $x > 0$, it would be sufficient to mirror the positions of the sink and source on the y axis. However, after introducing other boundary conditions, the source and sinks must also be mirrored on these new boundaries. This creates additional virtual sources and sinks that must be mirrored at the original boundary as well, leading to an infinite series of virtual sources and sinks, as shown in Figure A3.

According to [42], the coordinates of all sources or sinks that needed to express the finite plate problem for a source or sink at position (x_i, y_i) are given by

$$\begin{aligned} &(x_i + 2ml, y_i + 2nh), \\ &(2l(m + 1) - x_i, 2hn + y_i), \\ &(2l(m + 1) - x_i, 2h(n + 1) - y_i), \\ &(2lm + x_i, 2h(n + 1) - y_i) \end{aligned}$$

where $m, n \in \mathbb{Z}$. The variable m is needed to describe all mirror sources that are necessary to fulfill the boundary conditions of the current density in the x -direction, whereas the index n creates image sources to satisfy the constraints on the y component of \vec{j} .

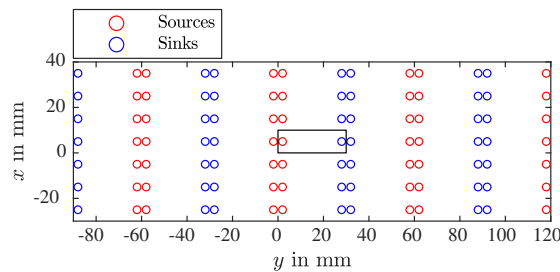


Figure A3. Mirror sources and sinks for an arbitrary position of the original source and sink.

The full potential of the source and sink problem is obtained by adding up the potentials related to sources and sinks at these coordinates.

$$\begin{aligned} \Phi_{\text{Source/Sink}}(\vec{x}) = & \mp \frac{I}{2\pi\sigma} \sum_{m=-\infty}^{\infty} \sum_{n=-\infty}^{\infty} \left\{ \ln \left| \begin{pmatrix} x_i + 2ml \\ y_i + 2nh \end{pmatrix} - \vec{x} \right| \right. \\ & + \ln \left| \begin{pmatrix} 2l(m + 1) - x_i \\ y_i + 2hn \end{pmatrix} - \vec{x} \right| \\ & + \ln \left| \begin{pmatrix} 2l(m + 1) - x_i \\ 2h(n + 1) - y_i \end{pmatrix} - \vec{x} \right| \\ & \left. + \ln \left| \begin{pmatrix} x_i + 2lm \\ 2h(n + 1) - y_i \end{pmatrix} - \vec{x} \right| \right\} \end{aligned} \tag{A8}$$

$$\implies \Phi_{\text{tot}}(\vec{x}) = \Phi_{\text{Source}}(\vec{x}) + \Phi_{\text{Sink}}(\vec{x}) \tag{A9}$$

The resulting potential field can be found in Figure A4. Figure A5 compares this analytical result with a numerical simulation. These numerical and analytical calculations align the most if, in the simulation, the radius of the current source, as well as the plate thickness, are set to be very small. Additionally, the mesh of the simulation was set to be extremely fine.

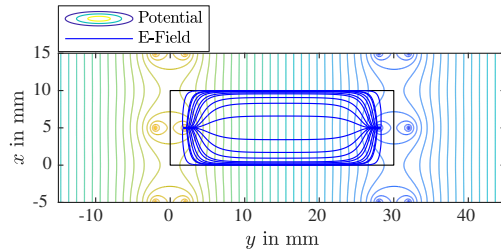


Figure A4. Potential distribution of the finite plate problem with a current of $I = 1$ and $\sigma = 156.64 \Omega^{-1}$ (effective 2D conductivity for a brass plate with a thickness of $d = 0.01$ mm).

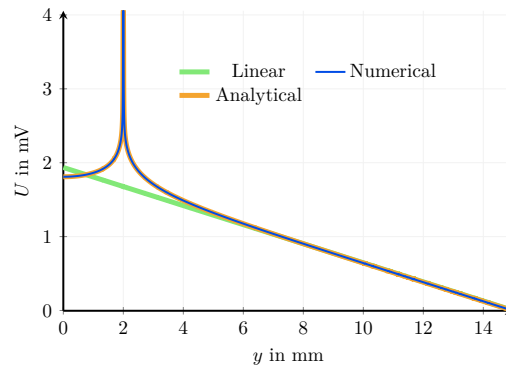


Figure A5. Potential across the y axis; a numerical and analytical voltage curve compared to the ideally expected linear slope of Ohm's law.

Appendix D. Resistance of An Adhesive Joining

Appendix D.1. Derivation of the Recursive Formula

Using the equivalent circuit depicted in Figure A6, the resistance of an adhesive joint can be calculated. In order to compute its total resistance for an arbitrary kP circuit (where k stands for the number of vertical resistors (r_c)), Δ -star transformations can be used to transform a kP into a $(k - 1)P$ circuit.

Figure A7 shows the circuit after a Δ -star transformation applied to the leftmost loop, where

$$s_a = \frac{r_a^{k-1}(r_c^k + r_b^{k-1})}{r_c^k + r_c^{k-1} + r_b^{k-1} + r_a^{k-1}} \tag{A10}$$

$$s_b = \frac{r_a^{k-1}r_c^{k-1}}{r_c^k + r_c^{k-1} + r_b^{k-1} + r_a^{k-1}} \tag{A11}$$

$$s_c = \frac{r_c^{k-1}(r_c^k + r_b^{k-1})}{r_c^k + r_c^{k-1} + r_b^{k-1} + r_a^{k-1}} \tag{A12}$$

This results in a $(k - 1)P$ circuit in series with the resistor (s_a), where the original resistor values of r_a^{k-1} and r_c^k were changed to $r_a^{k-1} + s_b$ and s_c , respectively. All other resistor values remain unchanged. Therefore, their indices (k) can be omitted.

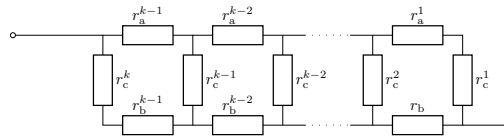


Figure A6. Equivalent circuit of a conducting adhesive joint

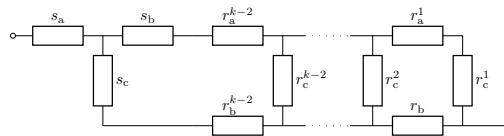


Figure A7. Equivalent circuit after a Δ-star transformation.

Now, a recursive formula for the total lap joint resistance (R_{LJ}^k) of a kP circuit can be found:

$$\begin{aligned}
 R_{LJ}^k(r_a^k, r_b^k, r_a, r_b, r_c) &= s_a + R_{LJ}^{k-1}(\tilde{r}_a^{k-2}, \tilde{r}_c^{k-1}, r_a, r_b, r_c) \\
 &\quad \text{with } \tilde{r}_a^{k-2} = r_a^{k-2} + s_b \text{ and } \tilde{r}_c^{k-1} = s_c \\
 &= \frac{r_a^k(r_b + r_c^k)}{r_a^k + r_b + r_c + r_c^k} \\
 &\quad + R_{LJ}^{k-1}(\tilde{r}_a^{k-1}, \tilde{r}_c^{k-1}, r_a, r_b, r_c) \\
 &\quad \text{with } \tilde{r}_a^{k-1} = r_a + \frac{r_a^k r_c}{r_a + r_b + r_c + r_c^k} \\
 &\quad \text{and } \tilde{r}_c^{k-1} = \frac{r_c(r_b + r_c^k)}{r_a + r_b + r_c + r_c^k}
 \end{aligned} \tag{A13}$$

Recursive reduction can be used until $k = 3$ is reached. Now, the 3P circuit shown in Figure A8 can be solved directly by a Δ-star transformation. The transformed circuit is depicted in Figure A9.

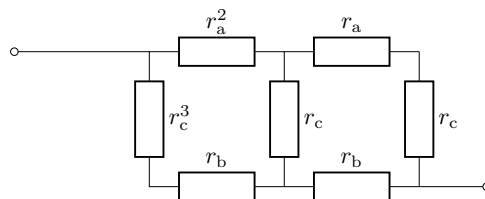


Figure A8. Base case for $k = 3$.

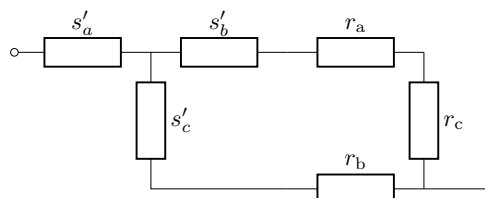


Figure A9. Base case for $k = 3$ after a Δ-star transformation.

The resistor values (S'_i) are expressed as

$$S'_a = \frac{r_a^2(r_c^3 + r_b)}{r_c^3 + r_c + r_b + r_a^2} \tag{A14}$$

$$S'_b = \frac{r_a^2 r_c}{r_c^3 + r_c + r_b + r_a^2} \tag{A15}$$

$$S'_c = \frac{r_c(r_c^3 + r_b)}{r_c^3 + r_c + r_b + r_a^2} \tag{A16}$$

and the total resistance of the 3P case is:

$$\begin{aligned} R_{LJ}^3(r_a^3, r_c^3, r_a, r_b, r_c) &= \\ &= S'_a + \frac{1}{\frac{1}{S'_c+r_b} + \frac{1}{S'_b+r_a+r_c}} \\ &= \frac{r_a^2(r_c^3 + r_b)}{r_c^3 + r_c + r_b + r_a^2} + \\ &\quad + \frac{1}{\frac{1}{\frac{r_c(r_c^3+r_b)}{r_c^3+r_c+r_b+r_a^2}+r_b} + \frac{1}{\frac{r_a^2 r_c}{r_c^3+r_c+r_b+r_a^2}+r_a+r_c}} \end{aligned} \tag{A17}$$

Appendix D.2. Convergence

In the equivalent circuit in Figure A6, r_a , r_b , and r_c are differential resistors that must be connected to a finite macroscopic resistor to ensure convergence. As k increases, these macroscopic resistors are decomposed into an increasing number of differential resistors. Quantitative dependencies can be found for the two limiting cases ($r_c \rightarrow \infty$ and $r_a, r_b \rightarrow 0$). Then:

$$r_A = \frac{R_A}{k-1} \tag{A18}$$

$$r_b = \frac{R_B}{k-1} \tag{A19}$$

$$r_c = kR_C \tag{A20}$$

After substituting these definitions into the recursive formula, $R_{LJ}^k(R_A, R_B, R_C)$ can be calculated for $k = 3, 4, 5$. The following expressions can be found for the symmetrical case where $R_A = R_B$:

$$\begin{aligned} R_{LJ}^3 &= \frac{(R_A)^2+12R_AR_C+18(R_C)^2}{2R_A+18R_C} \\ R_{LJ}^4 &= \frac{(R_A)^2+16R_AR_C+24(R_C)^2}{2R_A+24R_C} \\ R_{LJ}^5 &= \frac{(R_A)^3+55(R_A)^2R_C+700R_A(R_C)^2+1000(R_C)^3}{2((R_A)^2+50R_AR_C+500(R_C)^2)} \end{aligned} \tag{A21}$$

Figure 5b shows the dependence of the total resistance on the input parameters (R_A , R_B , and R_C) for the simplified symmetrical case with $R_A = R_B$. In Figure A10, the relative difference of a kP circuit compared to a 1000 P circuit is plotted.

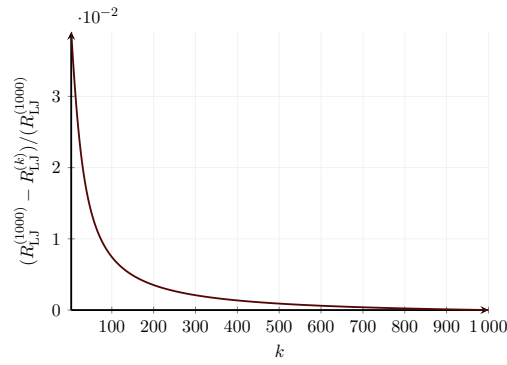


Figure A10. Error of the k -th step relative to the last computed step computed for $R_A^{\text{macro}} = R_B^{\text{macro}} = 1000 R_C^{\text{macro}}$.

Appendix E. Economical Evaluation

Table A1. Overview of the costs for the systems to apply electrically conductive adhesives (ECA) and laser beam welding for the joining of a 18650 battery cell.

Costs	Data	ECA	Laser Beam Welding
Machine			
(1)	Acquisition	EUR 50,000	EUR 453,000
(2)	Useful life	5 y	5 y
(3)	Working hours	3392 h/y	3392 h/y
(4)	Plant availability	90%	90%
Fixed			
(5)	Interest rate	1.14%	1.14%
(6)	Space requirement	10 m ²	10 m ²
(7)	Operating cost rate	550 euro/m ²	550 euro/m ²
(8)	Nominal power	10 kW	8 kW
(9)	Utilization rate	100%	100%
(10)	Electricity price	0.225/kWh	0.225/kWh
(11)	Maintenance cost rate	7%	7%
Variable			
(12)	Labor costs	39.73 euro/h	39.73 euro/h
(13)	Total cycle time	20 s/sample	1 s/sample
(14)	Adhesive	5.84 euro/g	0
(15)	Spacer	1.37 euro/g	0
(16)	Adhesive per sample	0.0045 g/sample	0
(17)	Spacer per sample	0.000025 g/sample	0

Table A2. Calculation of the machine costs per hour and the resulting costs per joint for ECA and laser beam welding for the joining of a 18650 battery cell

Costs	Formula	ECA	Laser Beam Welding
fixed	acc. Table A1		
(18) Depreciation	$\frac{(1)}{(2) \cdot (3)}$	2.95 euro/h	26.71 euro/h
(19) Interest cost per hour	$\frac{0.5 \cdot (1) \cdot (5)}{(3)}$	0.08 euro/h	0.76 euro/h
(20) Room cost per hour	$\frac{(6) \cdot (7)}{(3)}$	1.62 euro/h	1.62 euro/h
(21) Σ of fixed costs—machine hours	(18) + (19) + (20)	4.65 euro/h	29.09 euro/h
(22) Σ of fixed costs	(21) · (3)	15,785 euro/y	98,682.1 euro/y
variable			
(23) Energy	(8) · (10)	2.25 euro/h	1.80 euro/h
(24) Maintenance	$\frac{(1) \cdot (11)}{(2) \cdot (3)}$	0.21 euro/h	1.87 euro/h
(25) Labor	(12)	39.73 euro/h	39.73 euro/h
(26) Material	(14) · (16) + (15) · (17)	0.03 euro/sample	0 euro/sample
(27) Material	(26) · (3600) / (13)	4.77 euro/h	0 euro/h
(28) Σ of variable costs	(23) + (24) + (25) + (27)	46.96 euro/h	43.40 euro/h
(29) Σ of variable costs	$\frac{(13)}{3600} \cdot (28)$	0.26 euro/sample	0.01 euro/sample
(30) Max. number of samples per year	$\frac{(3)}{\frac{(13)}{3600} \cdot (4)}$	549.504 samples/y	10,990,080 samples/y

Table A3. Selection of joining areas for frequently used cell geometries.

Cell	Diameter or Lengths of Edges	90% Area	Adhesive Thickness	Adhesive Volume
	At the positive pole in cm	In cm	In μm	In cm^3
18650	0.8	0.4072	38	0.001547
21700	1	0.6362	38	0.002417
4680	1.5	1.431	38	0.005439
BEV2	1.8 · 3.6	5.832	38	0.02216

References

- Das, A.; Li, D.; Williams, D.; Greenwood, D. Joining Technologies for Automotive Battery Systems Manufacturing. *World Electr. Veh. J.* **2018**, *9*, 22. [\[CrossRef\]](#)
- Brand, M.J.; Schmidt, P.A.; Zaeh, M.F.; Jossen, A. Welding techniques for battery cells and resulting electrical contact resistances. *J. Energy Storage* **2015**, *1*, 7–14. [\[CrossRef\]](#)
- Brand, M.J.; Berg, P.; Kolp, E.I.; Bach, T.; Schmidt, P.; Jossen, A. Detachable electrical connection of battery cells by press contacts. *J. Energy Storage* **2016**, *8*, 69–77. [\[CrossRef\]](#)
- Brand, M.J.; Kolp, E.I.; Berg, P.; Bach, T.; Schmidt, P.; Jossen, A. Electrical resistances of soldered battery cell connections. *J. Energy Storage* **2017**, *12*, 45–54. [\[CrossRef\]](#)
- Reichel, A.; Sampaio, R.F.; Pragana, J.P.; Bragança, I.M.; Silva, C.M.; Martins, P.A. RForm-fit joining of hybrid busbars using a flexible tool demonstrator. *Proc. Inst. Mech. Eng. Part L J. Mater. Des. Appl.* **2022**, *236*, 1164–1175. [\[CrossRef\]](#)
- Bolsinger, C.; Zorn, M.; Birke, K.P. Electrical contact resistance measurements of clamped battery cell connectors for cylindrical 18650 battery cells. *J. Energy Storage* **2017**, *12*, 29–36. [\[CrossRef\]](#)
- Wassiliadis, N.; Ank, M.; Wildfeuer, L.; Kick, M.K.; Lienkamp, M. Experimental investigation of the influence of electrical contact resistance on lithium-ion battery testing for fast-charge applications. *Appl. Energy* **2021**, *295*, 117064. [\[CrossRef\]](#)
- Aradhana, R.; Mohanty, S.; Nayak, S.K. A review on epoxy-based electrically conductive adhesives. *Int. J. Adhes. Adhes.* **2020**, *99*, 102596. [\[CrossRef\]](#)
- Mostafavi, S.; Hesser, D.F.; Markert, B. Effect of process parameters on the interface temperature in ultrasonic aluminum wire bonding. *J. Manuf. Process.* **2018**, *36*, 104–114. [\[CrossRef\]](#)
- Kim, T.H.; Yum, J.; Hu, S.J.; Spicer, J.P.; Abell, J.A. Process robustness of single lap ultrasonic welding of thin, dissimilar materials. *CIRP Ann.* **2011**, *60*, 17–20. [\[CrossRef\]](#)
- Siddiq, A.; Ghassemieh, E. Thermomechanical analyses of ultrasonic welding process using thermal and acoustic softening effects. *Mech. Mater.* **2008**, *40*, 982–1000. [\[CrossRef\]](#)

12. Choi, S.; Fuhlbrigge, T.; Nidamarthi, S. Vibration analysis in robotic ultrasonic welding for battery assembly. In Proceedings of the 2012 IEEE International Conference on Automation Science and Engineering (CASE), Seoul, South Korea, 20–24 August 2012; pp. 550–554. [\[CrossRef\]](#)
13. Katayama, S. *Fundamentals and Details of Laser Welding*; Springer: Singapore, 2020. [\[CrossRef\]](#)
14. Kick, M.K.; Kuermeier, A.; Stadter, C.; Zaeh, M.F. Weld Seam Trajectory Planning Using Generative Adversarial Networks. In *Towards Sustainable Customization: Bridging Smart Products and Manufacturing Systems*; Lecture Notes in Mechanical Engineering; Andersen, A.L., Andersen, R., Brunoe, T.D., Larsen, M.S.S., Nielsen, K., Napoleone, A., Kjeldgaard, S., Eds.; Springer International Publishing: Cham, Switzerland, 2022; Volume 248, pp. 407–414. [\[CrossRef\]](#)
15. Grabmann, S.; Mayr, L.; Kick, M.K.; Zaeh, M.F. Enhancing laser-based contacting of aluminum current collector foils for the production of lithium-ion batteries using a nanosecond pulsed fiber laser. *Procedia CIRP* **2022**, *111*, 778–783. [\[CrossRef\]](#)
16. Grabmann, S.; Kick, M.K.; Geiger, C.; Harst, F.; Bachmann, A.; Zaeh, M.F. Toward the flexible production of large-format lithium-ion batteries using laser-based cell-internal contacting. *J. Laser Appl.* **2022**, *34*, 042017. [\[CrossRef\]](#)
17. Kick, M.K.; Habedank, J.B.; Heilmeier, J.; Zaeh, M.F. Contacting of 18650 lithium-ion batteries and copper bus bars using pulsed green laser radiation. *Procedia CIRP* **2020**, *94*, 577–581. [\[CrossRef\]](#)
18. Lee, S.S.; Kim, T.H.; Hu, S.J.; Cai, W.W.; Abell, J.A. Joining Technologies for Automotive Lithium-Ion Battery Manufacturing: A Review. In Proceedings of the ASME 2010 International Manufacturing Science and Engineering, Erie, PA, USA, 12–15 October 2010; Volume 1, pp. 541–549. [\[CrossRef\]](#)
19. Humpston, G.; Jacobson, D.M. *Principles of Soldering*; ASM International: Materials Park, OH, USA, 2004.
20. Schwartz, M. *Soldering: Understanding the Basics*; ASM International: Materials Park, OH, USA, 2004.
21. DIN Deutsches Institut für Normung e.V. *Adhesives—Terms and Definitions*; German version EN 923:2015 Beuth Verlag GmbH: Berlin, Germany, 2016. [\[CrossRef\]](#)
22. Holm, R. *Electric Contacts: Theory and Application*, 4th ed.; Springer: Berlin/Heidelberg, Germany, 1967. [\[CrossRef\]](#)
23. Li, Y.; Lu, D.; Wong, C.P. *Electrical Conductive Adhesives with Nanotechnologies*; Springer: Boston, MA, USA, 2010. [\[CrossRef\]](#)
24. Lu, D.; Wong, C.P. *Materials for Advanced Packaging*; Springer International Publishing: Cham, Switzerland, 2017. [\[CrossRef\]](#)
25. Li, Y.; Wong, C.P. Recent advances of conductive adhesives as a lead-free alternative in electronic packaging: Materials, processing, reliability and applications. *Mater. Sci. Eng. R Rep.* **2006**, *51*, 1–35. [\[CrossRef\]](#)
26. Gaynes, M.A.; Lewis, R.H.; Saraf, R.F.; Roldan, J.M. Evaluation of contact resistance for isotropic electrically conductive adhesives. *IEEE Trans. Compon. Packag. Manuf. Technol. Part B* **1995**, *18*, 299–304. [\[CrossRef\]](#)
27. Yim, M.J.; Li, Y.; Moon, K.S.; Paik, K.W.; Wong, C.P. Review of Recent Advances in Electrically Conductive Adhesive Materials and Technologies in Electronic Packaging. *J. Adhes. Sci. Technol.* **2008**, *22*, 1593–1630. [\[CrossRef\]](#)
28. Lee, J.; Cho, C.S.; Morris, J.E. Electrical and reliability properties of isotropic conductive adhesives on immersion silver printed-circuit boards. *Microsyst. Technol.* **2009**, *15*, 145–149. [\[CrossRef\]](#)
29. Maurer, A. Power-Module kleben statt löten. *Adhäsion Kleben Dichten* **2016**, *60*, 18–23. [\[CrossRef\]](#)
30. Sancaktar, E.; Bai, L. Electrically Conductive Epoxy Adhesives. *Polymers* **2011**, *3*, 427–466. [\[CrossRef\]](#)
31. Precht, A. *Vorlesungen über die Grundlagen der Elektrotechnik: Band 1*; Springer: Vienna, Austria, 1994. [\[CrossRef\]](#)
32. Love, A.E.H. *A Treatise on the Mathematical Theory of Elasticity*; Cambridge University Press: Cambridge, UK, 2013.
33. Toupin, R.A. Saint-Venant's Principle. *Arch. Ration. Mech. Anal.* **1965**, *18*, 83–96. [\[CrossRef\]](#)
34. Murrmann, H.; Widmann, D. Current crowding on metal contacts to planar devices. *IEEE Trans. Electron Devices* **1969**, *16*, 1022–1024. [\[CrossRef\]](#)
35. Berger, H.H. Models for contacts to planar devices. *Solid-State Electron.* **1972**, *15*, 145–158. [\[CrossRef\]](#)
36. Schmidt, P.A. Laserstrahlschweißen elektrischer Kontakte von Lithium-Ionen-Batterien in Elektro- und Hybridfahrzeugen. Ph.D. Thesis, Herbert Utz Verlag, München, Germany, 2015.
37. Lin, H.; Smith, S.; Stevenson, J.T.M.; Gundlach, A.M.; Dunare, C.C.; Walton, A.J. An evaluation of test structures for measuring the contact resistance of 3-D bonded interconnects. In Proceedings of the 2008 IEEE International Conference on Microelectronic Test Structures, Edinburgh, UK, 24–27 March 2008; pp. 123–127. [\[CrossRef\]](#)
38. Euler, J.; Nonnenmacher, W. Stromverteilung in porösen elektroden. *Electrochim. Acta* **1960**, *2*, 268–286. [\[CrossRef\]](#)
39. Habenicht, G. *Kleben—Erfolgreich und Fehlerfrei*; Springer Fachmedien Wiesbaden: Wiesbaden, Germany, 2016. [\[CrossRef\]](#)
40. Habenicht, G. *Kleben*; Springer: Berlin/Heidelberg, Germany, 2009. [\[CrossRef\]](#)
41. Griffiths, D.J. *Introduction to Electrodynamics*, 4th ed.; Cambridge University Press: Cambridge, UK; New York, NY, USA; Melbourne, Australia; New Delhi, India; Singapore, 2017.
42. Choi, Y.; Humphrey, J.A. Analytical prediction of two-dimensional potential flow due to fixed vortices in a rectangular domain. *J. Comput. Phys.* **1984**, *56*, 15–27. [\[CrossRef\]](#)

Disclaimer/Publisher's Note: The statements, opinions and data contained in all publications are solely those of the individual author(s) and contributor(s) and not of MDPI and/or the editor(s). MDPI and/or the editor(s) disclaim responsibility for any injury to people or property resulting from any ideas, methods, instructions or products referred to in the content.

4 A Novel Measurement Technique for Parallel-Connected Battery Cells

The previous chapter explained the measurement process of electrical joining techniques between cells. Different joining techniques were compared after determining an accurate and reproducible measurement process of electrical contact resistances. In the next step, cells are combined into parallel strings. In parallel strings, the current distribution is an option to quantify the inhomogeneity. Consequently, test-benches are necessary to define the driving forces for a homogeneous or an inhomogeneous current distribution.

In scientific studies, test-benches are designed to identify the factors influencing homogeneous current distribution under various boundary conditions. A precise and reproducible measurement setup is indispensable, which, up to now, was only possible with a high effort. Various current sensors are employed, ranging from contactless to contacting sensors. To our knowledge, no laboratory test-bench achieved clean re-contacting with defined additional path resistances.

This chapter presents the VPC, which virtually connects cells. Each cell is connected using the 4-wire measurement technique. The parallel connection is realized via the control variables of the battery cycler. Kirchhoff's node and loop law are used to solve the currents and voltages.

Due to Kirchhoff's node and loop law, additional resistances can be implemented in each parallel path. As the cells are only virtually connected in parallel through mathematical equations, it is possible to decouple the cells for check-up measurements and recouple them for cycling without ever having to touch them. In addition, cells can be easily located within different boundary conditions, such as positioning them in different climate chambers and varying the temperatures. → *Q4 How can the current distribution be measured efficiently in the presence of inhomogeneous contact resistances and path temperature?*

The novel measurement method was validated using a conventional test-bench in different charge, discharge, and rest phases. The results showed a good qualitative and quantitative agreement between the two measurement setups regarding the local minima and maxima and the intersection points of both currents.

Finally, two studies were conducted to assess the impact of contact resistances on the current distribution. The first study examined an additional resistance in one parallel path, while the second study focused on the influence of additional resistances in both parallel paths. Both studies concluded that the height of the local minima and maxima mainly depends on the resistance ratio relative to the combined cell and interconnection resistance in each pathway. However, neither the local minima and maxima observed at different cumulative charge throughputs nor the intersection points of the current distribution were affected by varying contact resistances. OCV interactions between both cells determine the shape of the current distribution. Additionally, the shape of the differential voltage showed correlations with the current distribution.

Authors Contribution

The study was designed and executed by Philipp Jocher with the support of Marco Steinhardt, Jonathan Martin and Sebastian Ludwig. The initial idea came from a discussion between Marco Steinhardt and Philipp Jocher. Philipp Jocher conducted the experiments and evaluated the experimental data. Philipp Jocher wrote the manuscript with the help of Markus Schindler. Andreas Jossen supervised the work. All authors discussed the data, commented on the results, and reviewed the manuscript.

A novel measurement technique for parallel-connected lithium-ion cells with controllable interconnection resistance

Jocher P., Steinhardt M., Ludwig S., Schindler M., Jonathan M. and Jossen A.

Journal of Power Sources 503 (2021) 230030

Permanent weblink:

<https://doi.org/10.1016/j.jpowsour.2021.230030>



Reproduced under the terms of the Creative Commons Attribution 4.0 License (CC BY-NC-ND, <http://creativecommons.org/licenses/by/4.0/>), which permits unrestricted reuse of the work in any medium, provided the original work is properly cited.



Contents lists available at [ScienceDirect](https://www.sciencedirect.com)

Journal of Power Sources

journal homepage: www.elsevier.com/locate/jpowsour



A novel measurement technique for parallel-connected lithium-ion cells with controllable interconnection resistance

P. Jocher^{a,*}, M. Steinhardt^a, S. Ludwig^a, M. Schindler^a, J. Martin^b, A. Jossen^a

^a Technical University of Munich (TUM), Institute for Electrical Energy Storage Technology (EES), Arcisstr. 21, 80333 Munich, Germany

^b BaSyTec GmbH, Öllinger Weg 17, 89176 Asselfingen, Germany

ARTICLE INFO

Keywords:

Current distribution
Virtual parallel connection
Resistance variation
Lithium-ion battery cell
Battery system

ABSTRACT

Due to the broad use of parallel-connected cells across multiple applications, it is essential to understand the current distribution between them. Variations in resistance, temperature and capacity can lead to an inhomogeneous current distribution and have a deleterious influence on ageing and safety. It is therefore crucial to investigate the current distribution within such systems. However, the task of designing a low-complexity test apparatus, that does not itself affect the current measurement, remains incomplete.

This work investigates a novel measurement method to connect cells in parallel with controllable interconnection resistances. Instead of a physical connection, the presented method couples the cell using Kirchhoff's laws via a commercial battery cycler. This connection allows investigation of parallel-connected cells, without influencing factors such as contact resistances or an additional measurement environment.

Further, two studies demonstrate the influence of the additional interconnection resistance caused by the parallel connection of two cells. The results of measurements including a differential voltage analysis show, that the cell current divides according to the ratio of the combined cell and interconnection resistance, whilst the open-circuit-voltage influences the shape of the current distribution.

1. Introduction

Lithium-Ion Batteries (LIBs) are used in many different applications and have to fulfil varying power and energy requirements [1]; from consumer electronics, with low energy and power requirements, up to automotive applications, e.g. Audi e-tron, Nissan Leaf, Renault ZOE and Tesla Model 3, to stationary operations where high power and energy are required, series and parallel connections can be used to achieve the desired characteristics [2]. Coupling cells in series raises the voltage of the battery module, although maximum voltage of the battery module is limited by the need for electrical isolation and the cost of semiconductors [3]. Connecting cells in parallel is used to achieve a desired energy. The load of each parallel path is defined by the resistance of the electrical wiring and junction to the cell, the open-circuit-voltage (OCV), the capacity and the internal resistance of the cell.

As such, variations during production, ageing and temperature differences and their effects on the OCV, capacity and the internal resistance can induce inhomogeneous current distribution [4–7]. It is therefore crucial to understand the drivers of the current distribution. With help of test-benches, the measurement of the current through each path in parallel-connected cells, helps to determine the driving

forces for convergence and divergence of the current distribution. The typical test-bench challenge is to define and minimise the influencing factors caused by the current measurement. The aim is an accurate and reproducible measurement of the individual cell current. Although we are aware that in commercial settings it can be rather difficult to test, verify, and ensure uniform current distribution in individual paths to another, the researcher goal is understanding the current distribution of parallel connected cells and the development of improved guidelines for commercial applications. Alternative approaches to the problem of battery diagnostics can be found in the work of Wei et al. [8] which discussed a variety of smart battery sensors, containing also innovative current sensors.

To understand the behaviour of parallel-connected cells, many researchers [4–7,9–26] have designed distinct test-benches to measure the current distribution. In any test-bench defined and undefined resistances caused by wiring, interconnections and measurement equipment can adversely effect the current distribution.

A summary of the publications regarding the measurement of the current distribution is presented in Table 1. All test-benches were designed such that measurement equipment and contact areas would

* Corresponding author.

E-mail address: philipp.jocher@tum.de (P. Jocher).

<https://doi.org/10.1016/j.jpowsour.2021.230030>

Received 10 February 2021; Received in revised form 15 April 2021; Accepted 9 May 2021

Available online 24 May 2021

0378-7753/© 2021 The Author(s).

Published by Elsevier B.V. This is an open access article under the CC BY-NC-ND license

(<http://creativecommons.org/licenses/by-nc-nd/4.0/>).

minimally influence the measured current. For the conventional measurement of the current on each parallel path, contactless, e.g. hall- and fluxgate sensors, as well as contacting sensors, e.g. shunt resistance, were used. Increasing the resistance in parallel paths leads to a more homogeneous current distribution [4,5,12], but the efficiency decreases due to increased ohmic losses. On the other hand, an inhomogeneous resistance ratio between parallel-connected paths leads to a divergent current distribution between parallel conduction paths [4,5,12].

Some of the authors quantified the influence of their interconnection technique, whereas others did not. To better understand their influence upon measurements, values and standard deviation intervals of the resistance of several interconnection techniques can be found in [27–30].

In the studies focussing on the measurement of the current distribution, the researchers investigated at most two parallel (2p) parallel-connected round cells with Lithium Sulphur (LS) and different LIBs cathode materials such as Lithium Iron Phosphate (LFP), Nickel Manganese Cobalt (NMC), Nickel Cobalt Aluminium (NCA) and Lithium Cobalt Oxide (LCO). Additionally, the resistance of the measurement environment is listed in the table, if it was defined in the work. Otherwise not defined (n.d.) is written. The primary goal was to determine the ageing behaviour of parallel-connected cells. Several measurement studies investigated the influence of parameter variations on the current distribution, using real capacity and ohmic resistance differences between the cells [4,5,10,12]. Additionally, measurements provided in [12] show the influence of cable resistances on current distribution.

Brand et al. [4] attempted to construct a defined measurement set-up with low impedances. For the measurement of the current distribution between 2p-connected battery cells the test-bench consisted of six current sensors. Fluxgate- and hall-transducer were used without increasing resistance in any parallel pathways. All in all, Brand et al. were able to determine an additional ohmic resistance of less than 1.5 mΩ per path. Combining test-bench results and simulations, Brand et al. showed, that at the beginning of a current step, the current distribution is dominated by resistances. In contrast, capacity differences affect the current distribution in the long term. Fill et al. [12] described a measurement set-up with adjustable thermal control of cells connected in parallel with an additional resistance of 0.3 mΩ per path and investigated the impact of the resistances on the current distribution within the whole measurement set-up. In this set-up load cables were used as a shunt resistance. Further, they used the measurement set-up to validate a simulation model showing the effects of module design on temperature gradients. Within a subsequent publication, Fill et al. [5] discussed the influence of current distribution, of cell parameter differences and of dynamic current stresses. Hofmann et al. [6] described a measurement set-up, using a shunt current sensor with a resistance of 1.0 mΩ. The test set-up consisted of a copper clamping construction, where cells are connected in parallel using laser welded hilumin plates. The test-bench was used to validate a simulation model for both, CC and dynamic load profiles.

Even though all of the publications in Table 1 produced useable findings, they have a common shortcoming: their measurement set-up influenced the current distribution. Some of the authors described their attempts, at great effort and cost, to determine and reduce each additional parasitic resistance, whereas others do not consider them. As a faulty contact or an unclean test-bench can unbalance the resistance ratio between parallel pathways, whilst the internal resistance of commercial LIBs is in the range of few mΩ, a clean test-bench is indispensable for high-quality experiments.

This work describes a novel measurement technique to connect cells in parallel, that overcomes the problems of additional and undefined resistances due to measurement equipment and contact resistance. Whereas in conventional test-benches cells are connected physically with junctions, Fig. 1(a), this novel technique takes advantage of Kirchhoff's laws, calculating the resulting voltage or current, and connects

Table 1

Publications regarding current distribution with details on the measurement equipment, the path resistance and the number and chemistry of cells in parallel.

Ref.	Measurement set-up	Number of cells in parallel	Cell format & chemistry	Additional resistance in mΩ per path
[9]	Hall Effect current sensor, undefined wiring	2	18650 - nickel-based	n.d.
[31]	n.d.	2	18650 - NCA	n.d.
[4]	Shunt resistance, Fluxgate and Hall Effect current sensor	2	18650 - NMC	1.5
[10, 21]	Shunt resistance, undefined wiring	4	18650 - n.d.	10
[11]	Hall Effect current sensor	2 & 3	18650 - NMC	n.d.
[5,12]	Load cables were used as a shunt	2	Pouch - LCO	0.3
[13]	Shunt resistance	3	Round - LFP	2.15
[14]	Sensors and wiring undefined	2	Round - LFP	n.d.
[15]	Hall Effect current sensor	2, 3 & 4	Pouch - n.d.	n.d.
[16]	Load cables were used as a shunt	4 & 8	26650 - LFP & 18650 - LCO	3
[6]	Shunt resistance	2	18650 - NMC	1
[17]	Shunt resistance	3	Pouch - LS	20
[18]	Shunt resistance	27	18650 - NMC	25
[7]	Shunt resistance and wiring undefined	5	18650 - LFP & NMC	3.4
[19]	Shunt resistance, undefined wiring	2 & 4	18650 - n.d.	5
[20]	Shunt resistance, undefined wiring	2	Pouch - NMC	5
[22, 25]	Contactless sensor, undefined wiring	8	18650 - n.d.	n.d.
[32]	n.d.	3	Pouch - NCA/LCO	n.d.
[23]	Shunt resistance	2	n.d. - LFP	0.25
[24]	Shunt resistance	Multi tab	Pouch - LFP	2
[26]	Hall Effect current sensor	5	Pouch - LFP	n.d.

cells in parallel using a commercial battery cycler, Fig. 1(b) and (c). Therefore, each cell benefits from the 4-wire measurement of the battery cycler, which generates no additional interconnection resistances. For this reason, only the OCV, the capacity and the resistance of the cell itself, as well as its relationship to other cells can influence the current distribution. Each cell is individually connected to the battery cycler using a 4-wire connection, and each cell voltage can be controlled separately. A current pulse is used to determine the voltage across the reference cell and the control unit imposes the same voltage across each cell. Thus, although individually connected to separate voltage sources, a 'virtual parallel connection' is present.

Connecting cells virtually has many advantages, such as coupling and decoupling without touching the cells, scaling to n-parallel constellations, low assembly effort on the test-bench and defined contact resistances. In addition, different cell formats can be investigated with no additional effort.

In this paper, the novel measurement method will first be validated and discussed for CC-, CV- and rest phases using of a conventional test-bench. Next, two studies will show the effect of additional resistances on the measurement. The first study investigates the influence of an inhomogeneous resistance increase within one leg of the parallel paths. Subsequently, the second study examines a homogeneous impedance increase within both parallel-connected paths. Finally, a DVA is used to discuss the relationship between the current distribution and the OCV.

2. Experimental

2.1. Cell characteristics

All measurements are performed in a climate chamber (Espec LU-123) at 25 °C with a commercial high energy 3.35 Ah cell

Table 2
 Measured capacity and ohmic resistance of the investigated cells in a climate chamber at 25 °C.

Cell	CCCV capacity in Ah	Ohmic resistance in mΩ at 50% SoC
cell 1	3.288	29.626
cell 2	3.296	32.536
cell 3	3.315	28.413
cell 4	3.344	28.525

(LG INR18650-MJ1). The electrodes are composed of nickel-rich NMC (811) on the cathode and silicon doped graphite (SiC) on the anode side [33,34]. The measurements in this work, unless not otherwise stated, were carried out by a CTS 32 channel battery cycler from BaSyTec GmbH where every cell is connected individually to a channel. According to the data-sheet of the battery cycler used in this work, the voltage sensor is guaranteed to a precision of 1 mV and a resolution of 0.3 mV and the current sensor to a precision of 1 mA and a resolution of 0.250 mA at the voltage and current ranges, used in this work CC periods. At the lower currents used for the DVA and the resting periods, the current measurement exhibits precision and sensitivity values that are correspondingly smaller.

All cells used within this study were initially characterised to determine their capacities and ohmic resistances. The capacity was measured via a constant current constant voltage (CCCV) charge with a CC rate of 0.2 C and a cut off current of 50 mA at 4.2 V. Ohmic impedance was determined at 50% State of Charge (SoC) using galvanostatic electrochemical impedance spectroscopy (EIS) with a current amplitude of 140 mA on a VMP3 potentiostat from Biologic Science Instruments SAS and was measured as the real-axis intercept of the Nyquist plot.

The cell type used in this work is known to contain variances in capacity and resistance [35–37]. Therefore, for the validation of the virtual parallel connection two cells with resistance spread of 2.9 mΩ and a capacity difference of 8 mAh, cell 1 and cell 2 from Table 2 were used. According to recently published results by Schindler et al. [37], the difference in resistance appears relatively high, which it corresponds to a difference of almost ten times the standard deviation for cells from the respective production batch. On the other hand, the difference in capacity corresponds to only 0.5 times the standard deviation [37].

For the measurements investigating the behaviour of cells with low initial differences in capacity and internal resistance cell 3 and cell 4 (see Table 2) were chosen.

2.2. Measurement principle

Any n -parallel connection can be typified by a simple ECM. Fig. 1(a) represents a simple ECM of a conventional n -parallel connection using a battery cycler in CC mode with as current source and voltage measurement within a 4-wire connection. Within such an ECM, each conduction path $x \in [1, n]$ consists of a cell x , that represents an individual cell including internal resistance and OCV, and a contact resistance, $R_{c,x}$, that stands for any additional resistance caused by contacting, wiring and measurement equipment. Using Kirchhoff's voltage and current laws, the following equations can be defined:

The current, I_x , of path x can be determined by the difference between the total current of the system, I_{tot} , and the sum of the current through all other n parallel paths, according to the Kirchhoff node law, Eq. (1).

$$I_x = I_{tot} - \sum_{y \in [1, n], y \neq x}^n I_y \quad (1)$$

Analogously, the voltage across the parallel connection, U_p , can be determined by employing the Kirchhoff loop law, represented by m_1 on Fig. 1(a). This generates Eq. (2).

$$U_p = U_{cell,y} + I_y \cdot R_{c,y} = U_{cell,x} + I_x \cdot R_{c,x} \quad (2)$$

Based on Eq. (2), the voltage of the cell x in path x , $U_{cell,x}$, as a function of cell y , can be determined with Eq. (3).

$$U_{cell,x} = U_{cell,y} + I_y \cdot R_{c,y} - I_x \cdot R_{c,x} \quad (3)$$

If all cells are operated by independent battery test channels, and assuming that each channel can read the values of voltage and current from others and use this as a control parameter, it is possible to set up the virtual parallel connection. This is achieved by utilising Eqs. (1) and (3). An example of this is provided in Fig. 1(c) where cell 1 is operated by a current source in respect to Eq. (1) – current I_1 is then used as the setpoint and voltage $U_{cell,1}$ is the feedback parameter that is fed to the control unit. All other $n-1$ cells are operated by a voltage source corresponding to Eq. (3) and as such, voltage $U_{cell,n}$ is the setpoint and current I_n is the feedback parameter. This means that each cell is operated at the same voltage, as though the cells were in parallel. Further, no undefined contact resistances occur due to the 4-wire connection of each channel. If an additional resistance is desired, the virtual parallel connection can increase the interconnection resistance, $R_{c,x}$, by calculating an ohmic loss in respect to Eq. (3).

The resulting closed-loop control system of n -parallel-connected cells is shown in Fig. 1(b). The forward path corresponds to the path through cell 1 with the additional resistance $R_{c,1}$. Further, the feedback path corresponds to the path through cell 2 with the resistance $R_{c,2}$. The setpoint of the forward-path is the current I_1 and the voltage sensor measures the cell response of cell 1. Combining the calculated voltage drop over the resistance $R_{c,1}$ with the calculated current through path 1, the voltage of the virtual parallel connection, U_p , results. The feedback path of cell 2, controlled by voltage $U_{cell,2}$ results in the current I_2 . This current I_2 is used to calculate the voltage drop over the resistance $R_{c,2}$. Any additional parallel path of n cells is calculated in the same manner as the feedback path of cell 2.

Consequently, for a 2p connection, the above defined equations were summarised to two equations. The voltage of cell 2 is controlled as in Eq. (3) and the current of cell 1 is controlled as in Eq. (1). According to Brand et al. [4] an asymmetric resistance ratio influences the beginning of a current pulse in the manner of a typical current divider. The current divider for the 2p connection of this work is given by Eq. (4), based on the ECM on Fig. 1(a).

$$i_2/i_{tot} = \frac{R_{cell,1} + R_{c,1}}{R_{cell,1} + R_{c,1} + R_{cell,2} + R_{c,2}} \quad (4)$$

2.3. Validation of the measurement

The virtual parallel connection described above is validated by a conventional 2p test-bench. This test-bench was designed and validated by Hofmann et al. [6,38]. To allow a better understanding of this work, a short summary is given.

The conventional test-bench of Hofmann et al. is shown in Fig. 2. It consists of a shunt current transducer ① with a resistance of 1.0 mΩ and a temperature coefficient of 30 ppm K⁻¹. Each cell ② is mounted with laser-welded hilumin plates ③ and fixed into the copper clamps ④. Soldered junctions and wiring ⑤ are used to connect the shunt resistance ① with the copper clamp ④ and the main connector ⑥. A 24-bit analog digital converter (ADC) measurement board ⑦ is used to measure the current. The current is applied to the main connector ⑧.

A temperature control unit is also integrated into the test-bench but not used and not mounted in this work. Consequently, the cells in this work are connected without cooler ⑨, Peltier element ⑩ and copper shells ⑪.

For the measurement using the virtual parallel connection, the cells are removed from the conventional test-bench and connected by the individual cell connector ⑫ to an independent channel of the battery cycler. With the 4-wire measurement at the hilumin plate, the

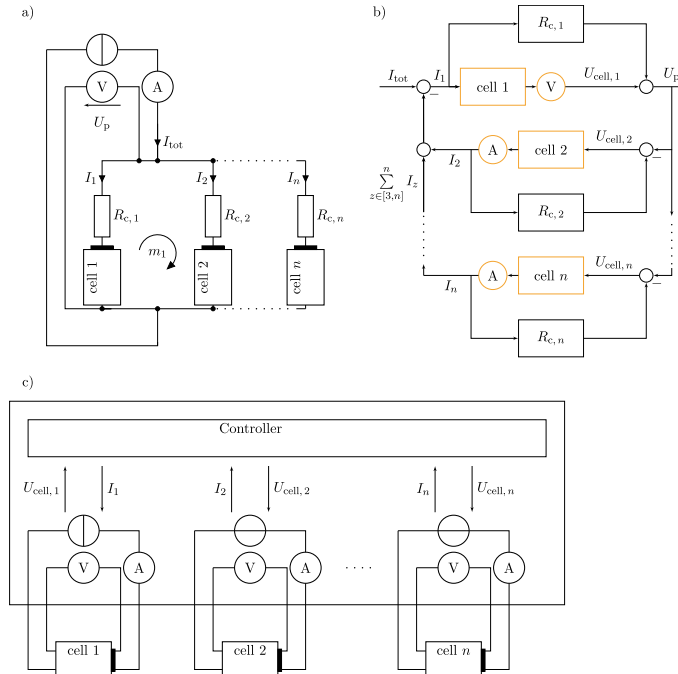


Fig. 1. (a) Simple ECM of a conventional n-parallel connection using a battery cycler in CC mode – current source and voltage measurement – in which each cell represents both the cell and its internal resistance, and a contact resistance, R_c that stands for any additional potential drop due to contacting, wiring and measurement equipment. (b) Closed-loop control system of a virtual n-parallel connection. The forward-path corresponds to the cell 1 with the additional resistance $R_{c,1}$ and the feedback-path is equivalent to the cell 2 (cell n) with the additional resistance $R_{c,2}$ ($R_{c,n}$). All symbols with an orange border refer to physical components. (c) Schematic of the virtual parallel connection within a n -channel battery cycler and physical cells connected to individuals channels via 4-wire technique. The controller calculates the setpoint of any channel with regard to Eqs. (1) and (3). Cell 1 is fed by a current source, see Eq. (1); current I_1 is the setpoint and voltage $U_{cell,1}$ is the feedback parameter. All other $n-1$ cells are operated with a voltage source, see Eq. (3). Voltage $U_{cell,n}$ is the setpoint and current I_n is the feedback parameter. (For interpretation of the references to colour in this figure legend, the reader is referred to the web version of this article.)

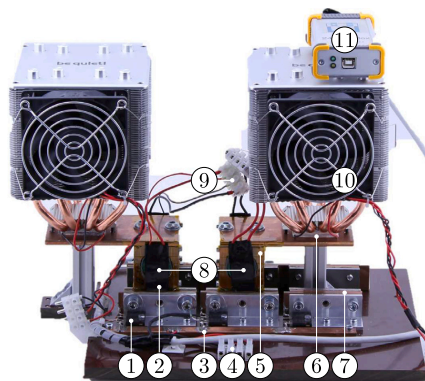


Fig. 2. Conventional test-bench used for the validation of the virtual measurement method; picture taken from [38]. Shunt ①, hilumin plate ②, soldered connection and wiring ③, main 2p connector ④, copper shells - not used in this work ⑤, peltier element - not used in this work ⑥, copper clamp ⑦, cells ⑧, individual cell connector ⑨, cooler - not used in this work ⑩, measurement board ⑪.

resistance of the laser-welded spots from the cell pole to the hilumin plate can be neglected. The measured capacity and ohmic resistance of these cells, as described in Table 2, had been established using this connection.

To ensure that both measurement methods incorporate the same additional resistance of the test-bench, $R_{c,x}$ has to be included in the virtual parallel connection. To define the resistance influence of the conventional test-bench, a hilumin strip was clamped between the two copper clamps, ⑦ on Fig. 2, instead of a physical cell.

Using this measurement set-up, an additional resistance of 2.2 mΩ for each path was determined using a high precision resistance measurement unit from Li.plus GmbH. The additional resistance results from the shunt of 1 mΩ ①, the press contact and the soldered connections as well as the wiring ③ between the main connector ④ and the clamping construction ⑦. Considering the results given in [28], the resistance of a press contact area of 10 mm × 15 mm with brass as the contacting material results in a resistance of about 0.15 mΩ. The remaining resistance of 0.9 mΩ is caused by additional undefined resistances due to soldered connections and wiring. Additional undefined resistances due to the area in the clamp and the welding area may occur.

3. Results and discussion

3.1. Validation of the measurement setup

For the validation of the virtual parallel connection, two test scenarios were chosen. The first test scenario was a CCCV charge and discharge, each at 1 C, and a cut-off current of 100 mA. The second test scenario was a CC charge and discharge at 1 C and a consecutive rest phase of 3600 s after each of the CC phases. The currents are related to the system current, and we would expect that the nominal current per cell should be half of the system current. Both scenarios were repeated over four cycles.

If one aims to compare different measurement methods with each other, it has to be ensured that the current distribution is reproducible and does not change significantly between two consecutive cycles. To calculate the difference between two cycles, x_1 and x_2 , the root mean square (RMS) value x_{RMS} can be calculated by Eq. (5) and the maximum difference by Eq. (6). Here, i defines the time-discrete point.

$$x_{RMS} = \sqrt{\frac{1}{n} \sum_{i=1}^n (x_1(i) - x_2(i))^2} \tag{5}$$

$$x_{max} = \max_{i=1, \dots, n} |x_1(i) - x_2(i)| \tag{6}$$

The differences between two consecutive cycles of virtual parallel connection were calculated to be $i_{RMS} = 0.487$ mA with a maximum value of $i_{max} = 2.386$ mA, whereas the conventional test-bench resulted in an $i_{RMS} = 0.438$ mA and a maximum difference of $i_{max} = 3.402$ mA. Taking the mean current of 1.675 A into account, these differences correspond to maximum deviation of 0.03 % and 0.2 %. For the purposes of comparing the measurement methods, these deviations are deemed to be negligible.

Further, the standard deviation of the sum of both currents over a CC phase is a quality factor of the test-bench and the battery cyler. The noise of the virtual measurement was found to 0.52 mA.

To compare and contrast the two measurement methods, six different phases of a typical LIBs charge–discharge cycle, including CC, CV and resting, were analysed. As described above, an additional resistance of $R_{c,s} = 2.2$ mΩ was added to each leg of the virtual connection to ensure comparability. Figs. 3 and 4 show the current distribution of both measurement methods over their charge and discharge phases. The orange lines represent the test-bench measurements with a physical interconnection and are labelled with “physical”, whereas the blue lines show the measurements with the virtual parallel connection and are therefore labelled with “virtual”. The solid lines correspond to the current through path 1 and the dashed lines to the current of path 2. The black, dashed line on the subfigure (a) represents the case of a homogeneous current distribution. The C-rate of the y-axis is calculated relative to the nominal capacity of a single cell.

Fig. 3 illustrates the charging behaviour of both methods. The subfigures represent the CC charging phase (a), the CV charging phase (b) and the resting phase (c) for both measurement techniques. For all measurements high qualitative and quantitative compliance is seen. Since both approaches display a high degree of similarity, the virtual rate closely follows the physical test-bench rate.

The lines representing the relative distribution of the charge produced by both methods agree closely. This is shown by the locations of their local minima and maxima and the intersection with the line drawn at 0.5 C. The same cumulative charge per cell is measured by both methods. This result is underlined by an RMS of less than 1.9 mA (0.11 %) for both, CC and CV charging between both measurement methods. Fig. 3(c) illustrates the resting phase after a CC charging.

Fig. 4 shows the discharge behaviour of the two cells connected in parallel. The CC and CV phases are marked with the letters (a) and (b) respectively. As seen in the charging behaviour, the local minima

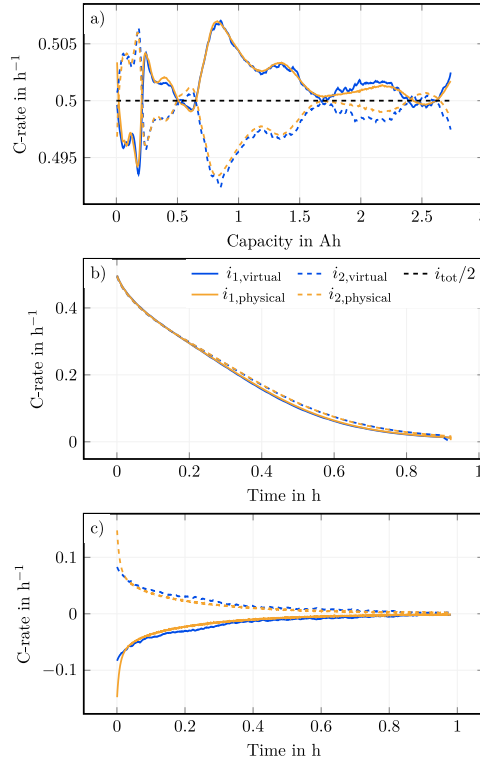


Fig. 3. Validation of the current distribution during charge between the novel measurement method and a conventional test-bench [38]. (a) shows the CC charge with an current of $I_{cc} = 1$ C and (b) shows the consecutive CV charge to 4.2 V. (c) shows the rest phase after a CC charge. (For interpretation of the references to colour in this figure legend, the reader is referred to the web version of this article.)

and maxima and the intersections of both currents display the same cumulative discharge throughput per path during discharge. Fig. 4(c) represents the rest phase after the CC discharge, where the highest difference occurs during the beginning of the phase. This might be explained as a consequence of the divergent current distribution at the end of the previous phase. Fig. 4(b) and (c) show the greatest differences between both measurement methods with disparities of 138.2 mA for the CV phase and 157.6 mA for the rest phase. Both follow the CC discharge phase, and the highest difference of 72.14 mA occurs during CC discharging at low SoC around 3.2 Ah. It seems that the virtually connected cells are exposed to a slightly higher voltage range, and therefore the current shows higher spreads at the end of the CC discharge phase. Most likely, this is caused by an additional resistance in the virtual test-bench due to an undefined resistance in the clamp contacts of the construction. The influence of such additional resistances is presented later on to underpin the importance of a correctly defined resistance in the measurement set-up. Nevertheless, an RMS of less than 7.5 mA (0.45 %) for both CC and CV discharging can be determined. Table 3 summarises all differences between RMS and maximum current for both test scenarios.

All in all, the comparison of the two measurement methods shows good correspondence between the local minima and maxima of both

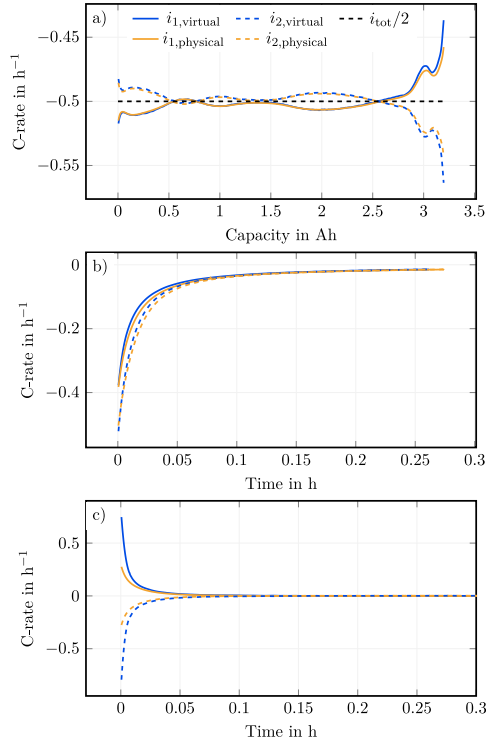


Fig. 4. Validation of the current distribution during discharge between the novel measurement method and a conventional test-bench [38]. (a) shows the CC discharge with an current of $i_{\max} = 1$ C and (b) shows the consecutive CV discharge to 2.5 V. (c) shows the rest after a CC discharge. (For interpretation of the references to colour in this figure legend, the reader is referred to the web version of this article.)

Table 3
Differences between i_{RMS} and i_{\max} in the conventional- and the virtual measurement method in different phases, according to Figs. 3 and 4.

	Fig. 3 - Charge			Fig. 4 - Discharge		
	CC (a)	CV (b)	Rest (c)	CC (a)	CV (b)	Rest (c)
i_{RMS} in mA	1.485	1.838	1.912	7.054	6.444	7.411
i_{\max} in mA	14.71	19.76	21.61	72.14	138.2	157.6

measurement methods as well as the intersection points of both currents during CC charging and discharging demonstrating points where the uneven current distribution through the cells was reversed. With these findings, the virtual connection can be used as a measurement method to connect cells in parallel. The presented measurement method should be open to all measurement devices which are capable of dynamic interaction between their channels.

Researchers investigating the ageing of parallel-connected LIBs have reported differing results in regard to the convergence and divergence of the current distribution. Although some discovered convergent current distribution behaviours [10,21], others found the opposite [15,39–42].

Any ageing study of LIBs is complex. Due to the influence of parameter variations, environmental parameters and load profiles on the

ageing behaviour [43], a large number of tests are necessary to reach a scientific conclusion [44]. With individual cell connections each cell is connected via the 4-wire technique, therefore no additional resistance occurs and this is increasing the accuracy of the measurement.

Conversely, the interconnection of the cells in a conventional parallel test bench as well as the measurement of the current can introduce additional resistances that can influence the current distribution [12, 28,31]. Added to the extra time and effort required to set such test benches up, the virtual parallel measurement represents a quicker and easier method to measure the same quantities. It is also not subject to the distorting effects of the additional resistances. To define possible influences of system parameters two studies are carried out.

3.2. Influence of system parameters

Due to the nature of electrical connection, additional resistances are inevitable in physical applications. In any conventional test-bench, the contact, wiring and measurement resistances increase the influence of the test-bench on the measurement. As described in Section 1, these additional interconnection resistances influence the current distribution and should therefore be minimised. Thus, in the following section, the influence of varying interconnection resistances within the measurement set-up on the current distribution is investigated. The intention is a better understanding of the drivers of inhomogeneous current distribution during measurements with exact additional resistance.

This study addresses the influence of undefined resistances, e.g. due to production variance of the electrical connectors, as well as defined resistances in test-benches, e.g. measurement equipment. The values were chosen with respect to typical additional resistances of conventional test-benches as summarised in Table 1, as well as faulty contact resistances. Hence, the resistance $R_{c,x}$ is set to 0 m Ω , 0.2 m Ω , 0.5 m Ω , 1 m Ω , 2 m Ω and 5 m Ω and measurements were conducted using cell 3 and cell 4, which are described in Table 2. Two 2p studies with additional interconnection resistances are examined by increasing of R_c . Study one analyses an increase of $R_{c,2}$, where $R_{c,1}$ is set to 0 m Ω . Study two investigates an increase of the resistance on both paths, such that $R_{c,1} = R_{c,2}$. For both studies the x-axis represents time and not the charge throughput as used in Figs. 3 and 4. This allows a better comparison of the curves due to the inhomogeneous resistance ratio.

Fig. 5 shows CC charging and discharging in the presence of an asymmetric resistance ratio with a homogeneous current through each path of $i_{1/2} = 0.5$ C. As expected from Eq. (4), the degree of distribution of the current is determined by the path resistance. This is however not responsible for the alterations in this distribution over time, which remain independent of path resistance. At the marked time intervals, the same maxima and minima are seen for all measurements. A quantitative analysis of the current at different local minima and maxima is illustrated in Fig. 7. The height change in the minima and maxima marked from ① to ⑥ in Fig. 5 corresponds to the ratio of the respective path resistances.

The higher current gap observed for marker ① during discharging can be explained by the SoC dependency of the internal resistance, as noted generally by [45,46] and by Zilberman et al. [47] for this cell type. The resistance is minimal at medium SoC range and increases for both higher and lower SoC. Its maximum values are found at low SoC. This can also be seen in the gradient of marker ① in the current in Fig. 7(a). The higher the internal resistance of both cells, the flatter the resultant gradient, see Eq. (4). Further, the steepness of the OCV influences this phenomenon [6]. Consequently, variations in resistance dominate the current distribution for flatter OCVs, whereas OCV changes become more influential as they become steeper. Therefore it can be stated, that the height of the minima and maxima of the current distribution are mainly dependent on the resistance ratio. In contrast, neither local minima and maxima seen at given cumulative charge throughputs, nor the changes in current distribution between

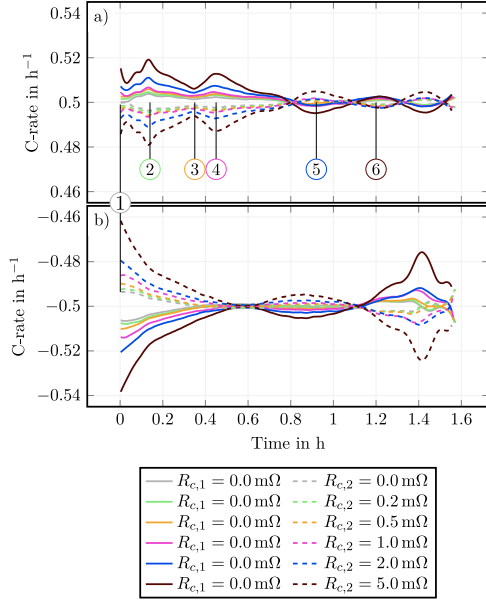


Fig. 5. Current distribution with the virtual parallel connection within inhomogeneous interconnection resistances. The resistance of path 1 was held at 0 mΩ while the interconnection resistance of path 2 was varied from 0 mΩ to 5 mΩ. Measurements were conducted during CC charging in (a) and discharging in (b) with a homogeneous current in each branch of 0.5 C. The marked circles correspond to local minima and maxima and are used in further analyses. (For interpretation of the references to colour in this figure legend, the reader is referred to the web version of this article.)

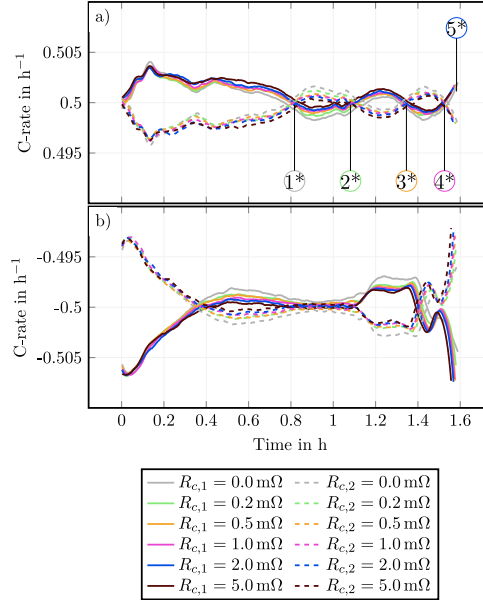


Fig. 6. Current distribution with the virtual measurement method and homogeneous interconnection resistances. The resistance of path 1 and of path 2 was varied from 0 mΩ to 5 mΩ. Measurements were conducted during CC charging in (a) and discharging in (b) with a homogeneous current in each branch of 0.5 C. The marked circles correspond to the intersection points of both currents, which are used in further analyses. (For interpretation of the references to colour in this figure legend, the reader is referred to the web version of this article.)

the cells are affected by the resistance ratios. Instead, the later two factors are dictated by the OCV interaction between the cells.

In a similar manner, the effect of increasing homogeneous path resistance on the current distribution was measured for CC charging and discharging, see Fig. 6. The current distribution with no additional resistance, $R_{c,x} = 0$ mΩ, echos the shape of Fig. 5. As expected, the current is very evenly distributed at the start of the measurement, as Eq. (4) suggests. During charging and discharging, the current distribution depends on the resistance of the paths, while higher additional resistances homogenise the current distribution. Nevertheless, the shape of the current distribution does not change significantly, and the intersection points of both currents only change marginally over the resistance increase.

A closer look at the progress of the intersection points of both currents, marked from ① to ⑥ on Fig. 6, is given in Fig. 7(b). Here the relative capacity at the intersection points of both currents over all charging cycles with a homogeneous current in each path of $i_{1/2} = 0.5$ C to study the influence of homogeneous resistance based on the first cycle is shown. Measurements were conducted three times at each resistance level. Analysing the behaviour of the intersection points of both currents as the cycles increase, some trends are visible. Intersection points ① and ③ generally occur at higher capacities as the number of cycles increase, whereas intersection points ② and ④ generally occur at lower capacities as the number of cycles increase. However ④ correlates with ⑤, which represents the capacity of the CC fully charged cell. The alteration in the intersections over time may indicate ageing, as reported in [48,49], however this cannot be stated conclusively in this paper.

The same behaviour is also reported by Fill et al. in [12], where the influence of cable resistances was pinpointed within measurements. That paper also showed an independence between the intersection points of the currents and the resistance differences between parallel-connected cells. To analyse this in detail, the current distribution is compared with the DVA in the following paragraphs.

The DVA can be used for chemical investigation [48], as well as to detect degradation mechanisms, where the characteristics of the DVA can be evaluated to determine different ageing contributions as loss of lithium inventory (LLI) and loss of active material (LAM) [50, 51]. Hust [18] explained current distribution based on the change of the OCV. With a DVA analysis of 27 parallel-connected cells, regions of an increased importance of the impedances and regions of increased importance of the OCV were noted. According to Hofmann et al. [6] a change in the OCV gradient influences the current distribution by causing an increase or decrease in the OCV differences between the cells. With this in mind, a DVA was carried out in this work during a 2p measurement. As a DVA provides clearer results at lower currents, the system current, i_{tot} was therefore set to 0.1 C [52]. This allowed a deeper analysis of the 2p DVA. The DVA is usually plotted over the capacity or the SoC during a CC charge or discharge. However, because the path current does not remain constant during the 2p measurement, and therefore the DVA of the 2p measurement is plotted over the voltage in this work.

Fig. 8 illustrates the analysis of the current distribution within the DVA. The corresponding DVA is illustrated in Fig. 8(b) and is normalised by the measured capacity, Q_0 , as performed by [52]. Additionally, the dashed lines in Fig. 8(b) and (c) were extracted from Sturm

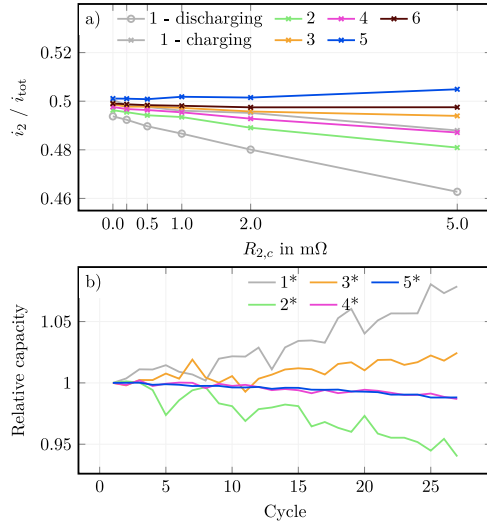


Fig. 7. Analysis of minima and maxima as well as intersection points of both currents. (a) shows the current spread at different points within different additional resistances due to an inhomogeneous load of Fig. 5. (b) shows the relative progress of intersection points of both currents according to Fig. 6 over all cycles within the investigation of homogeneous resistance in aspect to the loaded charge. (For interpretation of the references to colour in this figure legend, the reader is referred to the web version of this article.)

et al. [53] and illustrate the contribution of the SiC anode and the nickel-rich NMC cathode to the DVA of the full cell. The dashed yellow lines in Fig. 8(b) and (c) correspond to the same measurement data, whereby the x-axis is set to voltage in Fig. 8(b) and to capacity in (c). For a better comparison, the data of the 2p measurement is shifted on the x-axis to match with data of [53]. Although the cell batch and the measurement current in this work and in [53] differ, the corresponding DVA during the 2p measurement and the full cell of [53] show similarities, see Fig. 8(b).

Even though the current distribution of the 2p measurement shows more characteristic peaks compared to the DVA, some local minima and maxima within the current through path 2, i_2 , appear in almost the same region as the local minima and maxima of the 2p DVA. By assigning different peaks of both half cell profiles of the DVA to the anode and the cathode, see Fig. 8(c), the current distribution of both currents should be affected by these characteristic peaks. The pink arrows correspond to significant peaks belonging to the cathode and the blue arrows correspond to significant points belonging to the cathode. A clear explanation of the shape at low currents in Fig. 8 is still pending and will be continued in a subsequent work.

Additional ongoing investigations will focus on the development of the intersection points of both currents as a function of ageing. Nevertheless, the results of this work allow the conclusion, that the resistance ratio is responsible for the values of the local minima and maxima, whilst the DVA defines the shape of the current distribution.

4. Conclusion

This work presented a novel measurement technique to investigate the current distribution in parallel-connected cells. The cells were connected in parallel using Kirchhoff's laws and a battery cycler. By using the 4-wire measurement technique for each cell, the influence of

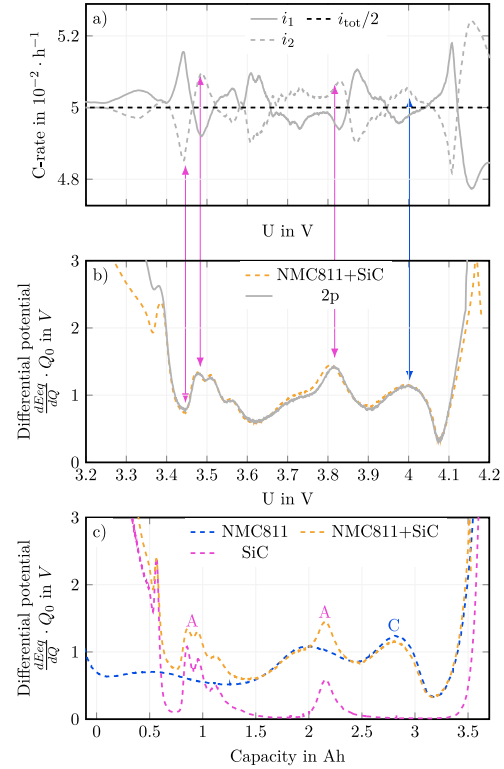


Fig. 8. Analysis of the DVA with the current distribution. (a) shows the current distribution between two parallel-connected cells with a homogeneous current in each branch of 0.05 C. The corresponding DVA during the 2p measurement is shown in (b). Additionally, the dashed lines in (b) and (c) were extracted from [53] and correspond to the half cell profiles and full cells of this cell type with assigned characteristic material markers. The arrows show some areas where the local minima and maxima between the current i_2 and DVA appear on the same voltage level. (For interpretation of the references to colour in this figure legend, the reader is referred to the web version of this article.)

system parameters such as interconnections and measurement equipment could be neglected, as is important for an exact and reproducible measurement setup. The novel measurement method was validated using a conventional test bench in charge and in discharge phases within CC, CV and resting periods. Measurement data showed good qualitative and quantitative agreement between the two measurement setups in regard to the local minima and maxima as well as the intersection points of both currents. The RMS was calculated to compare the measurements and showed low deviations of approximately 0.11 % across various charging phases and approximately 0.45 % across corresponding discharge phases.

To understand the influence of additional resistances in two parallel-connected cells, two measurement studies were carried out in which interconnection resistances were varied from 0 m Ω to 5 m Ω . Study one investigated the influence of an additional resistance in one parallel path, whilst study two addresses the influence of additional resistances in both parallel paths. The conclusion of both studies is, that the height of the local minima and maxima are mainly dependent on the

resistance ratio. They divide relative to the ratio of the combined cell and interconnection resistance in each pathway. In contrast, neither the local minima and maxima measured at various cumulative charge throughputs nor the intersection points of the current distribution are affected by varied resistances. OCV interactions between both cells determine the shape of the current distribution. Additionally, the shape of the DVA showed correlations with current distribution.

Using the tools set out in this work, the driving forces for convergence and divergence of the current distribution can be determined. As the cells are only ever connected in parallel via equations, it is possible to decouple the cells for check-ups and recouple them for cycling without ever touching them. This avoids any alteration of the contact resistance [4]. Additionally, with the flexibility of the virtual parallel connection, different cell formats can be investigated with less effort.

Based on the findings of these work, additional studies should be carried out. Ongoing work will focus on the ageing behaviour of parallel connected LIBs, influence of other electrode chemistry combinations as well as further analysis of the correlation between DVA, the intersection points of both currents and current distribution.

CRediT authorship contribution statement

P. Jocher: Conceptualization, Methodology, Software, Project administration, Writing - original draft, Visualization, Data curation, Investigation, Writing - review & editing. **M. Steinhardt:** Conceptualization, Writing - review & editing. **S. Ludwig:** Conceptualization, Writing - review & editing. **M. Schindler:** Writing - review & editing. **J. Martin:** Software, Conceptualization, Writing - review & editing. **A. Jossen:** Writing - review & editing, Supervision.

Declaration of competing interest

The authors declare that they have no known competing financial interests or personal relationships that could have appeared to influence the work reported in this paper.

Acknowledgements

Received funding from the Bavarian Research Foundation of the project OparaBatt, Germany (AZ-1296-17) and supported by the German Federal Ministry of Education and Research (BMBF), Germany under grant number 03XP0330A-F (OSLIB) is gratefully acknowledged. The responsibility for this publication rests with the authors.

References

- [1] L. Noel, G. Zarazua de Rubens, B.K. Sovacool, J. Kester, Fear and loathing of electric vehicles: The reactionary rhetoric of range anxiety, *Energy Res. Soc. Sci.* 48 (2019) 96–107, <http://dx.doi.org/10.1016/j.erss.2018.10.001>.
- [2] B. Tarroja, L. Zhang, van Wifrat, B. Shaffer, S. Samuelsen, Assessing the stationary energy storage equivalency of vehicle-to-grid charging battery electric vehicles, *Energy* 106 (2016) 673–690, <http://dx.doi.org/10.1016/j.energy.2016.03.094>.
- [3] S. Kasap, P. Capper, *Springer Handbook of Electronic and Photonic Materials*, Springer International Publishing, Cham, 2017, <http://dx.doi.org/10.1007/978-3-319-48933-9>.
- [4] M.J. Brand, P. Berg, E.I. Kolp, T. Bach, P. Schmidt, A. Jossen, Detachable electrical connection of battery cells by press contacts, *J. Energy Storage* 8 (2016) 69–77, <http://dx.doi.org/10.1016/j.est.2016.09.011>.
- [5] A. Fill, T. Mader, T. Schmidt, R. Llorente, K.P. Birke, Measuring test bench with adjustable thermal connection of cells to their neighbors and a new model approach for parallel-connected cells, *Batteries* 6 (1) (2020) 2, <http://dx.doi.org/10.3390/batteries6010002>.
- [6] M.H. Hofmann, K. Czyrka, M.J. Brand, M. Steinhardt, A. Noel, F.B. Spingler, A. Jossen, Dynamics of current distribution within battery cells connected in parallel, *J. Energy Storage* 20 (2018) 120–133, <http://dx.doi.org/10.1016/j.est.2018.08.013>.
- [7] M.P. Klein, J.W. Park, Current distribution measurements in parallel-connected lithium-ion cylindrical cells under non-uniform temperature conditions, *J. Electrochem. Soc.* 164 (9) (2017) A1893–A1906, <http://dx.doi.org/10.1149/2.0011709jes>.
- [8] Z. Wei, J. Zhao, H. He, G. Ding, H. Cui, L. Liu, Future smart battery and management: Advanced sensing from external to embedded multi-dimensional measurement, *J. Power Sources* 489 (1) (2021) 229462, <http://dx.doi.org/10.1016/j.jpowsour.2021.229462>.
- [9] F. An, J. Huang, C. Wang, Z. Li, J. Zhang, S. Wang, P. Li, Cell sorting for parallel lithium-ion battery systems: Evaluation based on an electric circuit model, *J. Energy Storage* 6 (2016) 195–203, <http://dx.doi.org/10.1016/j.est.2016.04.007>.
- [10] T. Bruen, J. Marco, Modelling and experimental evaluation of parallel connected lithium ion cells for an electric vehicle battery system, *J. Power Sources* 310 (2016) 91–101, <http://dx.doi.org/10.1016/j.jpowsour.2016.01.001>.
- [11] M. Dubarry, A. Devie, B.Y. Liaw, Cell-balancing currents in parallel strings of a battery system, *J. Power Sources* 321 (2016) 36–46, <http://dx.doi.org/10.1016/j.jpowsour.2016.04.125>.
- [12] A. Fill, T. Schmidt, T. Mader, R. Llorente, A. Avdylii, B. Mulder, K.P. Birke, Influence of cell parameter differences and dynamic current stresses on the current distribution within parallel-connected lithium-ion cells, *J. Energy Storage* 32 (2020) 101929, <http://dx.doi.org/10.1016/j.est.2020.101929>.
- [13] M. Fleckenstein, O. Bohlen, M.A. Roscher, B. Bäker, Current density and state of charge inhomogeneities in li-ion battery cells with lifepo4 as cathode material due to temperature gradients, *J. Power Sources* 196 (10) (2011) 4769–4778, <http://dx.doi.org/10.1016/j.jpowsour.2011.01.043>.
- [14] R. Gogoana, M.B. Pinson, M.Z. Bazant, S.E. Sarma, Internal resistance matching for parallel-connected lithium-ion cells and impacts on battery pack cycle life, *J. Power Sources* 252 (2014) 8–13, <http://dx.doi.org/10.1016/j.jpowsour.2013.11.101>.
- [15] X. Gong, R. Xiong, C.C. Mi, Study of the characteristics of battery packs in electric vehicles with parallel-connected lithium-ion battery cells, *IEEE Trans. Ind. Appl.* 51 (2) (2015) 1872–1879, <http://dx.doi.org/10.1109/TIA.2014.2345951>.
- [16] T. Grün, K. Stella, O. Wollersheim, Influence of circuit design on load distribution and performance of parallel-connected lithium ion cells for photovoltaic home storage systems, *J. Energy Storage* 17 (2018) 367–382, <http://dx.doi.org/10.1016/j.est.2018.03.010>.
- [17] I. Hunt, T. Zhang, Y. Patel, M. Marinescu, R. Purkayastha, P. Kovacic, S. Walus, A. Swiatek, G.J. Offer, The effect of current inhomogeneity on the performance and degradation of li-s batteries, *J. Electrochem. Soc.* 165 (1) (2018) A6073–A6080, <http://dx.doi.org/10.1149/2.0141801jes>.
- [18] F. Hust, Physico-Chemically Motivated Parameterization and Modelling of Real-Time Capable Lithium-Ion Battery Models - a Case Study on the Tesla Model S Battery (Ph.D. thesis), RWTH AACHEN UNIVERSITÄT, Aachen, 2018, <http://dx.doi.org/10.18154/RWTH-2019-00249>.
- [19] S. Miyatake, Y. Susuki, T. Hikiyama, S. Itoh, K. Tanaka, Discharge characteristics of multicell lithium-ion battery with nonuniform cells, *J. Power Sources* 241 (2013) 736–743, <http://dx.doi.org/10.1016/j.jpowsour.2013.05.179>.
- [20] A.S. Mussa, M. Klett, G. Lindbergh, R.W. Lindström, Effects of external pressure on the performance and ageing of single-layer lithium-ion pouch cells, *J. Power Sources* 385 (2018) 18–26, <http://dx.doi.org/10.1016/j.jpowsour.2018.03.020>.
- [21] C. Pastor-Fernández, T. Bruen, W.D. Widanage, M.A. Gama-Valdez, J. Marco, A study of cell-to-cell interactions and degradation in parallel strings: Implications for the battery management system, *J. Power Sources* 329 (2016) 574–585, <http://dx.doi.org/10.1016/j.jpowsour.2016.07.121>.
- [22] Y. Pan, X. Feng, M. Zhang, X. Han, L. Lu, M. Ouyang, Internal short circuit detection for lithium-ion battery pack with parallel-series hybrid connections, *J. Cleaner Prod.* 255 (2020) 120277, <http://dx.doi.org/10.1016/j.jclepro.2020.120277>.
- [23] W. Shi, X. Hu, C. Jin, J. Jiang, Y. Zhang, T. Yip, Effects of imbalanced currents on large-format lifepo 4 /graphite batteries systems connected in parallel, *J. Power Sources* 313 (2016) 198–204, <http://dx.doi.org/10.1016/j.jpowsour.2016.02.087>.
- [24] G. Zhang, C.E. Shaffer, C.-Y. Wang, C.D. Rahn, In-situ measurement of current distribution in a li-ion cell, *J. Electrochem. Soc.* 160 (4) (2013) A610–A615, <http://dx.doi.org/10.1149/2.046304jes>.
- [25] M. Zhang, M. Ouyang, L. Lu, X. He, X. Feng, L. Liu, X. Xie, Battery internal short circuit detection, *ECS Trans.* 77 (11) (2017) 217–223, <http://dx.doi.org/10.1149/07711.0217ecst>.
- [26] Y. Zhang, J. Zheng, S. Lin, F. Bai, W.H. Tanveer, S. Cha, X. Wu, W. Feng, Nonuniform current distribution within parallel-connected batteries, *Int. J. Energy Res.* 42 (8) (2018) 2835–2844, <http://dx.doi.org/10.1002/er.4039>.
- [27] M.J. Brand, P.A. Schmidt, M.F. Zaeh, A. Jossen, Welding techniques for battery cells and resulting electrical contact resistances, *J. Energy Storage* 1 (2015) 7–14, <http://dx.doi.org/10.1016/j.est.2015.04.001>.
- [28] M.J. Brand, M.H. Hofmann, M. Steinhardt, S.F. Schuster, A. Jossen, Current distribution within parallel-connected battery cells, *J. Power Sources* 334 (2016) 202–212, <http://dx.doi.org/10.1016/j.jpowsour.2016.10.010>.
- [29] M.J. Brand, E.I. Kolp, P. Berg, T. Bach, P. Schmidt, A. Jossen, Electrical resistances of soldered battery cell connections, *J. Energy Storage* 12 (2017) 45–54, <http://dx.doi.org/10.1016/j.est.2017.03.019>.

- [30] P. Taheri, S. Hsieh, M. Bahrami, Investigating electrical contact resistance losses in lithium-ion battery assemblies for hybrid and electric vehicles, *J. Power Sources* 196 (15) (2011) 6525–6533, <http://dx.doi.org/10.1016/j.jpowsour.2011.03.056>.
- [31] M. Baumann, L. Wildfeuer, S. Rohr, M. Lienkamp, Parameter variations within lithium-ion battery packs – theoretical investigations and experimental quantification, *J. Energy Storage* 18 (2018) 295–307, <http://dx.doi.org/10.1016/j.est.2018.04.031>.
- [32] S. Paarmann, L. Cloos, J. Technau, T. Wetzel, Measurement of the temperature influence on the current distribution in lithium-ion batteries, *Energy Technol.* 158 (2021) 2000862, <http://dx.doi.org/10.1002/ente.202000862>.
- [33] J. Sturm, A. Rheinfield, I. Zilberman, F.B. Spingler, S. Kosch, F. Frie, A. Jossen, Modeling and simulation of inhomogeneities in a 18650 nickel-rich, silicon-graphite lithium-ion cell during fast charging, *J. Power Sources* 412 (2019) 204–223, <http://dx.doi.org/10.1016/j.jpowsour.2018.11.043>.
- [34] T.M.M. Heenan, A. Jnawali, M.D.R. Kok, T.G. Tranter, C. Tan, A. Dimitrijevic, R. Jarvis, D.J.L. Brett, P.R. Shearing, An advanced microstructural and electrochemical datasheet on 18650 li-ion batteries with nickel-rich NMC811 cathodes and graphite-silicon anodes, *J. Electrochem. Soc.* 167 (14) (2020) 140530, <http://dx.doi.org/10.1149/1945-7111/abc4c1>.
- [35] K. Rumpf, M. Naumann, A. Jossen, Experimental investigation of parametric cell-to-cell variation and correlation based on 1100 commercial lithium-ion cells, *J. Energy Storage* 14 (2017) 224–243, <http://dx.doi.org/10.1016/J.EST.2017.09.010>.
- [36] I. Zilberman, S. Ludwig, A. Jossen, Cell-to-cell variation of calendar aging and reversible self-discharge in 18650 nickel-rich, silicon-graphite lithium-ion cells, *J. Energy Storage* 26 (2019) 100900, <http://dx.doi.org/10.1016/j.est.2019.100900>.
- [37] M. Schindler, J. Sturm, S. Ludwig, J. Schmitt, A. Jossen, Evolution of initial cell-to-cell variations during a three-year production cycle, *eTransportation* (2021) 100102, <http://dx.doi.org/10.1016/j.etrans.2020.100102>.
- [38] M.H. Hofmann, *Current Distribution in Parallel-Connected Battery Cells*, Vol. 1, Auflage ed., Verlag Dr. Hut, München, 2020, URL: <https://www.dr.hut-verlag.de/9783843946148.html>.
- [39] A. Cordoba-Arenas, S. Onori, G. Rizzoni, A control-oriented lithium-ion battery pack model for plug-in hybrid electric vehicle cycle-life studies and system design with consideration of health management, *J. Power Sources* 279 (8) (2015) 791–808, <http://dx.doi.org/10.1016/j.jpowsour.2014.12.048>.
- [40] P.-L. Huynh, *Beitrag Zur Bewertung Des Gesundheitszustands Von Traktionsbatterien in Elektrofahrzeugen*, Springer Fachmedien Wiesbaden, Wiesbaden, 2016, <http://dx.doi.org/10.1007/978-3-658-16562-8>.
- [41] N. Kakimoto, K. Goto, Capacity-fading model of lithium-ion battery applicable to multicell storage systems, *IEEE Trans. Sustain. Energy* 7 (1) (2016) 108–117, <http://dx.doi.org/10.1109/TSTE.2015.2476476>.
- [42] S.F. Schuster, M.J. Brand, P. Berg, M. Gleissenberger, A. Jossen, Lithium-ion cell-to-cell variation during battery electric vehicle operation, *J. Power Sources* 297 (2015) 242–251, <http://dx.doi.org/10.1016/j.jpowsour.2015.08.001>.
- [43] C.R. Birkel, M.R. Roberts, E. McTurk, P.G. Bruce, D.A. Howey, Degradation diagnostics for lithium ion cells, *J. Power Sources* 341 (1) (2017) 373–386, <http://dx.doi.org/10.1016/j.jpowsour.2016.12.011>.
- [44] R.A. Maronna, D.R. Martin, V.J. Yohai, M. Salibián-Barrera, *Robust Statistics: Theory and Methods (with R)*, second ed., in: *Wiley Series in Probability and Statistics Ser.*, John Wiley & Sons Incorporated, Newark, 2018, URL: <https://ebookcentral.proquest.com/lib/gbv/detail.action?docID=5568377>.
- [45] S. Gantenbein, M. Weiss, E. Ivers-Tiffée, Impedance based time-domain modeling of lithium-ion batteries: Part i, *J. Power Sources* 379 (2018) 317–327, <http://dx.doi.org/10.1016/j.jpowsour.2018.01.043>.
- [46] W. Waag, S. Käbitz, D.U. Sauer, Experimental investigation of the lithium-ion battery impedance characteristic at various conditions and aging states and its influence on the application, *Appl. Energy* 102 (2013) 885–897, <http://dx.doi.org/10.1016/j.apenergy.2012.09.030>.
- [47] I. Zilberman, J. Schmitt, S. Ludwig, M. Naumann, A. Jossen, Simulation of voltage imbalance in large lithium-ion battery packs influenced by cell-to-cell variations and balancing systems, *J. Energy Storage* 32 (2020) 101828, <http://dx.doi.org/10.1016/j.est.2020.101828>.
- [48] H.-J. Noh, S. Youn, C.S. Yoon, Y.-K. Sun, Comparison of the structural and electrochemical properties of layered $\text{Li}[\text{Ni}_{1-x}\text{Co}_x\text{Mn}_x]\text{O}_2$ ($x = 1/3, 0.5, 0.6, 0.7, 0.8$ and 0.85) cathode material for lithium-ion batteries, *J. Power Sources* 233 (2013) 121–130, <http://dx.doi.org/10.1016/j.jpowsour.2013.01.063>.
- [49] D. Anseán, G. Baure, M. González, I. Camaño, A.B. García, M. Dubarry, Mechanistic investigation of silicon-graphite/ $\text{LiNi}_0.8\text{Mn}_0.1\text{Co}_0.1\text{O}_2$ commercial cells for non-intrusive diagnosis and prognosis, *J. Power Sources* 459 (2020) 227882, <http://dx.doi.org/10.1016/j.jpowsour.2020.227882>.
- [50] P. Keil, S.F. Schuster, J. Wilhelm, J. Travi, A. Hauser, R.C. Karl, A. Jossen, Calendar aging of lithium-ion batteries, *J. Electrochem. Soc.* 163 (9) (2016) A1872–A1880, <http://dx.doi.org/10.1149/2.0411609jes>.
- [51] M. Dubarry, C. Truchot, B.Y. Liaw, Synthesize battery degradation modes via a diagnostic and prognostic model, *J. Power Sources* 219 (2012) 204–216, <http://dx.doi.org/10.1016/j.jpowsour.2012.07.016>.
- [52] I. Bloom, A.N. Jansen, D.P. Abraham, J. Knuth, S.A. Jones, V.S. Battaglia, G.L. Henriksen, Differential voltage analyses of high-power, lithium-ion cells, *J. Power Sources* 139 (1–2) (2005) 295–303, <http://dx.doi.org/10.1016/j.jpowsour.2004.07.021>.
- [53] J. Sturm, A. Frank, A. Rheinfield, S.V. Erhard, A. Jossen, Impact of electrode and cell design on fast charging capabilities of cylindrical lithium-ion batteries, *J. Electrochem. Soc.* 167 (13) (2020) 130505, <http://dx.doi.org/10.1149/1945-7111/abb40c>.

5 Comparing Lithium-Ion and Sodium-Ion Technologies in Parallel Configuration by Sensitivity Factors

Up to now, electrical path resistances were presented, and a novel measurement technique was introduced. In summary, accurately determined path resistances can set as a boundary condition in a test-bench for measuring the current distribution. In this chapter, we use the VPC to analyze the influence of inhomogeneous path resistances of cells connected in parallel. In addition, the influence of inhomogeneous path temperature of parallel-connected cells is investigated.

In order to provide general information of inhomogeneities across different cell technologies, three cell technologies were investigated in a 2p configuration. Two LIB with NCA and LFP as cathode chemistries and an SIB with layered oxide as cathode material were investigated. The first part of the study investigated the inhomogeneous path resistances from 0 up to a resistance in the order of their internal resistance, R_{AC} . The second part of the study investigated the temperature difference of parallel-connected battery cells. Two different climate chambers were used to achieve a temperature difference between both battery cells of the same chemistry. The temperature of one cell was kept at 25 °C while the temperature of the other cell was varied between 15 and 35 °C. In a third study, the impact of the C-rate was quantified with three different current rates, ranging from 0.25 to 1 C.

The following parameters were used to compare all three cell technologies with each other: the maximum current of both cells, $i_{max,1}$, $i_{max,2}$ and the maximum SoC difference between both cells at two operating points: the overall maximum difference, $\max\Delta\text{SoC}$, and the ΔSoC at 80% $\text{SoC}_{\text{System}}$.

Sensitivity factors were introduced to assess the influence of inhomogeneous boundary conditions. For this purpose, the respective parameters are measured over the additional resistance and the temperature difference. For all the investigated inhomogeneities, an increase of the inhomogeneity showed a proportional change in the quantifiable parameters, $i_{max,x}$ and ΔSoC . The sensitivity factor is the slope of the linear fit over the added inhomogeneity.

Using these sensitivity factors, the following research questions were addressed. How sensitive are LIB_{NCA} , LIB_{LFP} and SIB to inhomogeneous path resistance and cell temperature differences? How does this affect the current distribution and what is the resulting SoC difference? → *Q5 How does an inhomogeneous contact resistance or path temperature influence the system performance in a parallel configuration?*

Due to the increase in maximum current and the differences in SoC, all three investigated cell technologies exhibit performance losses across both investigated inhomogeneities. The SIB shows the smallest sensitivity to inhomogeneous path resistance but showed the greatest R_{DC} , see Table 2.1. In contrast, due to the flat OCV the LIB_{LFP} resulted in the most inhomogeneous behavior. The LIB_{NCA} overall shows the lowest sensitivity regarding path resistance and temperature.

Authors Contribution

Philipp Jocher designed the study. With the help of Adrian Himmelreich and Totilo Idrizi, Philipp Jocher conducted the electrical experiments and evaluated the experimental data. Franz Roehrer and Mathias Rhem supported the manuscript and measurement procedure. Philipp Jocher wrote the manuscript with the help of Franz Roehrer. Andreas Jossen supervised the work. All authors discussed the data, commented on the results, and reviewed the manuscript.

Scaling from Cell to System: Comparing Lithium-ion and Sodium-ion Technologies Regarding Inhomogeneous Resistance and Temperature in Parallel Configuration by Sensitivity Factors

Joher P., Roehrer F., Rehm F., Idrizi T., Himmelreich, A. and Jossen A.

Journal of Energy Storage 98 (2024) 112931

Permanent weblink:

<https://doi.org/10.1016/j.est.2024.112931>



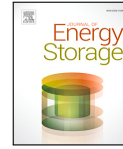
Reproduced under the terms of the Creative Commons Attribution 4.0 License (CC BY, <http://creativecommons.org/licenses/by/4.0/>), which permits unrestricted reuse of the work in any medium, provided the original work is properly cited.



Contents lists available at ScienceDirect

Journal of Energy Storage

journal homepage: www.elsevier.com/locate/est



Research papers

Scaling from cell to system: Comparing Lithium-ion and Sodium-ion technologies regarding inhomogeneous resistance and temperature in parallel configuration by sensitivity factors

P. Jocher*, F. Roehrer, M. Rehm, T. Idrizi, A. Himmelreich, A. Jossen

Technical University of Munich (TUM), TUM School of Engineering and Design, Department of Energy and Process Engineering, Chair of Electrical Energy Storage Technology, Arcisstr. 21, 80333 Munich, Germany



ARTICLE INFO

Keywords:

Current distribution
Lithium-ion
Sodium-ion
Battery system
Parallel connection

ABSTRACT

Understanding the strengths and limitations of different cell technologies is vital for effectively scaling from cell to system level. In any group of cells connected in parallel, inhomogeneous current flow can occur. To better understand the factors influencing current distribution, we conducted a sensitivity analysis focusing on the effects of inhomogeneous contact resistances and unequal cell temperatures. This analysis was carried out on several state-of-the-art battery chemistries, with Sodium-Ion Batteries and Lithium-Ion Batteries using both NCA and LFP as cathode materials. Our study reveals that both investigated inhomogeneities result in unique outcomes for different cell technologies, such as fluctuations in maximum currents and differences in SoC. By introducing sensitivity factors, LIB_{LFP} show the highest deviations due to its flat open-circuit-voltage characteristics. This leads to maximum SoC differences of up to 14.8%/ R_{AC} and 7.46%/K between the cells. In contrast, the SIB current distribution shows significantly lower sensitivity to resistance but higher sensitivity to temperature inhomogeneities. The LIB_{NCA} technology demonstrates comparatively low sensitivity to both investigated inhomogeneities. Our results show that, when selecting a cell type for a particular application, it is crucial to consider the effect of contact resistance and temperature inequalities on current distribution.

1. Introduction

Given the rapid development of electrical energy storage systems in stationary and mobile applications, it is essential to investigate cells' electrical, mechanical, and thermal behavior. Many laboratory studies focus on the single-cell level which offers useful insights at low current and voltage levels. This has the advantage of reduced effort, cost, and safety risks, compared to multi-cell systems. In real applications, multiple cells are connected in series and parallel to achieve the desired energy and required system voltage.

To increase system voltage, cells are connected in series, however the voltages of each logical cell can drift apart during operation and limit the accessible system energy [1]. By actively monitoring the individual cell voltages and implementing appropriate control algorithms, balancing systems can ensure that each cell operates within a specified voltage range [2].

Cells connected in parallel are vulnerable to significant reductions in performance and longevity if they experience inhomogeneous current flows [3]. As a result, different electrical, mechanical, and thermal boundary conditions have been investigated to understand effects on

current distribution in such systems. In lithium battery systems, intrinsic cell parameter variations [3–11] and aging [8,10,12–16] have been widely investigated. Other studies focus on external boundary conditions such as variations in contact resistance [17–19], different State of Health (SoH) between the cells under test [12,19] and the effects of external temperature gradients [14–16,20,21].

The influence of intrinsic resistance and capacity differences on the initial current distribution has been demonstrated in the literature. According to Brand et al. [3] the resistance ratio defines the initial current distribution according to the current divider, whereas long-term differences in current distribution are attributed to differences in capacity. Additionally, it was shown that the current distribution's minima and maxima vary linearly with an incremental increase in the contact resistance and that the shape of the current distribution vs. SoC is determined by the OCV differences between the cells [17].

Several authors have investigated the influence of a temperature gradient between Lithium-Ion (LI) cells connected in parallel. Klein and Park [20] used Nickel Manganese Cobalt (NMC) and LFP cells and investigated them by using a shunt-based test-bench for connecting

* Corresponding author.

E-mail address: philipp.jocher@tum.de (P. Jocher).

<https://doi.org/10.1016/j.est.2024.112931>

Received 22 January 2024; Received in revised form 2 June 2024; Accepted 8 July 2024

Available online 27 July 2024

2352-152X/© 2024 The Authors. Published by Elsevier Ltd. This is an open access article under the CC BY license (<http://creativecommons.org/licenses/by/4.0/>).

five 18 650 cells in parallel. Within a temperature gradient between 5 to 20 °C, current differences, up to 1.8 times the nominal current, occurred [20].

The development of aging in the presence of temperature gradients between the cells has also been investigated in the literature. Naylor Marlow et al. [14] carried out an aging study investigating the effects of thermal gradients on cells connected in parallel. A divergent capacity fade between parallel connected LI cells was observed in a temperature gradient of 20 to 45 °C. [14] Cavalheiro et al. [15] carried out an aging study on a stack of five pouch non-identified chemistry LI cells connected in parallel at a temperature of 25 °C. The cell located at the center of the stack experienced a significantly accelerated capacity fade and resistance increase. This was linked to higher local temperatures up to 8 °C greater than the ambient temperature. While cycling, the middle cell's current deviated considerably from that of the other four and reached peak values of up to 1.5 times the nominal current, whereas the current profiles of the outer cells remained relatively stable [15]. The aging effects in a module of four parallel NMC cells under a forced temperature gradient of 10 °C were examined by Al-Amin et al. [16]. The cell exposed to the elevated temperature degraded the fastest, which is attributed to the combined effects of higher temperature and current throughput. Nevertheless, an unheated cell with a lower initial capacity underwent the highest current peaks of up to 1.4 times the nominal current, which led to an accelerated increase in its resistance [16].

While it is well-known that inhomogeneities lead to faster aging, it is unclear which boundary conditions affect convergence or divergence of the SoH of the cells. While some studies state that different boundary conditions result in a diverging of the capacity of the individual LI cells [5,13,22], others find that capacity converges in parallel LI cells as aging progresses [10,12]. Shi et al. [13] conducted an aging study with parallel connected LFP cells displaying different SoH. Using a shunt of 0.25 mΩ, a diverging of the cell capacities was measured during aging. Contrary to that, Pastor-Fernández et al. [12] analyzed non-identified parallel connected LI cells with varying SoH and found a converging behavior. Four 3 Ah cells were aged to different SoHs. Subsequently, the cells were further cycled in parallel using 10 mΩ shunts. Both the capacity and resistance of the individual cells showed a convergence [12].

Moreover, Cui et al. [19] carried out experiments to investigate the effects of different SoH, 2–18%, and contact resistances, 5–25 mΩ, on the current distribution of two NMC cells in parallel. Current peaks reaching 1.38 and 1.3 times the nominal current, respectively, were observed [19]. Further, Ma et al. [18] varied both the contact and the internal resistance of NMC cells in parallel and analyzed the effects on system performance. The research revealed that these inhomogeneities yield comparable current profiles, but the maximum current peaks and SoC differences in charge and discharge direction differ [18].

Studies regarding the current distribution mainly focus on the 2p level. An advantage of conducting investigations at the 2p level is the directly coupled behavior of the two cells. This allows for a targeted investigation of the influence of boundary conditions. When scaling to the n parallel (np) level, each cell affects the others, complicating the analysis. Nevertheless, studying and analyzing behavior at the np level is important as it allows insights into the behavior of real systems containing large numbers of cells. Some researchers try to scale the investigations from 2p to np with Monte Carlo simulations [9,23,24]. For instance, by varying cell resistance, capacity, and number of parallel LI cells Fill et al. [9] investigated the different effects on the current distribution based on a ECM model. According to the Monte Carlo simulations, increasing the number of parallel connected cells increases current inhomogeneities and SoC imbalances [9].

For all experimental studies, a high precision test-bench is vital. Differences between the resistances of each parallel path can significantly influence the current distribution and the measurement results [17]. Consequently, the coupling and decoupling of connections in laboratory test-benches to allow single cells to be measured may alter

the contact resistance of the connections. Naylor Marlow et al. [14] found variations in the current distribution caused by differences in the contact resistance. This was, in turn, attributed to repeated assembly and disassembly of the packs.

Several studies have explored current distribution, employing various experimental setups and investigating diverse boundary conditions across distinct LIB cell technologies. Nevertheless, a clear comparison between cell technologies within the same test-bench is still missing. By using conventional setups, for example, the influence of contact resistance is a difficult parameter to adjust. In addition, the temperature was usually applied via a gradient and not cell individual. A targeted adjustment of both parameters, cell temperature and contact resistance, has not yet been possible in experimental studies. This work uses the virtual parallel connection, where each parallel-connected cell can have specific boundary conditions.

Three different state-of-the-art cells are investigated under several sets of inhomogeneous parallel path conditions, namely contact resistance and cell temperature. Contact resistances encompass any additional potential drop due to contacting, wiring, and measurement equipment. Two LIB with differing cathode chemistries are investigated (i.e., NCA, and LFP) as well as an SIB with a layered oxide as cathode material. These cells were used to research the following questions:

- What are the strengths and challenges of different cell technologies (LIB_{NCA}, LIB_{LFP} and SIB) when placed in parallel systems?
- How sensitive are LIB_{NCA}, LIB_{LFP} and SIB to inhomogeneous contact resistance and cell temperature differences?
 - What is the effect on the current distribution?
 - What is the resulting SoC difference?
- What are the consequences for their application in battery systems?

2. Experimental

2.1. Cell specifications

Three 18 650 cells were selected to investigate the strengths and challenges regarding their scalability from cell to system. These include a LIB_{NCA} made by Samsung SDI, a LIB_{LFP} made by Haidi Energy Group, and a SIB, with layered oxide as cathode material, made by Shenzhen Mushang Electronics. Table 1 summarizes the cell data, either taken from the appropriate data sheets or measured at 25 °C.

The capacity, C_{meas} , was determined based on a constant current constant voltage phase (CCCV) charge with a CC rate of 0.2 C, followed by a constant voltage phase (CV) at the cell-specific upper voltage limit U_{charge} until a cut-off current equivalent to 0.02 C. Subsequently, the cell was discharged to 50% SoC and left to relax for 30 min. Following this, the R_{DC} resistance was assessed by calculating the ratio of the voltage response, observed 10 s after applying a current pulse equivalent to 0.67 C, to the magnitude of the pulse itself. Therefore, the checkup included two charge and discharge phases, followed by resistance, R_{DC} , measurement at 50% SoC. Before the study, Z_{AC} was determined by Galvanostatic Electrochemical Impedance Spectroscopy (GEIS) with a current amplitude of 140 mA at 50% SoC, using a VMP3 potentiostat from Biologic Science Instruments SAS. The AC resistance, R_{AC} , of the cell was defined as the intercept of the Nyquist plot with the real axis, i.e., where $Z_{\text{AC}, \text{Im} \rightarrow 0}$.

The LIB_{NCA} cells exhibit the lowest R_{AC} resistance at 20.2 mΩ, followed by SIB at 25.4 mΩ and LIB_{LFP} at 27.9 mΩ. Additionally, a distinct behavior among the different investigated cell technologies is evident in the ratio of R_{DC} to R_{AC} . The LIB_{NCA} cells display the lowest ratio at 1.83, while SIB cells exhibit the highest ratio at 3.35. Several cell pairs were measured, but only one cell pair was considered in this work. The other cell pairs showed similar results.

The resulting mean and standard deviations of the cell parameters C_{meas} and R_{AC} for all investigated cell pairs are presented in Table 1. This spread in the cell parameters intrinsically influences the current distribution of the 2p-connected cells [3].

Table 1
Specifications of the investigated cells. The measurements were carried out at 25 °C; resistance measurements were taken at 50% SoC.

Parameter	Symbol	LIB _{NCA}	LIB _{LFP}	SIB
Identifier ^a	–	INR18650-35E	HDCFI8650-1800	NA18650-1250
Manufacturer ^a	–	Samsung SDI	HAI DI Energy Group	Shenzhen Mushang
Format ^a	–	18 650	18 650	18 650
Nominal capacity in Ah ^b	C _N	3.35	1.80	1.25
Measured capacity in Ah ^b	C _{meas}	3.434 ± 0.004	1.860 ± 0.000	1.289 ± 0.016
Nominal voltage in V ^b	V _N	3.6	3.2	3.0
Lower voltage limit in V ^b	U _{discharge}	2.65	2	1.5
Upper voltage limit in V ^b	U _{charge}	4.2	3.65	3.8
Z _{ACZ_{meas}} in mΩ ^b	R _{AC}	20.2 ± 0.1	27.9 ± 0.2	25.4 ± 0.3
R _{DC,10 s} in mΩ ^b	R _{DC}	37.12 ± 0.05	58.4 ± 1.0	84.99 ± 0.01
R _{DC} /R _{AC} ^b	–	1.83 ± 0.02	2.13 ± 0.04	3.35 ± 0.04

^a Data extracted from datasheet.

^b Measured data.

2.2. Test-bench

Specific requirements must be fulfilled to examine the impact of inhomogeneous contact resistance. Firstly, an accurate measurement of the current distribution is essential, and influencing factors should be known and determinable. In addition, coupling and decoupling of parallel connections – to allow individual cells to be measured separately during the study – should be carried out without affecting the current distribution. Moreover, a setup that offers consistency and reproducibility is required to experiment simultaneously on multiple cell pairs. Fourthly, investigating the influence of different contact resistances requires the presence of defined and adjustable resistances.

The Virtual Parallel Connection (VPC) [17] was used to fulfill these requirements. The VPC allows the current distribution to be measured without the influence of inhomogeneous wiring, contact resistances, or an additional measurement environment. It is easily reproducible on multiple measurement channels, and the coupling and decoupling of parallel connections can be carried out without affecting the current distribution. A short overview is given to understand the principle.

First, the cells are not physically connected in parallel. Instead, they are connected to a battery cycler, with current flows to each cell determined by the controller. The controller solves Kirchhoff's equations for cells in parallel and supplies the appropriate current to the cells. This method allows cells to be connected and disconnected from the circuit without affecting or altering the contacts.

For a 2p connection, channel 1 is voltage controlled; the system is required to match the cell voltage of channel 1 to that of channel 2.

$$U_{\text{cell1}} = U_{\text{cell2}} + I_2 \cdot R_{c,2} - I_1 \cdot R_{c,1}. \quad (1)$$

Channel 2 is current controlled; the system sets I_2 as the difference of the total current, I_{tot} , and the current of channel 1, I_1

$$I_2 = I_{\text{tot}} - I_1. \quad (2)$$

This closed-loop system defines the VPC. During the measurement, all cells are connected by the 4-wire measurement technique, which eliminates the effects of uneven wiring, contact resistances, and additional sensors. Moreover, the VPC enables the inclusion of virtual and thus clearly defined contact resistances, $R_{c,1}$ and $R_{c,2}$, using Kirchhoff's voltage law, see Eq. (1). A detailed overview and validation with a conventional measurement setup are given in [17].

For all tests, a commercial battery cycler (BaSyTec, CTS) was used. All tests were conducted in a climate chamber. The cells were evenly distributed in the climate chamber to minimize temperature inhomogeneities and were heated by convection.

Contacting the cells

Contacting of the cells without any alternation of resistance and temperature is essential. Wassiliadis et al. [25] showed that different cell temperatures resulted from different cell contacts. Therefore, in our work, each cell was connected by resistance spot welding to minimize

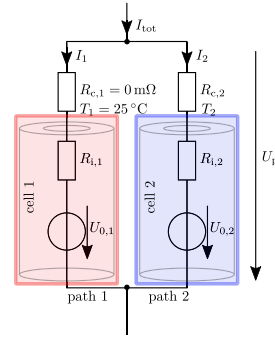


Fig. 1. Simplified ECM of a 2p battery connection. The voltage sources $U_{0,1}$ and $U_{0,2}$, and the internal resistances $R_{i,1}$ and $R_{i,2}$ represent the cells. T_1 and T_2 represent possible temperature inhomogeneities between the two cells. Additionally, the contact resistances, $R_{c,1}$ and $R_{c,2}$, stand for any additional potential drop due to contacting, wiring and measurement equipment.

the effects of this parameter on cell temperature. According to Brand et al. [26] the contact resistance of this connection method is less than 0.2 mΩ. The contacts for the 4-wire measurement technique were welded individually at both poles.

2.3. Measurement matrix

Fig. 1 shows a simple ECM of a 2p battery connection, which represents the system under investigation. The variables $R_{c,1}$ and $R_{c,2}$ stand for any additional potential drop due to contacting, wiring, and measurement equipment, $R_{i,1}$ and $R_{i,2}$ represent the internal resistance, T_1 and T_2 indicate the ambient temperature of the cells.

To investigate the strengths and challenges of the three cell technologies under investigation, the influence of inhomogeneous contact resistance, cell temperature, and the C-rate was evaluated. In the first study, inhomogeneous additional contact resistances were applied. $R_{c,1}$ remained fixed at 0 mΩ, while $R_{c,2}$ was varied. 25 mΩ was chosen as the upper limit as it corresponds roughly to the R_{AC} of the cells under study. In this range, $R_{c,2}$ was incremented in five steps, namely 0, 1, 5, 10, and 25 mΩ. All five resistance variations were tested at a C-rate of 0.5 C. At 0 mΩ, further C-rates of 0.25 C and 1.0 C were utilized. Both cells were cycled at a temperature of 25 °C. **Table 2** summarizes all parameter tuples concerning the resistance and C-rate variation.

Contact resistances of different contacting methods, e.g., welding, press, soldering, and conductive adhesive, exhibit resistances in the order of 0.1 to 0.3 mΩ per contact for a 18 650 cell [27]. In this context,

P. Jocher et al.

Journal of Energy Storage 98 (2024) 112931

Table 2
Test matrix to investigate the influence of inhomogeneous contact resistance on 2p battery cells. The resistance $R_{c,1}$ remained fixed at 0 mΩ. All measurements are carried out at 25 °C. All measured parameter combinations are denoted by "x".

$R_{c,2}$	C-rate		
	0.25	0.5	1
0 mΩ	x	x	x
1 mΩ		x	
5 mΩ		x	
10 mΩ		x	
25 mΩ		x	

Table 3
Test matrix to investigate the influence of inhomogeneous cell temperatures for various charge and discharge rates on 2p battery cells. Both, $R_{c,1}$ and $R_{c,2}$ were held at 0 mΩ.

T_1	T_2	$T_2 - T_1$
25 °C	15 °C	-10 °C
25 °C	20 °C	-5 °C
25 °C	25 °C	0 °C
25 °C	26 °C	1 °C
25 °C	27 °C	2 °C
25 °C	30 °C	5 °C
25 °C	35 °C	10 °C

the additional contact resistances examined in our study significantly exceed those of typical cell contacts [26].

Nevertheless, for the sensitivity study, contact resistances from 0 Ω to the AC resistance, R_{AC} , were selected. A doubling of the internal resistance is often defined as an end-of-life criterion [28].

The second study evaluated the influence of temperature gradients on the current distribution. In a similar manner to the inhomogeneous resistance study, the temperature T_1 was kept at 25 °C while the temperature T_2 was varied between 15 °C and 35 °C. T_2 was varied in seven steps. Two steps below T_1 , namely 15 and 20 °C, and five steps $T_2 \geq T_1$, namely 25, 26, 27, 30 and 35 °C were chosen. Two climate chambers established distinct temperature conditions for each of the 2p connected cells. The climate chambers showed a measurement uncertainty below 0.1 K. The test matrix to investigate the influence of inhomogeneous cell temperatures can be found in Table 3.

2.4. Inhomogeneity determination

Several parameters can be defined to quantify the current inhomogeneity of parallel connected cells. Particularly, current maxima can exceed the maximum allowed cell currents, giving rise to significant aging and safety implications [29]. The maximum current of cell x is obtained from the measured current distributions using Eq. (3). Here, in order to allow the comparison between different cell technologies and different C-rates, the current distribution of each cell is normalized to the average cell current I_{mean} . In this study, the maximum current of a particular cell is related to the average current,

$$i_{max,x} = \max\left(\frac{I_x}{I_{mean}}\right) - 1. \quad (3)$$

with

$$I_{mean} = \frac{I_{tot}}{2}. \quad (4)$$

The SoC difference between parallel connected cells indicates an inhomogeneous state of charge in the battery pack. To quantify these differences, the terms SoC_{system} and the individual SoC_x of the cells will be used. The SoC is defined as follows: Each study cycle corresponds to a CCCV charge and CCCV discharge to the respective voltage limits. The cut-off current of the CV is equivalent to C/10. After these processes were complete, it was assumed that the system was fully charged, $SoC_{system} = 100\%$, or discharged, $SoC_{system} = 0\%$. The SoC_x of the

individual cells is obtained based on the accumulated CCCV capacity of cell x as given in

$$SoC_x(t) = \frac{\int_{t_0}^t I_x(\tau) d\tau}{\int_{t_0}^{t_1} I_x(\tau) d\tau}. \quad (5)$$

With t_0 as start time and $SoC = 0\%$ and t_1 as end time and $SoC = 100\%$, of the corresponding CCCV charge. Similarly, the SoC_{system} is computed as

$$SoC_{system}(t) = \frac{\int_{t_0}^t (I_1(\tau) + I_2(\tau)) d\tau}{\int_{t_0}^{t_1} (I_1(\tau) + I_2(\tau)) d\tau}. \quad (6)$$

The SoC difference between the cells, can be used to characterize the inhomogeneity between the individual cells,

$$\Delta SoC = SoC_1 - SoC_2. \quad (7)$$

The maximum difference, $\max(\Delta SoC)$, is taken as an assessment parameter for the characterization of inhomogeneity. It is calculated as the value where the absolute difference between SoC_1 and SoC_2 is maximal.

The sensitivity factor introduces a further step to characterize inhomogeneity. As demonstrated in our previous work [17], local minima and maxima of the current distribution are allocated linearly according to the contact resistance. In this work, we extend this linear relationship for C-rate and temperature. The sensitivity factor is computed as the slope b of the linear fit of the characteristic parameter y over the variation x of C-rate, contact resistance or temperature,

$$y = b \cdot x. \quad (8)$$

The sensitivity factors quantify how much the inhomogeneity parameters $i_{max,x}$ and the maximum SoC difference, are affected by variations in contact resistance and unequal cell temperature. High sensitivity factor values suggest that the current distribution of cells in 2p configuration is likely to diverge significantly.

To quantify the influence of aging during the study of the cells, capacity and pulse resistance were measured regularly throughout the experimental period. During the experiment, all cells have undergone fewer than 100 Equivalent Full Cycles (EFCs) at C/2 and 25 °C. The LIB_{NCA} exhibits the highest overall capacity fade of approximately 5% in comparison to a fade of 2% for the LIB_{LFP} and an increase of 0.5% for the SIB. The more pronounced aging of the LIB_{NCA} can be attributed to the silicon content within the LIB_{NCA}'s anode, resulting in a capacity decrease during the initial cycles of the cell's life [30]. However, since the different studies were conducted sequentially, the capacity decrease within each study remained below 2% for all cell types. For further analysis and discussion, it will be assumed that aging did not influence the measurement results significantly and can be neglected.

3. Results and discussion

In this section, the results of the studies are presented and discussed. Two SoC ranges were considered: a boundary range and a middle SoC range. In real applications, cells typically operate in the middle SoC range [31]. Additionally, fast charging strategies focus on SoC ranges between 10 and 80% [32]. Consequently, the results presented in this chapter are confined to the 10 to 80% SoC_{system} range in charge direction. The analysis covering the full SoC spectrum can be found in Appendix C. The discharge phase is also plotted in Appendix D.

3.1. Influence of inhomogeneous contact resistance

Fig. 2 shows the impact of an increased contact resistance, $R_{c,2}$. The normalized current distribution and the SoC difference between the cells, SoC_1 - SoC_2 , is shown for each of the three cell technologies. Additionally, the voltage profiles, U_p , of the investigated cells, as measured during the 0.5 C CC charging process are plotted. To highlight variations within the examined SoC range, the y -axis of Subfigure (b)

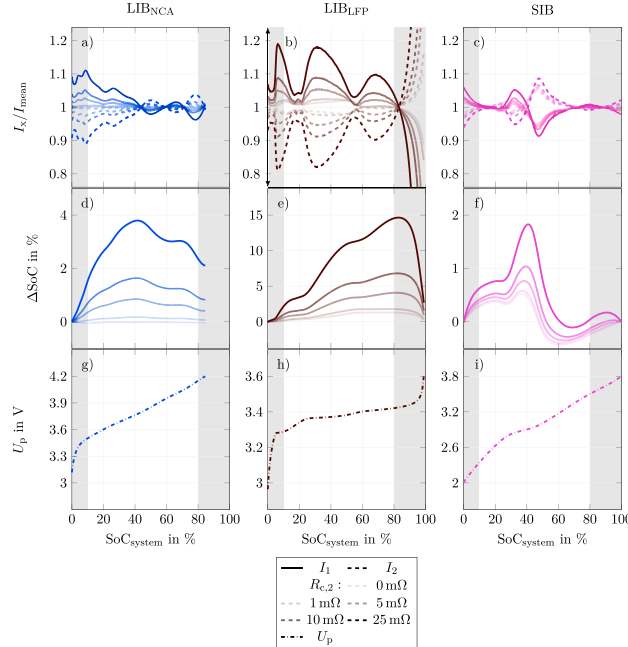


Fig. 2. Current distribution between 2p cells during CC charging at 0.5C and inhomogeneous contact resistance. The resistance, $R_{c,2}$, was varied from 0 to 25 mΩ and LIB_{NCA}, LIB_{LFP} and SIB cells are analyzed. The x-axis is the same over all subfigures and represents the SoC_{system}. The gray areas represent low SoC_{system} < 10% and high SoC_{system} > 80%. Subfigures (a), (b) and (c) show the resulting current distribution with the same y-axis for both cells, $x \in \{1, 2\}$. The corresponding data with the full y-axis is plotted in Fig. C.2. Subfigures (d), (e) and (f) show the resulting SoC difference between the 2p-connected battery cells. The resulting voltage U_p at $R_{c,2} = 0$ mΩ is plotted in the Subfigures (g), (h) and (i).

is slightly cropped. In all cases, an increased inhomogeneity between the two parallel cells can be seen with a rising difference in the contact resistance.

Of the investigated cell technologies, the LIB_{LFP} possesses the most prominent current inhomogeneity. The current of path 1 is consistently higher than the current of path 2 for all contact resistances. At the highest investigated additional contact resistance of 25 mΩ, this leads to a peak SoC difference of 15%. Large current peaks occur for the cell without the additional contact resistance, see I_1 in Fig. 2, reaching about 1.18 times the I_{mean} current in the investigated SoC_{system} range. Over the full range of SoC_{system}, a maximum current of 1.8 times the I_{mean} current for the cell with the contact resistance is observed. This can be seen in Fig. C.2 can be particularly challenging in real applications, where such large currents may cause irreversible damage to the cells.

In comparison to LIB_{LFP}, the LIB_{NCA} and SIB cells show a more homogeneous current distribution. Additionally, the current load of path 1 is not continuously higher than that of path 2. Multiple intersections of the current curves occur in the SoC_{system} range between 10 to 80%. This results in a smaller maximum SoC difference for the LIB_{NCA} and SIB cells, which remains below 4% and 2%, respectively, even for a contact resistance in the order of $R_{AC} = 25$ mΩ. An explanation for this can be provided by considering U_p in Subfigures (g) (h) and (i) in Fig. 2, which show a steeper curve throughout the charging process for LIB_{NCA} and SIB cells. According to the findings of Hust [33], deviations in resistance between parallel cells predominantly influence the current distribution in flat OCV segments. Consequently, the most substantial deviations are observed for the LIB_{LFP} cell, which, particularly within

the examined SoC_{system} range, demonstrates a notably flat OCV, see Fig. 2(h). The most significant current deviations coincide with the segments of the OCV where almost no change in the voltage is present. If the entire CC phase is considered, the SoC differences of LIB_{LFP} and SIB both even out to almost zero in the end. In the case of LIB_{NCA}, however, SoC differences do not even out before reaching the CV phase.

A more detailed insight into this relationship is provided in Fig. 3, where the corresponding Differential Voltage Analysis (DVA) of U_p and the SoC difference between the cells for the case $R_{c,2} = 25$ mΩ are plotted against the cell voltage. Similar to Fig. 2, the gray areas represent the SoC_{system} ranges below 10% and above 80%. It is evident that for all three investigated cell technologies, the global minima of the DVA, and hence, regions with the least change in OCV, correspond to the fastest divergence of the SoC between the two cells. LIB_{LFP} exhibits the smallest differential potential, leading to the most inhomogeneous SoC. For LIB_{NCA} and SIB, larger differential potentials are prominent, with segments where the effect of the contact resistance on current distribution is dominated by OCV, resulting in a convergence of the cell SoC_x. The R_{DC} is an additional factor in how the imposed contact resistance affects current distribution and consequently the SoC difference. The impact becomes apparent when comparing the trends of LIB_{NCA} and SIB in Fig. 3. Due to LIB_{NCA} displaying differential potential values generally greater or equal to those of SIB, its SoC is expected to be less affected by contact resistance. Nevertheless, the maximum SoC difference is approximately twice as large as in the case of SIB. As listed in Table 1, LIB_{NCA} exhibits the lowest R_{DC}/R_{AC} at approximately 1.83, followed by LIB_{LFP} and SIB with ratios of approximately 2.13 and 3.35, respectively. Hence, the R_{DC} defines the influence of contact resistances

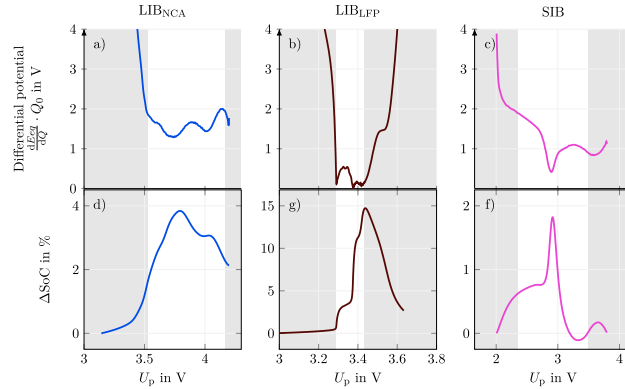


Fig. 3. Differential Voltage Analysis (DVA) (a–c) during CC charge with 0.5 C. Subfigures (d), (e) and (f) correspond to the SoC cell to cell difference regarding the additional contact resistance $R_{c,2} = 25 \text{ m}\Omega$. A large SoC difference between the cells corresponds to a small slope of the OCV. The gray areas represent low $\text{SoC}_{\text{system}} < 10\%$ and high $\text{SoC}_{\text{system}} > 80\%$.

on the current distribution. Additionally, due to the 2.7 times higher capacity of the LIB_{NCA} cell, a higher absolute current occurs, and thus, as a first approximation, a higher overvoltage than the SIB cell results. As a result, larger SoC differences can be achieved between the cells. Consequently, for LIB_{NCA}, the cell with the lowest R_{DC} , the presence of contact resistance leads to a more significant imbalance in the total resistance between paths compared to SIB.

The effect of increasingly inhomogeneous contact resistance on the maximum path currents of both parallel connected cells and the maximum SoC difference can be more closely examined by analyzing it within Fig. 4. The maximum normalized currents, as defined in Eq. (3), are plotted over the additional resistance $R_{c,2}/R_{AC}$. An approximately linear correlation of the current maxima is observed across all studied cell technologies. Notably, LIB_{LFP} demonstrates the most pronounced maximum current and the most significant dependence on the balance between contact resistances. Apart from this, qualitative distinctions can be observed in the patterns of the individual cells in Subfigures (a), (b), and (c) in Fig. 4. While for LIB_{NCA} and SIB the maximum currents in both cells increase along with the imbalances in contact resistance, in the case of LIB_{LFP}, the maximum current through cell 2 decreases as its contact resistance increases. Moreover, the current maxima of cell 2 consistently remain below 1, offering a direct explanation for the markedly higher SoC inhomogeneity observed in the case of LIB_{LFP}.

When comparing LIB_{NCA} and SIB cells, we observe that both cell types increase the maximum current level by adding resistance. However, as the resistance $R_{c,2}$ increases, the LIB_{NCA} cell without additional contact resistance shows a more rapid increase in maximum current. Every cell pair displays a noticeable difference in their maximum currents, even when $R_{c,2} = 0 \text{ m}\Omega$, likely due to internal variations between individual SIB cells. This difference in maximum currents persists as $R_{c,2}$ increases.

In every instance, the inhomogeneous current distribution induces unequal charging patterns in the two parallel connected cells, causing an uneven SoC development during the charging process, as depicted in Fig. 2(d), (e), and (f). The resulting maximum SoC differences between the cells due to the rising contact resistance of cell 2 within the range of 10% to 80% $\text{SoC}_{\text{system}}$ are presented in Fig. 4(d), (e) and (f). A linear relationship between maximum SoC imbalance and increasingly inhomogeneous contact resistance is observed in all cells under study. Similarly to the pronounced increase in current maxima, there is a notably stronger divergence in SoC between the cells for LIB_{LFP} compared to all other technologies. The maximum SoC difference between the cells reaches approximately 15% for an additional contact resistance of

$R_{c,2} = 25 \text{ m}\Omega$. Conversely, the other technologies exhibit significantly lower SoC drifts, with LIB_{NCA} reaching 4% and SIB reaching 2% despite the same contact resistance imbalance. The results over the full SoC range are plotted in Appendix C and the corresponding discharge phase in Fig. D.7.

3.2. Influence of inhomogeneous cell temperature

A variation in the cell's temperature leads to alterations in its electrical parameters, particularly affecting the R_{DC} resistance [34]. The decrease of resistance with increasing temperatures can be described using the Arrhenius relation [34–37]. Therefore, for all investigated cell technologies, the influence of temperature on the R_{DC} resistance was measured. Fig. A.1 illustrates the resulting DC resistance between 15 and 35 °C. Each cell technology displays distinct temperature sensitivities. Of the three technologies studied, the greatest sensitivity of R_{DC} to temperature changes was displayed by SIB due to an activation energy barrier almost 3 times greater than the other cells. This was determined by fitting an Arrhenius-like equation to the resistance over the temperature curve, see Fig. A.1.

Fig. 5 illustrates how variations in cell temperature, ranging from a temperature difference of –10 K to 10 K between cell 2 and cell 1, impact the current distribution throughout a charging process conducted at a constant current rate of 0.5 C. In all measurements, the temperature of cell 1 was maintained at 25 °C. Subfigures (a), (b), and (c) depict the normalized current distribution of cell 2, while Subfigures (d), (e), and (f) represent the SoC differences of cell 1 relative to cell 2. To better highlight the variations within the examined SoC range, the y-axis of Subfigures (b) and (c) are slightly cropped. To differentiate between behaviors at cold and hot temperature inhomogeneities, only the current distributions for path 2 are presented. Due to the 2p configuration, cell 1 exhibits symmetrical behavior to cell 2. Additionally, the plot with the full y-axis is provided in Fig. C.3. The corresponding discharge phase is plotted in Fig. D.8.

Among all investigated cell technologies, increasing differences between the cell temperatures of the parallel connected cells result in a progressively asymmetrical evolution of the currents, which correspondingly affects the SoC of the individual cells. The LIB_{NCA} displays the smallest changes in current distribution as temperature imbalance increases, resulting in a maximum SoC difference of 2% between the two parallel connected cells. In contrast, the LIB_{LFP} and SIB cells demonstrate a more pronounced sensitivity to inhomogeneous cell temperatures. This can be directly attributed to the stronger temperature

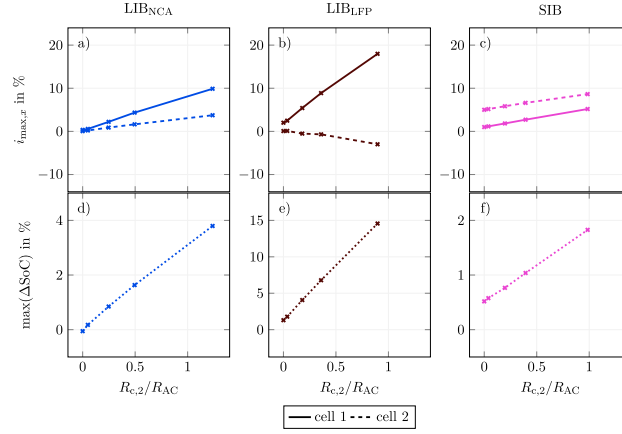


Fig. 4. Maxima of the evaluated inhomogeneity parameters in the presence of inhomogeneous contact resistance between 10 to 80% SoC_{system} . Subfigures (a), (b) and (c) represent the maximum current and (d), (e) and (f) maximum SoC differences between both cells, $x \in 1,2$. All data show a linear behavior regarding the additional contact resistance $R_{c,2}$. Please be aware that the y-axis of Subfigure (d), (e) and (f) is different. The full SoC range is plotted in Fig. C.4.

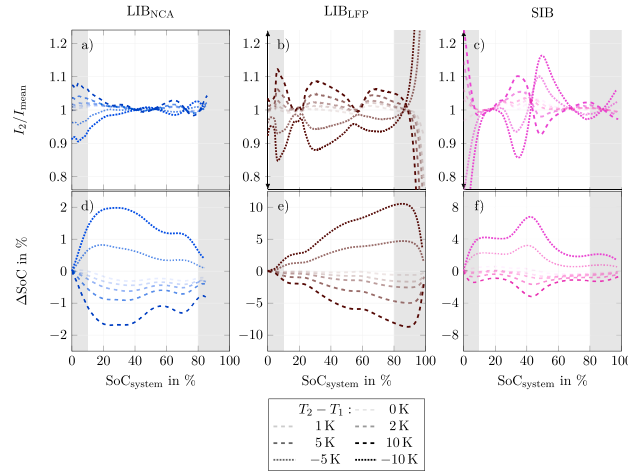


Fig. 5. Current distribution between 2p cells during CC charging at 0.5C and inhomogeneous cell temperature. Cell 1 was kept at $T_1 = 25^\circ C$, the temperature of cell 2 (T_2) was varied in the range $25^\circ C \pm 10 K$, and LIBNCA, LIBLFP and SIB cells are analyzed. The x-axis is the same over all subfigures and represents the SoC_{system} . The gray areas represent the edge areas of the SoCs, from 0 to 10% SoC_{system} , as well as from 80 to 100% SoC_{system} . Subfigures (a), (b) and (c) show the resulting current I_2 on the same y-axis scale for all investigated cells. The corresponding full y-axis range is plotted in Fig. C.3. Subfigures (d), (e) and (f) show the resulting SoC spread between the 2p-connected cell pairs.

dependency of the R_{DC} resistance in the case of the SIB cells, as shown in Fig. A.1. Although R_{DC} of the LIBLFP cells is markedly less dependent on temperature than SIB, it is still significantly affected by the plateaus in OCV discussed above. The results show that temperature variations increase inhomogeneity in LIBLFP less than path resistance variations, while the opposite is true for SIB.

The SIB cells demonstrate the most fluctuating current distribution and the highest current peaks, whereas the LIBLFP cells display the most one-sided current distribution within the investigated SoC range due to their flat OCV. As a result, the LIBLFP cells show the largest SoC difference, reaching up to 10% in the examined SoC_{system} range from 10 to 80%. Further quantitative insights can be obtained from Fig. 6,

where the evolution of the maximum current and the maximum SoC difference between the two parallel cells is plotted against the imposed cell temperature difference $T_2 - T_1$.

The Arrhenius relationship is directly reflected in the trends of the two parameters across all the examined cell technologies. First, lowering the temperature of cell 2 has a more significant impact on the maximum current of both cells than raising it. This is due to the exponential increase in resistance with decreasing temperature, leading to a more pronounced resistance imbalance between the two cells when T_2 is reduced. Second, the most significant alterations in the maximum current are observed in the case of the SIB cells. This phenomenon

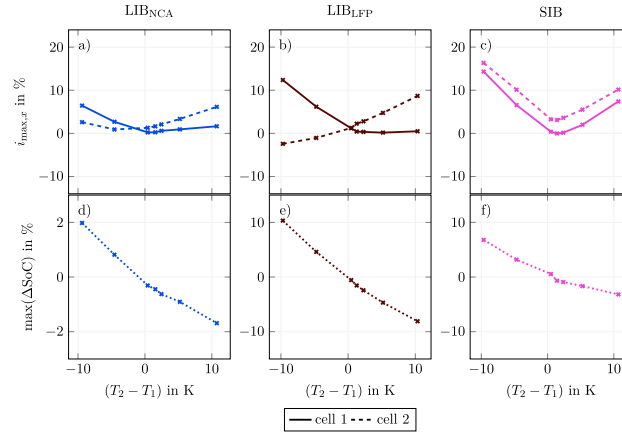


Fig. 6. Maxima of the evaluated inhomogeneity parameters in the presence of inhomogeneous cell temperature between 10 to 80% SoC_{system}. Subfigures (a), (b) and (c) represent the maximum current and (d), (e) and (f) the maximum SoC differences between both cells, $x \in 1,2$. Please be aware that the y-axis of Subfigures (d), (e) and (f) is different. The full SoC range is plotted in Fig. C.5.

can be attributed to the greater temperature dependency of their R_{DC} resistance values.

The most significant SoC difference occurs for the LIB_{LFP} cells, as was the case in the study of inhomogeneous contact resistance. The cause lies in the one-sided current curve, where the warmer cell almost continuously takes on the higher load. In the case of $T_2 - T_1 = 10$ K, the consistently higher current in the warmer cell results in the strongest SoC difference between the cells.

In Fig. 6 it is possible to observe that the SIB does not exhibit an intersection point of the current maxima at $T_1 - T_2 = 0$, while this occurs in the LIB_{LFP} and LIB_{NCA} cells. This can be traced back to the current reversal following the crossing points of the current distributions represented in Fig. 5. Here, the SIB cell exhibits a current reversal occurring after the crossing point at around 40 to 45% SoC. In contrast, LIB_{LFP} and LIB_{NCA} show a less pronounced current reversal with a more one-sided current distribution, in which one cell tendentially maintains a lower current throughout the entire charge between 10 and 80% SoC. Therefore, with increasing temperature difference, the maximum current of one LIB_{LFP} or LIB_{NCA} cell increases, while the maximum current of the other cell remains relatively moderate. On the other hand, for SIB both current maxima grow with rising absolute temperature difference.

3.3. Influence of C-rate

To investigate the impact of the current amplitude, tests at 0.25 C, 0.5 C, and 1 C have been carried out. In contrast to the investigations in which contact resistance and cell temperature were varied, varying the C-rate did not provoke a consistent trend across all three cell technologies. Nevertheless, the parameters studied in this work are less sensitive to the C-rate than to contact resistance or cell temperature difference. This is the case for all three cell technologies. An insensitivity to the C-rate has been observed for the LIB_{LFP}, as this parameter does not appear to affect the maximum current, $i_{max,x}$, in the cells. The LIB_{NCA} displays a trend in which the current maxima increases marginally in step with the C-rate. In contrast, as the C-rate increases, the SIB current maxima decreases. The corresponding current distribution is plotted in Fig. E.9.

Additionally, examining the three cell technologies demonstrates disparities in the durations of the CC phases. Both LIB_{LFP} and SIB exhibit insensitivity across all investigated C-rates, consistently obtaining a SoC_{system} at or above 95%. In contrast, the LIB_{NCA} SoC_{system} is

noticeably affected by changes in the C-rate. Due to overvoltages, it is CC chargeable to SoC_{system} = 95% at C-rates of 0.25 C. However, an increase in the C-rate to 1 C leads to a significant decrease in the achievable SoC_{system}, with only 75% achievable during the CC phase. The same behavior is also visible in 1p configuration.

3.4. Sensitivity factor

As illustrated in Figs. 4 and 6, within the SoC_{system} range of 10 to 80% the maximum path currents and the SoC difference display a linear development in the presence of a progressively inhomogeneous contact resistance and positive cell temperatures, $T_2 \geq T_1$. To enable a sensitivity analysis of both studies, the slopes of the maximum path currents, the peak SoC difference among the cells, and the SoC difference at SoC_{system} = 80% are evaluated. This enables the sensitivity of these parameters to the test conditions to be quantified. Table B.4 shows the Pearson coefficient as a measure for linear correlation between two data sets. Fig. 7(a) represents the sensitivity factor of $R_{c,2}$ computed from the parameters given in Fig. 4 in %/ R_{AC} . Fig. 7(b) represents the sensitivity factor over the increase in temperature, $T_2 \geq T_1$, based on Fig. 6 in %/K. The sensitivity regarding the slope parameter evaluated over the full SoC spectra is plotted in Fig. C.6.

The analysis of the slopes facilitates a quantitative comparison of the cell technologies under investigation, while also providing a measurable demonstration of their respective strengths and challenges. Based on the steep OCV and the high R_{DC} to R_{AC} ratio, the SIB shows the lowest sensitivity to the inhomogeneous contact resistance. In contrast, the prominent Arrhenius relationship gives the same technology a strong sensitivity to temperature differences significantly affecting current distribution between the cells. Due to the flat OCV of the LIB_{LFP} cell, inhomogeneities in both contact resistance and cell temperature lead to the larger and more frequent deviations in the current distribution and the SoC than are seen for the other cells.

4. Conclusion

This paper analyzes the challenges and strengths of three different cell technologies (LIB_{NCA}, LIB_{LFP} and SIB) when scaling from a single cell to a system of two cells in parallel.

To investigate inhomogeneous contact resistance, an additional resistance on path 2 of up to $R_{c,2} = 25$ mΩ, which corresponds roughly

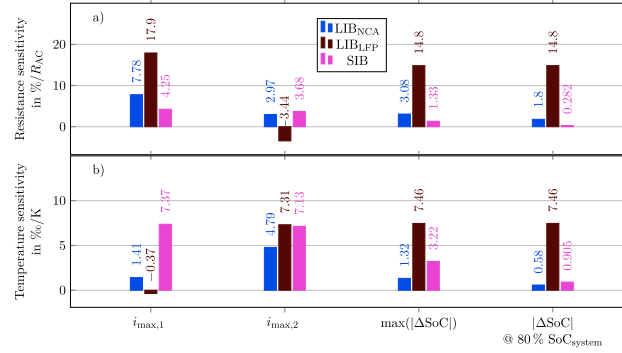


Fig. 7. Sensitivity factor during investigation of inhomogeneous contact resistance and cell temperature between 10 and 80% SoC_{system}. Quantitative comparison between the investigated sensitivity factors, i_{max} , and ΔSoC , between the cells for (a) resistance and (b) temperature. The positive temperature differences, $T_2 \geq T_1$, are considered.

to the AC resistance R_{AC} , was added. We find, that to achieve a current distribution as homogeneous as possible, the OCV should have a high slope and the cell should have a contact resistance relatively small compared to R_{DC} . For the examined LIB_{LFP} cells, SoC differences between the cells of up to 15% and current differences of up to 1.8 times the mean current were identified when considering entire SoC_{system} range. This can be particularly challenging in real applications, where such large currents may cause irreversible harm to the cells. In the SoC range between 10 and 80% SoC the LIB_{LFP} cells show the highest current inhomogeneity with deviations from the mean of up to 18%, whereas LIB_{NCA} and SIB display maximum deviations from the mean of around 10%. For all contact resistance inhomogeneities, at 80% SoC_{system} the SIB cells demonstrated a SoC difference of less than 2%, the lowest of all technologies studied.

In contrast, inhomogeneous cell temperatures provoke the largest inhomogeneity in the current in SIB cells between 10 to 80% SoC_{system}. When subjected to inhomogeneous path temperatures in the range of $(25 \pm 10)^\circ C$ disparities from the mean of up to 17% were displayed by the SIB cell technology. In this case, the Arrhenius dependency of the cell resistance was shown to explain the influence of temperature differences. It was additionally observed, that under inhomogeneous temperature conditions, a flat OCV, as found in LIB_{LFP} cells, results in an inhomogeneous current distribution.

The maximum currents of both paths and the resulting SoC difference between the cells were investigated and to quantify the inhomogeneity, sensitivity factors were introduced. As all investigated parameters showed a linear relationship, the slope was used to quantify the resulting sensitivity factor. Fig. 8 summarizes the results and shows a comparison between 10 to 80% SoC_{system} of both, (a) inhomogeneous contact resistance and (b) cell temperature. The data corresponds to an inhomogeneous contact resistance in the order of $R_{c,2} = 20\% \cdot R_{AC}$ and a temperature difference, $T_2 - T_1$, of 5 K. The numbers represent the inhomogeneity in %. Zero represents an equal behavior between the two cells, while a negative value indicates that one cell experiences a current lower than the mean current, I_{mean} . Consequently, a large area corresponds to a small sensitivity and signifies that the battery is more capable of operating under inhomogeneous conditions. Both LIB_{NCA} and SIB show a similar qualitative sensitivity towards resistance inhomogeneities, while quantitatively the SIB cell exhibits slightly better sensitivity. LIB_{LFP} exhibits the greatest sensitivity to the factors studied, which is represented by the smallest area in both diagrams. Fig. 8(b) shows clearly, that LIB_{NCA} is the least sensitive of the technologies to unequal cell temperatures. SIB lies between the two other examined cell technologies due to its highly temperature-sensitive resistance.

Finally, the sensitivity factors of different state-of-the-art technologies are analyzed. The cell technologies under investigation exhibit significant performance disparities in response to increased temperature and resistance imbalances while being charged in parallel configurations. The SIB shows the smallest sensitivity to inhomogeneous contact resistance. In contrast, due to its flat OCV the LIB_{LFP} cell shows a large sensitivity to both inhomogeneous contact resistance and cell temperature. Compared with the aforementioned cell technologies, LIB_{NCA} shows a lower overall sensitivity to both path resistance and temperature imbalances. These may be used as a guideline for battery applications. Especially for LIB_{LFP} undergoing complete charging phases, large current inhomogeneities must be mitigated when designing charging strategies. The one-sided current distribution leads to the largest SoC difference seen in this study. For SIB cell technology temperature inhomogeneities should be considered as they have the most significant influence on maximum currents in the 10 to 80% SoC_{system} range and strongest R_{DC} to temperature behavior.

In summary, significant impacts on current distribution can occur in all the cell technologies studied in this work. These may be caused by the intrinsic development of their OCVs, or due to imbalances in cell resistance or temperature.

The results of this work provoke new research questions. One of the most prominent is the influence of inhomogeneous contact resistance and cell temperature when scaling from 2p to μp . Also of interest is the development of aging and the influence of disparities in the SoH on the current distribution between parallel connected cells.

CRedit authorship contribution statement

P. Jocher: Writing – review & editing, Writing – original draft, Validation, Methodology, Formal analysis, Data curation, Conceptualization. F. Roehrer: Writing – review & editing, Writing – original draft, Methodology, Investigation. M. Rehm: Writing – review & editing, Methodology, Investigation. T. Idriizi: Writing – review & editing, Data curation. A. Himmelreich: Writing – review & editing, Data curation. A. Jossen: Writing – review & editing, Supervision, Project administration, Funding acquisition.

Declaration of competing interest

The authors declare that they have no known competing financial interests or personal relationships that could have appeared to influence the work reported in this paper.

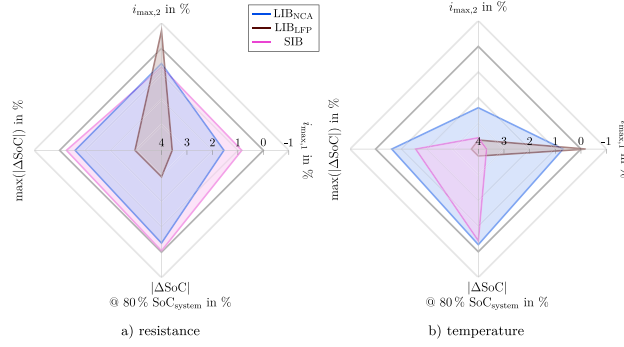


Fig. 8. Comparison between the sensitivity factors, $i_{max,2}$, $\max(|\Delta\text{SoC}|)$ and $|\Delta\text{SoC}|$ at $\text{SoC}_{system} = 80\%$. Subfigure (a) represents an inhomogeneous contact resistance in the order of $R_{c,2} = 20\% \cdot R_{AC}$ and (b) a temperature difference, $T_2 - T_1$, of 5 K with $T_1 = 25^\circ\text{C}$. The numbers represent the inhomogeneity of each sensitivity factor in %. Consequently, a large area corresponds to a small sensitivity. The SoC range between 10 to 80% is considered and is based on Fig. 7.

Table B.4

Pearson correlation coefficients of the investigated parameters. The row R refers to the investigation of contact resistance and the relationships shown for cell 2 in Fig. 4. Row T refers cell two and the relationships shown in Fig. 6, for which $T_2 \geq T_1$. The SoC_{system} range between 10 to 80% is considered. The Pearson correlation coefficient quantifies the strength and direction of the linear relationship between the parameters and the investigated inhomogeneity increase, ranging from 1 (perfect positive correlation) to -1 (perfect negative correlation), with 0 indicating no linear correlation.

Parameter	$i_{max,1}$			$i_{max,2}$			$\max(\Delta\text{SoC})$			$\Delta\text{SoC} @ 80\% \text{ SoC}$			
	Matrix	NCA	LFP	SIB	NCA	LFP	SIB	NCA	LFP	SIB	NCA	LFP	SIB
R		0.9995	0.9993	0.9999	0.9994	-0.9879	0.9990	0.9992	0.9999	0.9999	1.0000	0.9999	0.9992
T		0.9908	-0.3819	0.9681	0.9987	0.9986	0.9872	-0.9985	-0.9968	-0.9617	-0.9925	-0.9968	-0.9920

Data availability

Data will be made available on request.

Declaration of Generative AI and AI-assisted technologies in the writing process

During the preparation of this work the authors used Grammarly and ChatGPT for individual sections in order to improve language and readability. After using this tool, the authors reviewed and edited the content as needed and take full responsibility for the content of the publication.

Acknowledgments

This research was funded by the German Federal Ministry of Education and Research (BMBF) via the OSLiB research project (grant number 03X90330 A) and Federal Ministry for Economic Affairs and Climate Action (BMWK), Germany via the ProMoBiS research project (grant number 03ETE046 F).

Appendix A. Cell parameter

See Fig. A.1.

Appendix B. Linear correlation coefficient of the investigated parameters

See Table B.4.

Appendix C. Analysis of full SoC range — charge direction

See Figs. C.2–C.6.

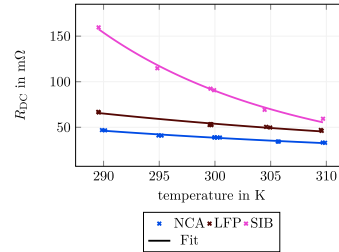


Fig. A.1. Measured R_{DC} evaluated after 10 s over the temperature for all investigated cells. An Arrhenius fit of the form $R_{DC}(T) = R_0 \exp(\frac{E_a}{k_B T})$ can be employed to model the relationship between resistance and temperature [38]. Here, R_0 is a pre-exponential factor, E_a denotes the activation energy barrier and k_B the Boltzmann constant. The resulting energy barrier of the LIB_{NCA} and LIB_{LFP} are (0.1362 ± 0.0144) eV and (0.1405 ± 0.0144) eV respectively, whereas the SIB's barrier is approximately (0.40 ± 0.02) eV.

Appendix D. Analysis of full SoC range — discharge direction

See Figs. D.7 and D.8.

Appendix E. Analysis of C-rate

See Fig. E.9.

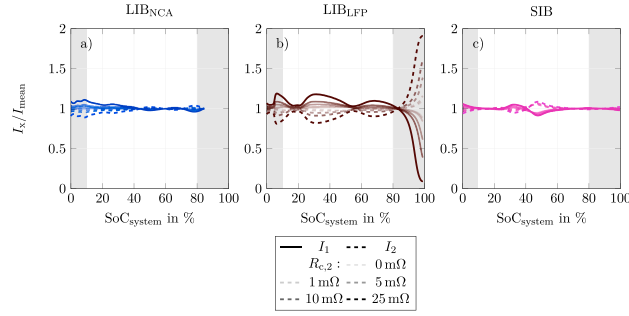


Fig. C.2. Current distribution between 2p parallel connected cells during CC charging at 0.5C during investigation of inhomogeneous contact resistance over the full SoC_{system} range. LIB_{NCA}, LIB_{LFP} and SIB cells are analyzed. The resistance, $R_{c,2}$, was varied from 0 to 25 mΩ.

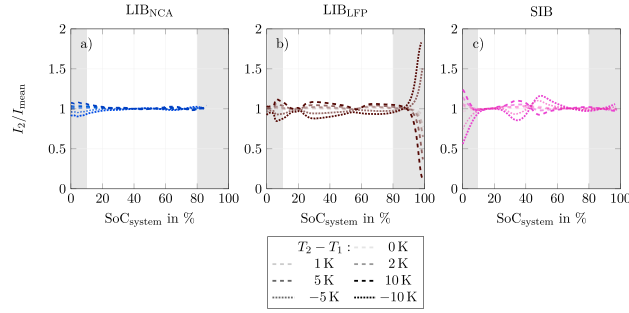


Fig. C.3. Current distribution between 2p parallel connected cells during CC charging at 0.5C during investigation of inhomogeneous cell temperature over the full SoC_{system} range. LIB_{NCA}, LIB_{LFP} and SIB cells are analyzed. Temperature T_2 was varied by a maximum of ± 10 K in relation to the temperature $T_1 = 25^\circ\text{C}$.

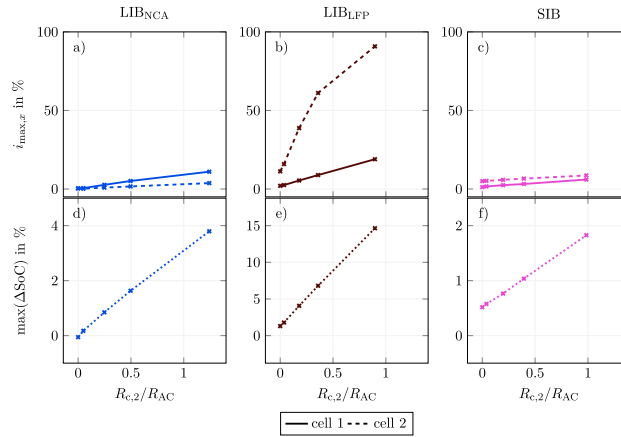


Fig. C.4. Maxima of the evaluated inhomogeneity parameters measured while investigating inhomogeneous contact resistances over the full SoC_{system} range. The current, i_{max} and the SoC, difference between the cells are analyzed, $x \in 1, 2$. Please be aware that the y-axis of Subfigure (d), (e) and (f) is different.

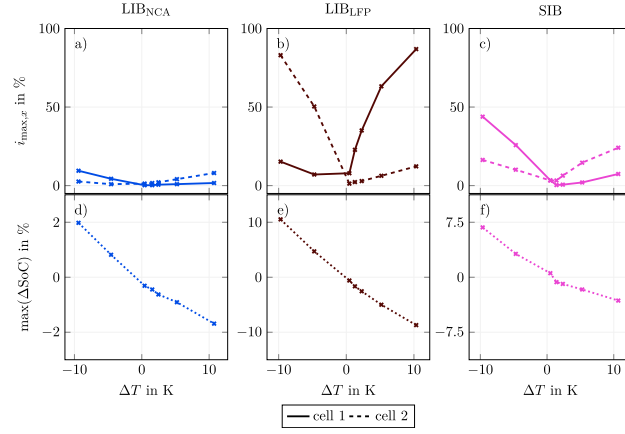


Fig. C.5. Maxima of the evaluated inhomogeneity parameters measured while investigating inhomogeneous cell temperature over the full $\text{SoC}_{\text{system}}$ range. The current, $i_{\text{max},x}$ and the SoC_x difference between the cells are analyzed, $x \in \{1, 2\}$. Please be aware that the y-axis of Subfigure (d), (e) and (f) is different.

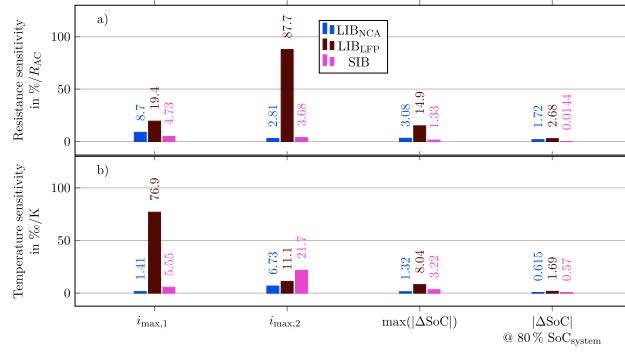


Fig. C.6. Sensitivity factors calculated for the investigations of inhomogeneous contact resistance and cell temperature over the full $\text{SoC}_{\text{system}}$ range. The positive temperature differences, $T_2 \geq T_1$, are considered.

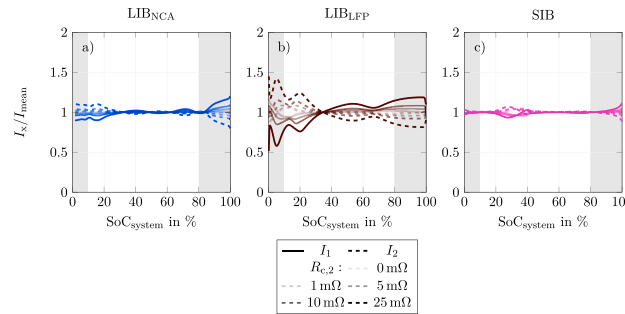


Fig. D.7. Analysis of the 2p discharge current distribution at 0.5C during investigation of inhomogeneous contact resistance over the full $\text{SoC}_{\text{system}}$ range. LIB_{NCA}, LIB_{LFP} and SIB cells are analyzed. The x-axis and y-axis are the same overall subfigures. The resistance, $R_{c,2}$, was varied from 0 to 25 mΩ. The discharge direction is from the right to the left.

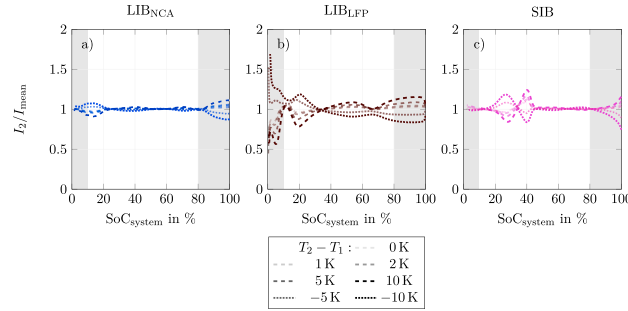


Fig. D.8. Current distribution between 2p discharge at 0.5C during investigation of inhomogeneous cell temperature over the full SoC_{system} range. LIB_{NCA}, LIB_{LFP} and SIB cells are analyzed. The x-axis and y-axis are the same overall subfigures. Temperature T_2 was varied ± 10 K in relation to the temperature T_1 was 25 °C. The discharge direction is from the right to the left.

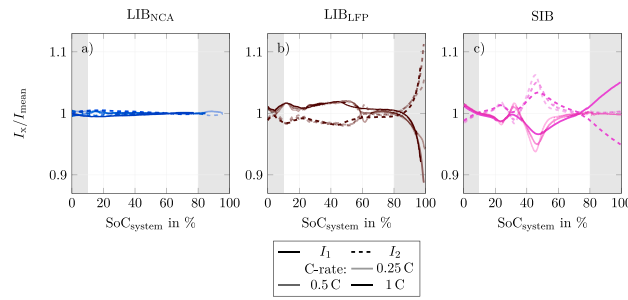


Fig. E.9. Current distribution between 2p charge at different C-rates over the full SoC_{system} range. LIB_{NCA}, LIB_{LFP} and SIB cells are analyzed. The x-axis and y-axis are the same overall subfigures.

References

[1] I. Zilberman, S. Ludwig, M. Schiller, A. Jossen, Online aging determination in lithium-ion battery module with forced temperature gradient, *J. Energy Storage* 28 (9) (2020) 101170, <http://dx.doi.org/10.1016/j.est.2019.101170>.

[2] M.M. Hoque, M.A. Hannan, A. Mohamed, A. Ayob, Battery charge equalization controller in electric vehicle applications: A review, *Renew. Sustain. Energy Rev.* 75 (8) (2017) 1363–1385, <http://dx.doi.org/10.1016/j.rser.2016.11.126>.

[3] M.J. Brand, M.H. Hofmann, M. Steinhardt, S.F. Schuster, A. Jossen, Current distribution within parallel-connected battery cells, *J. Power Sources* 334 (2016) 202–212, <http://dx.doi.org/10.1016/j.jpowsour.2016.10.010>.

[4] F. An, J. Huang, C. Wang, Z. Li, J. Zhang, S. Wang, P. Li, Cell sorting for parallel lithium-ion battery systems: Evaluation based on an electric circuit model, *J. Energy Storage* 6 (2016) 195–203, <http://dx.doi.org/10.1016/j.est.2016.04.007>.

[5] M. Baumann, L. Wildfeuer, S. Rohr, M. Lienkamp, Parameter variations within lithium-ion battery packs – theoretical investigations and experimental quantification, *J. Energy Storage* 18 (2018) 295–307, <http://dx.doi.org/10.1016/j.est.2018.04.031>.

[6] M. Dubarry, A. Devie, B.Y. Liaw, Cell-balancing currents in parallel strings of a battery system, *J. Power Sources* 321 (2016) 36–46, <http://dx.doi.org/10.1016/j.jpowsour.2016.04.125>.

[7] A. Fill, T. Schmidt, T. Mader, R. Llorente, A. Avdyli, B. Mulder, K.P. Birke, Influence of cell parameter differences and dynamic current stresses on the current distribution within parallel-connected lithium-ion cells, *J. Energy Storage* 32 (2020) 101929, <http://dx.doi.org/10.1016/j.est.2020.101929>.

[8] R. Gogoana, M.B. Pinson, M.Z. Bazant, S.E. Sarma, Internal resistance matching for parallel-connected lithium-ion cells and impacts on battery pack cycle life, *J. Power Sources* 252 (2014) 8–13, <http://dx.doi.org/10.1016/j.jpowsour.2013.11.101>.

[9] A. Fill, S. Koch, A. Pott, K.-P. Birke, Current distribution of parallel-connected cells in dependence of cell resistance, capacity and number of parallel cells, *J. Power Sources* 407 (1) (2018) 147–152, <http://dx.doi.org/10.1016/j.jpowsour.2018.10.061>.

[10] M. Schindler, P. Jocher, A. Durdal, A. Jossen, Analyzing the aging behavior of lithium-ion cells connected in parallel considering varying charging profiles and initial cell-to-cell variations, *J. Electrochem. Soc.* 168 (9) (2021) 090524, <http://dx.doi.org/10.1149/1945-7111/ac2089>.

[11] M. Schindler, A. Durdal, J. Sturm, P. Jocher, A. Jossen, On the impact of internal cross-linking and connection properties on the current distribution in lithium-ion battery modules, *J. Electrochem. Soc.* 167 (12) (2020) 120542, <http://dx.doi.org/10.1149/1945-7111/abad6b>.

[12] C. Pastor-Fernández, T. Bruen, W.D. Widanage, M.A. Gama-Valdez, J. Marco, A study of cell-to-cell interactions and degradation in parallel strings: Implications for the battery management system, *J. Power Sources* 329 (2016) 574–585, <http://dx.doi.org/10.1016/j.jpowsour.2016.07.121>.

[13] W. Shi, X. Hu, C. Jin, J. Jiang, Y. Zhang, T. Yip, Effects of imbalanced currents on large-format LiFePO₄/graphite batteries systems connected in parallel, *J. Power Sources* 313 (2016) 198–204, <http://dx.doi.org/10.1016/j.jpowsour.2016.02.087>.

[14] M. Naylor Marlow, J. Chen, B. Wu, Degradation in parallel-connected lithium-ion battery packs under thermal gradients, *Commun. Eng.* 3 (1) (2024) <http://dx.doi.org/10.1038/s44172-023-00153-5>.

[15] G.M. Cavalheiro, T. Iriyama, G.J. Nelson, S. Huang, G. Zhang, Effects of nonuniform temperature distribution on degradation of lithium-ion batteries, *J. Electrochem. Energy Convers. Storage* 17 (2) (2020) <http://dx.doi.org/10.1115/1.4045205>.

[16] M. Al-Amin, A. Barai, T.R. Ashwin, J. Marco, An insight to the degradation behaviour of the parallel connected lithium-ion battery cells, *Energies* 14 (16) (2021) 4716, <http://dx.doi.org/10.3390/en14164716>.

[17] P. Jocher, M. Steinhardt, S. Ludwig, M. Schindler, J. Martin, A. Jossen, A novel measurement technique for parallel-connected lithium-ion cells with controllable interconnection resistance, *J. Power Sources* 503 (1) (2021) 230030, <http://dx.doi.org/10.1016/j.jpowsour.2021.230030>.

[18] M. Ma, Q. Duan, C. Zhao, Q. Wang, J. Sun, Faulty characteristics and identification of increased connecting and internal resistance in parallel-connected lithium-ion battery pack for electric vehicles, *IEEE Trans. Veh. Technol.* 69 (10) (2020) 10797–10808, <http://dx.doi.org/10.1109/TVT.2020.3012354>.

[19] Z. Cui, N. Cui, J. Rao, C. Li, C. Zhang, Current distribution estimation of parallel-connected batteries for inconsistency diagnosis using long short-term

- memory networks, IEEE Trans. Transp. Electr. 8 (1) (2022) 1013–1025, <http://dx.doi.org/10.1109/TTE.2021.3118691>.
- [20] M.P. Klein, J.W. Park, Current distribution measurements in parallel-connected lithium-ion cylindrical cells under non-uniform temperature conditions, J. Electrochem. Soc. 164 (9) (2017) A1893–A1906, <http://dx.doi.org/10.1149/2.0011709jes>.
- [21] S. Paarmann, L. Cloos, J. Technau, T. Wetzel, Measurement of the temperature influence on the current distribution in lithium-ion batteries, Energy Technol. 158 (2021) 2000862, <http://dx.doi.org/10.1002/ente.202000862>.
- [22] T. Baumhöfer, M. Brühl, S. Rothgang, D.U. Sauer, Production caused variation in capacity aging trend and correlation to initial cell performance, J. Power Sources 247 (2014) 332–338, <http://dx.doi.org/10.1016/j.jpowsour.2013.08.108>.
- [23] W. Diao, M. Pecht, T. Liu, Management of imbalances in parallel-connected lithium-ion battery packs, J. Energy Storage 24 (2019) 100781, <http://dx.doi.org/10.1016/j.est.2019.100781>.
- [24] X. Fan, W. Zhang, Z. Wang, F. An, H. Li, J. Jiang, Simplified battery pack modeling considering inconsistency and evolution of current distribution, IEEE Trans. Intell. Transp. Syst. 22 (1) (2021) 630–639, <http://dx.doi.org/10.1109/ITTS.2020.3010567>.
- [25] N. Wassiliadis, M. Ank, L. Wildfeuer, M.K. Kick, M. Lienkamp, Experimental investigation of the influence of electrical contact resistance on lithium-ion battery testing for fast-charge applications, Appl. Energy 295 (7) (2021) 117064, <http://dx.doi.org/10.1016/j.apenergy.2021.117064>.
- [26] M.J. Brand, P.A. Schmidt, M.F. Zaeh, A. Jossen, Welding techniques for battery cells and resulting electrical contact resistances, J. Energy Storage 1 (2015) 7–14, <http://dx.doi.org/10.1016/j.est.2015.04.001>.
- [27] P. Jocher, M.K. Kick, M. Rubio Gomez, A.V. Himmelreich, A. Gruendl, E. Hoover, M.F. Zaeh, A. Jossen, Determination of the contact resistance of planar contacts: Electrically conductive adhesives in battery cell connections, Batteries 9 (9) (2023) 443, <http://dx.doi.org/10.3390/batteries9090443>.
- [28] M. Ecker, J.B. Gerschler, J. Vogel, S. Käbitz, F. Hust, P. Dechent, D.U. Sauer, Development of a lifetime prediction model for lithium-ion batteries based on extended accelerated aging test data, J. Power Sources 215 (2012) 248–257, <http://dx.doi.org/10.1016/j.jpowsour.2012.05.012>.
- [29] M.H. Hofmann, Current Distribution in Parallel-Connected Battery Cells, Dr. Hut, München, 2020.
- [30] P. Kuntz, O. Raccurt, P. Azaïs, K. Richter, T. Waldmann, M. Wohlfahrt-Mehrens, M. Bardet, A. Buzlukov, S. Genies, Identification of degradation mechanisms by post-mortem analysis for high power and high energy commercial li-ion cells after electric vehicle aging, Batteries 7 (3) (2021) 48, <http://dx.doi.org/10.3390/batteries7030048>.
- [31] D. Kucevic, B. Tepe, S. Englberger, A. Parlikar, M. Mühbauer, O. Bohlen, A. Jossen, H. Hesse, Standard battery energy storage system profiles: Analysis of various applications for stationary energy storage systems using a holistic simulation framework, J. Energy Storage 28 (2020) 101077, <http://dx.doi.org/10.1016/j.est.2019.101077>.
- [32] C. Zoerr, J.J. Sturm, S. Solchenbach, S.V. Erhard, A. Latz, Electrochemical polarization-based fast charging of lithium-ion batteries in embedded systems, J. Energy Storage 72 (2023) 108234, <http://dx.doi.org/10.1016/j.est.2023.108234>.
- [33] F. Hust, Physico-Chemically Motivated Parameterization and Modelling of Real-Time Capable Lithium-Ion Battery Models - a Case Study on the Tesla Model S Battery, ISEA, RWTH Aachen University, Aachen, 2018, <http://dx.doi.org/10.18154/RWTH-2019-00249>.
- [34] S. Ludwig, I. Zilberman, M.F. Horsche, T. Wohlers, A. Jossen, Pulse resistance based online temperature estimation for lithium-ion cells, J. Power Sources 490 (6) (2021) 229523, <http://dx.doi.org/10.1016/j.jpowsour.2021.229523>.
- [35] J.P. Schmidt, S. Arnold, A. Loges, D. Werner, T. Wetzel, E. Ivers-Tiffée, Measurement of the internal cell temperature via impedance: Evaluation and application of a new method, J. Power Sources 243 (2013) 110–117, <http://dx.doi.org/10.1016/j.jpowsour.2013.06.013>.
- [36] R. Srinivasan, B.G. Carkhuff, M.H. Butler, A.C. Baisden, Instantaneous measurement of the internal temperature in lithium-ion rechargeable cells, Electrochim. Acta 56 (17) (2011) 6198–6204, <http://dx.doi.org/10.1016/j.electacta.2011.03.136>.
- [37] S. Gantenbein, M. Weiss, E. Ivers-Tiffée, Impedance based time-domain modeling of lithium-ion batteries: Part I, J. Power Sources 379 (2018) 317–327, <http://dx.doi.org/10.1016/j.jpowsour.2018.01.043>.
- [38] S. Ludwig, M. Steinhardt, A. Jossen, Determination of internal temperature differences for various cylindrical lithium-ion batteries using a pulse resistance approach, Batteries 8 (7) (2022) 60, <http://dx.doi.org/10.3390/batteries8070060>.

6 Conclusion

This work examines the factors influencing the current distribution of parallel-connected battery cells. The knowledge of the electrical contact can serve as the basis for any battery system. The first study analyzed factors influencing the measurement of electrical contact resistances and compared different joining methods. The second study presented a novel measurement method with defined boundary conditions. Following that, the influence of inhomogeneous contact resistance and path temperature is investigated for different cell technologies. In total five questions were addressed in this thesis.

Q1 How can electric contact resistance be measured accurately?

Usually, the 4-wire measurement, using power and sense lines, is used to quantify the electrical contact resistance. In this work, influencing factors on measuring electrical resistances were identified. It was demonstrated that the current injection considerably influences voltage measurement and its accuracy. This is particularly important when high accuracy is required for the determination of electrical parameters. The gap between the power and the sense pins should be at least half of the longest side length of the specimen's contact area to determine the electrical parameters and minimize fluctuations from position inaccuracies.

Q2 Is there an optimal design for cell connections to minimize electrical contact resistance?

The current distribution in area-based connections could be quantified as a second finding of the first study. An analysis showed the relationship between the resistances of the specimens and the contact. With a very good electrical contact, which corresponds to a low contact resistance, the current flows through the contact area at the two edges of the surface aligned orthogonally to the current direction. In this case, the contact resistance is primarily affected by the length of the edges but not by the cross-sectional area. Consequently, the positioning of these two weld seams should be as orthogonal to the direction of the current and as far away from each other as possible.

Q3 Which resistances result from ECA in comparison to well-established joining techniques?

Based on *Q1* and *Q2*, well-established joining techniques such as welding, press connections and soldering are compared with ECA. The adhesive was found to have a low contact resistance and a high mechanical strength in the same order as the well-established joining techniques. In an economic assessment, the costs for ECA are significantly higher than for laser beam welding.

Q4 How can the current distribution be measured efficiently in the presence of inhomogeneous contact resistances and path temperature?

A novel test-bench was developed to investigate the current distribution in the presence of inhomogeneous contact resistances and path temperature. Within the novel method, a battery cyler was used to couple cells to each other using Kirchhoff's voltage and current law. By connecting each cell using the 4-wire measurement technique, the influence of interconnections and measurement equipment can be neglected. In contrast, the connection via equations enables the introduction of clearly defined path resistances. Furthermore, the cells can be cycled in different climate chambers, allowing to analyse of inhomogeneous temperatures.

Q5 How does an inhomogeneous contact resistance or path temperature influence the system performance in a parallel configuration?

Three different state-of-the-art cell technologies were examined to analyze inhomogeneous contact resistance or path temperature in a parallel configuration. Different characteristics of the current distribution, such as the maximum path current or SoC difference, were measured to analyze the inhomogeneities. In order to analyze the inhomogeneity, sensitivity factors were introduced, which were based on the linearity of the characteristics observed over the inhomogeneity. In summary, the OCV, the R_{DC} resistance, and the temperature stability define the sensitivity of the current distribution. A steep OCV curve and a low-temperature sensitivity ensure a homogeneous current distribution, as the LIB_{NCA} presents. In contrast, the LIB_{LFP} exhibits a flat OCV, making it more sensitive to inhomogeneities. The SIB shows a steep OCV but a high-temperature sensitivity, resulting in a high sensitivity against temperature inhomogeneities but less against resistance inhomogeneities.

Outlook

Based on the results of this work, subsequent studies should examine how the inhomogeneities develop over the aging process. The aim is to identify factors influencing convergent and divergent aging.

In addition, virtual coupling offers great potential for follow-up studies. Besides the temperature difference, external pressure could be analyzed, as the cells can be located in different places. In addition, with the European Green Deal, cells must be interchangeable for specific applications. It could, therefore, be investigated how cells with different state-of-health (SoH) behave in the parallel network initially and during cycling. Moreover, this work focused only on the 2p configuration. Scaling into np configuration is straightforward with the VPC and fills a gap in the literature. As mentioned in Chapter 2.4.2, a further development of the VPC according to dynamics current profiles should be considered. Implementing the methodology directly in the microcontroller could be advantageous in keeping a smoother transient response.

In addition, the cells were convectively tempered in this work. Further work could focus on the cooling strategy and the thermal connection to the cells. With side cooling across parallel-connected cells, for example, only a part of the possible surface is tempered. This results in temperature inhomogeneities within the cell. An analysis at EP level could provide insight.

Besides that, future studies might explore different current profiles. While this thesis only considered CC profiles, the behavior of partial cycling, especially across areas where the different voltage shows significant changes, could be of interest. Additionally, examining the behavior in high-performance settings, such as the fast charging of cells connected in parallel, could provide valuable insights. Further battery systems based on lithium-sulfur, ASSB (All-solid-state-battery), or variants of sodium-ion technology could be examined for their sensitivity to temperature and resistance inhomogeneities.

References

- [1] Guarnieri, M.: *Looking back to electric cars*. In: *2012 Third IEEE History of Electrotechnology*, pp. 1–6. DOI: 10.1109/HISTELCON.2012.6487583 (see p. 1).
- [2] Statista: *eMobility: in-depth market analysis | Statista*. 2023. URL: <https://www.statista.com/study/49240/emobility---market-insights-and-data-analysis/> (visited on 01/15/2024) (see p. 1).
- [3] Blomgren, G. E.: *The Development and Future of Lithium Ion Batteries*. In: *Journal of The Electrochemical Society* 164.1 (2017), A5019–A5025. ISSN: 0013-4651. DOI: 10.1149/2.0251701jes (see p. 1).
- [4] Wood, D. L., Li, J., and Daniel, C.: *Prospects for reducing the processing cost of lithium ion batteries*. In: *Journal of Power Sources* 275 (2015), pp. 234–242. ISSN: 03787753. DOI: 10.1016/j.jpowsour.2014.11.019 (see p. 1).
- [5] Jacobson, M. Z. et al.: *100% Clean and Renewable Wind, Water, and Sunlight All-Sector Energy Roadmaps for 139 Countries of the World*. In: *Joule* 1.1 (2017), pp. 108–121. ISSN: 25424351. DOI: 10.1016/j.joule.2017.07.005 (see p. 1).
- [6] Kovárník, R. and Staňková, M.: *Determinants of Electric Car Sales in Europe*. In: *LOGI – Scientific Journal on Transport and Logistics* 12.1 (2021), pp. 214–225. DOI: 10.2478/logi-2021-0020 (see p. 1).
- [7] IEA: *Global EV Outlook 2023*. 2023. URL: <https://www.iea.org/reports/global-ev-outlook-2023> (visited on 03/25/2024) (see p. 1).
- [8] Peng, R., Tang, J. H. C. G., Yang, X., Meng, M., Zhang, J., and Zhuge, C.: *Investigating the factors influencing the electric vehicle market share: A comparative study of the European Union and United States*. In: *Applied Energy* 355 (2024), p. 122327. ISSN: 03062619. DOI: 10.1016/j.apenergy.2023.122327 (see p. 2).
- [9] Statista: *Projected global battery demand by application | Statista*. 2021. URL: <https://www.statista.com/statistics/1103218/global-battery-demand-forecast/> (visited on 01/16/2024) (see p. 2).
- [10] Ahmeid, M., Muhammad, M., Milojevic, Z., Lambert, S., and Attidekou, P.: “The Energy Loss Due to Interconnections in Paralleled Cell Configurations of Lithium-Ion Batteries in Electric Vehicles.” In: *2019 IEEE 4th International Future Energy Electronics Conference (IFEEEC)*. IEEE, 2019, pp. 1–4. ISBN: 978-1-7281-3153-5. DOI: 10.1109/IFEEEC47410.2019.9014956 (see p. 2).
- [11] Nguyen, R. T., Toba, A.-L., Severson, M. H., Woodbury, E. M., Carey, A. R., and Devin Imholte, D.: *A market-oriented database design for critical material research*. In: *Clean Technologies and Recycling* 1.1 (2021), pp. 34–49. ISSN: 2770-4580. DOI: 10.3934/ctr.2021002 (see p. 2).
- [12] BYD: *BYD ATTO 3: Stilvolles und Dynamisches C-SUV | BYD Deutschland*. 2024-03-12. URL: <https://www.byd.com/de/car/atto3> (visited on 03/12/2024) (see p. 2).

- [13] *CATL and BYD to use sodium-ion batteries in EVs this year* | *electrive.com*. 2024-03-13. URL: <https://www.electrive.com/2023/04/21/catl-and-byd-to-use-sodium-ion-batteries-in-evs-this-year/> (visited on 03/13/2024) (see p. 3).
- [14] Jocher, P., Kick, M. K., Rubio Gomez, M., Himmelreich, A. V., Gruendl, A., Hoover, E., Zaeh, M. F., and Jossen, A.: *Determination of the Contact Resistance of Planar Contacts: Electrically Conductive Adhesives in Battery Cell Connections*. In: *Batteries* 9.9 (2023), p. 443. DOI: 10.3390/batteries9090443 (see pp. 4, 21, 24).
- [15] Jocher, P., Steinhardt, M., Ludwig, S., Schindler, M., Martin, J., and Jossen, A.: *A novel measurement technique for parallel-connected lithium-ion cells with controllable interconnection resistance*. In: *Journal of Power Sources* 503 (2021), p. 230030. ISSN: 03787753. DOI: 10.1016/j.jpowsour.2021.230030 (see pp. 4, 15, 18, 26).
- [16] Jocher, P., Roehrer, F., Rehm, M., Idrizi, T., Himmelreich, A., and Jossen, A.: *Scaling from cell to system: Comparing Lithium-ion and Sodium-ion technologies regarding inhomogeneous resistance and temperature in parallel configuration by sensitivity factors*. In: *Journal of Energy Storage* 98 (2024), p. 112931. ISSN: 2352152X. DOI: 10.1016/j.est.2024.112931 (see p. 4).
- [17] Armand, M. et al.: *Lithium-ion batteries – Current state of the art and anticipated developments*. In: *Journal of Power Sources* 479 (2020), p. 228708. ISSN: 03787753. DOI: 10.1016/j.jpowsour.2020.228708 (see p. 7).
- [18] Jossen, A.: *Fundamentals of battery dynamics*. In: *Journal of Power Sources* 154.2 (2006), pp. 530–538. ISSN: 03787753. DOI: 10.1016/j.jpowsour.2005.10.041 (see p. 7).
- [19] Park, M., Zhang, X., Chung, M., Less, G. B., and Sastry, A. M.: *A review of conduction phenomena in Li-ion batteries*. In: *Journal of Power Sources* 195.24 (2010), pp. 7904–7929. ISSN: 03787753. DOI: 10.1016/j.jpowsour.2010.06.060 (see p. 7).
- [20] Illig, J.: *Physically based Impedance Modelling of Lithium-Ion Cells*. Dissertation. Karlsruhe: Karlsruher Institut für Technologie, 2014. DOI: 10.5445/KSP/1000042281 (see p. 7).
- [21] Gantenbein, S., Weiss, M., and Ivers-Tiffée, E.: *Impedance based time-domain modeling of lithium-ion batteries: Part I*. In: *Journal of Power Sources* 379 (2018), pp. 317–327. ISSN: 03787753. DOI: 10.1016/j.jpowsour.2018.01.043 (see p. 7).
- [22] Buchberger, I.: *Electrochemical and structural investigations on lithium-ion battery materials and related degradation processes*. Dissertation. München: Universitätsbibliothek der TU München, 2016 (see p. 7).
- [23] Zhou, X., Huang, J., Pan, Z., and Ouyang, M.: *Impedance characterization of lithium-ion batteries aging under high-temperature cycling: Importance of electrolyte-phase diffusion*. In: *Journal of Power Sources* 426 (2019), pp. 216–222. ISSN: 03787753. DOI: 10.1016/j.jpowsour.2019.04.040 (see p. 7).
- [24] Pistoia, G. and Liaw, B. Y., eds.: *Behaviour of lithium-ion batteries in electric vehicles: Battery health, performance, safety, and cost*. Engineering. Cham: Springer, 2018. ISBN: 978-3-319-69950-9 (see p. 8).
- [25] Kerler, M.: *Eine Methode zur Bestimmung der optimalen Zellgröße für Elektrofahrzeuge*. Dissertation. Verlag Dr. Hut, 2019 (see pp. 8, 10).

- [26] Wildfeuer, L., Wassiliadis, N., Reiter, C., Baumann, M., and Lienkamp, M.: “Experimental Characterization of Li-Ion Battery Resistance at the Cell, Module and Pack Level.” In: *2019 Fourteenth International Conference on Ecological Vehicles and Renewable Energies (EVER)*. IEEE, 2019, pp. 1–12. ISBN: 978-1-7281-3703-2. DOI: 10.1109/EVER.2019.8813578 (see p. 8).
- [27] L bberding, H., Wessel, S., Offermanns, C., Kehrer, M., Rother, J., Heimes, H., and Kampker, A.: *From Cell to Battery System in BEVs: Analysis of System Packing Efficiency and Cell Types*. In: *World Electric Vehicle Journal* 11.4 (2020), p. 77. DOI: 10.3390/wevj11040077 (see p. 8).
- [28] Zwicker, M., Moghadam, M., Zhang, W., and Nielsen, C. V.: *Automotive battery pack manufacturing – a review of battery to tab joining*. In: *Journal of Advanced Joining Processes* 1 (2020), p. 100017. ISSN: 26663309. DOI: 10.1016/j.jajp.2020.100017 (see pp. 8, 15).
- [29] BMW Group PressClub: *Mehr Leistung, CO2-reduzierte Produktion, Kosten deutlich reduziert: Die BMW Group setzt in der Neuen Klasse ab 2025 innovative BMW Batteriezellen im Rundformat ein*. 2024-02-29. URL: <https://www.press.bmwgroup.com/deutschland/article/detail/T0403470DE/mehr-leistung-co2-reduzierte-produktion-kosten-deutlich-reduziert-die-bmw-group-setzt-in-der-neuen> (visited on 02/29/2024) (see p. 8).
- [30] Pampel, F., Pischinger, S., and Teuber, M.: *A systematic comparison of the packing density of battery cell-to-pack concepts at different degrees of implementation*. In: *Results in Engineering* 13 (2022), p. 100310. ISSN: 25901230. DOI: 10.1016/j.rineng.2021.100310 (see p. 8).
- [31] Jung, C.: *Power Up with 800-V Systems: The benefits of upgrading voltage power for battery-electric passenger vehicles*. In: *IEEE Electrification Magazine* 5.1 (2017), pp. 53–58. ISSN: 2325-5897. DOI: 10.1109/MELE.2016.2644560 (see p. 9).
- [32] Aghabali, I., Bauman, J., Kollmeyer, P. J., Wang, Y., Bilgin, B., and Emadi, A.: *800-V Electric Vehicle Powertrains: Review and Analysis of Benefits, Challenges, and Future Trends*. In: *IEEE Transactions on Transportation Electrification* 7.3 (2021), pp. 927–948. DOI: 10.1109/TTE.2020.3044938 (see p. 9).
- [33] Frank, A., Sturm, J., Steinhardt, M., Rheinfeld, A., and Jossen, A.: *Impact of Current Collector Design and Cooling Topology on Fast Charging of Cylindrical Lithium-Ion Batteries*. In: *ECS Advances* 1.4 (2022), p. 040502. DOI: 10.1149/2754-2734/ac97e0 (see p. 9).
- [34] Kim, K. and Choi, J.-I.: *Effect of cell-to-cell variation and module configuration on the performance of lithium-ion battery systems*. In: *Applied Energy* 352 (2023), p. 121888. ISSN: 03062619. DOI: 10.1016/j.apenergy.2023.121888 (see p. 10).
- [35] Fleckenstein, M., Bohlen, O., Roscher, M. A., and B ker, B.: *Current density and state of charge inhomogeneities in Li-ion battery cells with LiFePO₄ as cathode material due to temperature gradients*. In: *Journal of Power Sources* 196.10 (2011), pp. 4769–4778. ISSN: 03787753. DOI: 10.1016/j.jpowsour.2011.01.043 (see pp. 9, 11, 17).
- [36] Osswald, P. J., Erhard, S. V., Noel, A., Keil, P., Kindermann, F. M., Hoster, H., and Jossen, A.: *Current density distribution in cylindrical Li-Ion cells during impedance measurements*. In: *Journal of Power Sources* 314 (2016), pp. 93–101. ISSN: 03787753. DOI: 10.1016/j.jpowsour.2016.02.070 (see p. 9).
- [37] Zhang, G., Shaffer, C. E., Wang, C.-Y., and Rahn, C. D.: *Effects of Non-Uniform Current Distribution on Energy Density of Li-Ion Cells*. In: *Journal of The Electrochemical Society* 160.11 (2013), A2299–A2305. ISSN: 0013-4651. DOI: 10.1149/2.061311jes (see pp. 9, 18).

- [38] Zhang, G., Shaffer, C. E., Wang, C.-Y., and Rahn, C. D.: *In-Situ Measurement of Current Distribution in a Li-Ion Cell*. In: *Journal of The Electrochemical Society* 160.4 (2013), A610–A615. ISSN: 0013-4651. DOI: 10.1149/2.046304jes (see pp. 9, 17).
- [39] Baumann, M., Wildfeuer, L., Rohr, S., and Lienkamp, M.: *Parameter variations within Li-Ion battery packs – Theoretical investigations and experimental quantification*. In: *Journal of Energy Storage* 18 (2018), pp. 295–307. ISSN: 2352152X. DOI: 10.1016/j.est.2018.04.031 (see pp. 10, 17, 18).
- [40] Shi, W., Hu, X., Jin, C., Jiang, J., Zhang, Y., and Yip, T.: *Effects of imbalanced currents on large-format LiFePO₄ /graphite batteries systems connected in parallel*. In: *Journal of Power Sources* 313 (2016), pp. 198–204. ISSN: 03787753. DOI: 10.1016/j.jpowsour.2016.02.087 (see pp. 10, 18).
- [41] Baumhöfer, T., Brühl, M., Rothgang, S., and Sauer, D. U.: *Production caused variation in capacity aging trend and correlation to initial cell performance*. In: *Journal of Power Sources* 247 (2014), pp. 332–338. ISSN: 03787753. DOI: 10.1016/j.jpowsour.2013.08.108 (see p. 10).
- [42] Piombo, G., Fasolato, S., Heymer, R., Hidalgo, M., Faraji Niri, M., Onori, S., and Marco, J.: *Unveiling the performance impact of module level features on parallel-connected lithium-ion cells via explainable machine learning techniques on a full factorial design of experiments*. In: *Journal of Energy Storage* 84 (2024), p. 110783. ISSN: 2352152X. DOI: 10.1016/j.est.2024.110783 (see p. 10).
- [43] Zheng, Y., Che, Y., Hu, X., Sui, X., Stroe, D.-I., and Teodorescu, R.: *Thermal state monitoring of lithium-ion batteries: Progress, challenges, and opportunities*. In: *Progress in Energy and Combustion Science* 100 (2024), p. 101120. ISSN: 03601285. DOI: 10.1016/j.pecs.2023.101120 (see pp. 10, 11).
- [44] Waldmann, T., Wilka, M., Kasper, M., Fleischhammer, M., and Wohlfahrt-Mehrens, M.: *Temperature dependent ageing mechanisms in Lithium-ion batteries – A Post-Mortem study*. In: *Journal of Power Sources* 262 (2014), pp. 129–135. ISSN: 03787753. DOI: 10.1016/j.jpowsour.2014.03.112 (see pp. 10, 11).
- [45] Ma, S., Jiang, M., Tao, P., Song, C., Wu, J., Wang, J., Deng, T., and Shang, W.: *Temperature effect and thermal impact in lithium-ion batteries: A review*. In: *Progress in Natural Science: Materials International* 28.6 (2018), pp. 653–666. ISSN: 10020071. DOI: 10.1016/j.pnsc.2018.11.002 (see p. 10).
- [46] Morello, R., Di Rienzo, R., Roncella, R., Saletti, R., Schwarz, R., Lorentz, V., Hoedemaekers, E., Rosca, B., and Baronti, F.: “Advances in Li-Ion Battery Management for Electric Vehicles.” In: *IECON 2018 - 44th Annual Conference of the IEEE Industrial Electronics Society*. IEEE, 2018, pp. 4949–4955. ISBN: 978-1-5090-6684-1. DOI: 10.1109/IECON.2018.8591185 (see p. 10).
- [47] Alipour, M., Ziebert, C., Conte, F. V., and Kizilel, R.: *A Review on Temperature-Dependent Electrochemical Properties, Aging, and Performance of Lithium-Ion Cells*. In: *Batteries* 6.3 (2020), p. 35. DOI: 10.3390/batteries6030035 (see p. 10).
- [48] Lopez, C. F., Jeevarajan, J. A., and Mukherjee, P. P.: *Evaluation of Combined Active and Passive Thermal Management Strategies for Lithium-Ion Batteries*. In: *Journal of Electrochemical Energy Conversion and Storage* 13.3 (2016). ISSN: 2381-6872. DOI: 10.1115/1.4035245 (see p. 10).

- [49] Xu, J., Lan, C., Qiao, Y., and Ma, Y.: *Prevent thermal runaway of lithium-ion batteries with minichannel cooling*. In: *Applied Thermal Engineering* 110 (2017), pp. 883–890. ISSN: 13594311. DOI: 10.1016/j.applthermaleng.2016.08.151 (see p. 10).
- [50] Akbarzadeh, M., Kalogiannis, T., Jaguemont, J., Jin, L., Behi, H., Karimi, D., Beheshti, H., van Mierlo, J., and Bercibar, M.: *A comparative study between air cooling and liquid cooling thermal management systems for a high-energy lithium-ion battery module*. In: *Applied Thermal Engineering* 198 (2021), p. 117503. ISSN: 13594311. DOI: 10.1016/j.applthermaleng.2021.117503 (see p. 10).
- [51] Ghaeminezhad, N., Wang, Z., and Ouyang, Q.: *A Review on lithium-ion battery thermal management system techniques: A control-oriented analysis*. In: *Applied Thermal Engineering* 219 (2023), p. 119497. ISSN: 13594311. DOI: 10.1016/j.applthermaleng.2022.119497 (see p. 10).
- [52] Chen, D., Jiang, J., Kim, G.-H., Yang, C., and Pesaran, A.: *Comparison of different cooling methods for lithium ion battery cells*. In: *Applied Thermal Engineering* 94 (2016), pp. 846–854. ISSN: 13594311. DOI: 10.1016/j.applthermaleng.2015.10.015 (see p. 11).
- [53] Zhao, C., Cao, W., Dong, T., and Jiang, F.: *Thermal behavior study of discharging/charging cylindrical lithium-ion battery module cooled by channeled liquid flow*. In: *International Journal of Heat and Mass Transfer* 120 (2018), pp. 751–762. ISSN: 00179310. DOI: 10.1016/j.ijheatmasstransfer.2017.12.083 (see p. 11).
- [54] Ye, Y., Saw, L. H., Shi, Y., Somasundaram, K., and Tay, A. A.: *Effect of thermal contact resistances on fast charging of large format lithium ion batteries*. In: *Electrochimica Acta* 134 (2014), pp. 327–337. ISSN: 00134686. DOI: 10.1016/j.electacta.2014.04.134 (see p. 11).
- [55] Roe, C. et al.: *Immersion cooling for lithium-ion batteries – A review*. In: *Journal of Power Sources* 525 (2022), p. 231094. ISSN: 03787753. DOI: 10.1016/j.jpowsour.2022.231094 (see p. 11).
- [56] Hu, X., Zheng, Y., Howey, D. A., Perez, H., Foley, A., and Pecht, M.: *Battery warm-up methodologies at subzero temperatures for automotive applications: Recent advances and perspectives*. In: *Progress in Energy and Combustion Science* 77 (2020), p. 100806. ISSN: 03601285. DOI: 10.1016/j.peccs.2019.100806 (see p. 11).
- [57] Richardson, R. R., Zhao, S., and Howey, D. A.: *On-board monitoring of 2-D spatially-resolved temperatures in cylindrical lithium-ion batteries: Part I. Low-order thermal modelling*. In: *Journal of Power Sources* 326 (2016), pp. 377–388. ISSN: 03787753. DOI: 10.1016/j.jpowsour.2016.06.103 (see p. 11).
- [58] Sun, H. and Dixon, R.: *Development of a Liquid Cooled Battery Module*. In: *Journal of The Electrochemical Society* 163.10 (2016), E313–E321. ISSN: 0013-4651. DOI: 10.1149/2.1081610jes (see p. 11).
- [59] Forgez, C., Vinh Do, D., Friedrich, G., Morcrette, M., and Delacourt, C.: *Thermal modeling of a cylindrical LiFePO₄/graphite lithium-ion battery*. In: *Journal of Power Sources* 195.9 (2010), pp. 2961–2968. ISSN: 03787753. DOI: 10.1016/j.jpowsour.2009.10.105 (see p. 11).
- [60] Yang, X., Gao, X., Zhang, F., Luo, W., and Duan, Y.: *Experimental study on temperature difference between the interior and surface of Li[Ni_{1/3}Co_{1/3}Mn_{1/3}]O₂ prismatic lithium-ion batteries at natural convection and adiabatic condition*. In: *Applied Thermal Engineering* 190 (2021), p. 116746. ISSN: 13594311. DOI: 10.1016/j.applthermaleng.2021.116746 (see p. 11).

- [61] Gepp, M., Reisenweber, H., Lorentz, V., and Marz, M.: “Temperature gradient reduction in high-power battery systems using prismatic cells combined with Phase-Change Sheets and Graphite foils.” In: *IECON 2016 - 42nd Annual Conference of the IEEE Industrial Electronics Society*. IEEE, 2016, pp. 5519–5524. ISBN: 978-1-5090-3474-1. DOI: 10.1109/IECON.2016.7793497 (see p. 11).
- [62] Dai, H., Jiang, B., and Wei, X.: *Impedance Characterization and Modeling of Lithium-Ion Batteries Considering the Internal Temperature Gradient*. In: *Energies* 11.1 (2018), p. 220. DOI: 10.3390/en11010220 (see p. 11).
- [63] Fleckenstein, M., Bohlen, O., and Bäker, B.: *Aging Effect of Temperature Gradients in Li-ion Cells Experimental and Simulative Investigations and the Consequences on Thermal Battery Management*. In: *World Electric Vehicle Journal* 5.2 (2012), pp. 322–333. DOI: 10.3390/wevj5020322 (see p. 11).
- [64] Martiny, N., Osswald, P., Huber, C., and Jossen, A.: *Safety Management for Electric Vehicle Batteries in a Tropic Environment*. In: *World Electric Vehicle Journal* 5.2 (2012), pp. 394–404. DOI: 10.3390/wevj5020394 (see p. 11).
- [65] Fill, A., Mader, T., Schmidt, T., Avdyli, A., Kopp, M., and Birke, K. P.: *Experimental investigations on current and temperature imbalances among parallel-connected lithium-ion cells at different thermal conditions*. In: *Journal of Energy Storage* 51 (2022), p. 104325. ISSN: 2352152X. DOI: 10.1016/j.est.2022.104325 (see pp. 11, 18).
- [66] Fill, A., Mader, T., Schmidt, T., Llorente, R., and Birke, K. P.: *Measuring Test Bench with Adjustable Thermal Connection of Cells to Their Neighbors and a New Model Approach for Parallel-Connected Cells*. In: *Batteries* 6.1 (2020), p. 2. DOI: 10.3390/batteries6010002 (see pp. 11, 17, 18).
- [67] Cavalheiro, G. M., Iriyama, T., Nelson, G. J., Huang, S., and Zhang, G.: *Effects of Nonuniform Temperature Distribution on Degradation of Lithium-Ion Batteries*. In: *Journal of Electrochemical Energy Conversion and Storage* 17.2 (2020). ISSN: 2381-6872. DOI: 10.1115/1.4045205 (see pp. 11, 18).
- [68] Al-Amin, M., Barai, A., Ashwin, T. R., and Marco, J.: *An Insight to the Degradation Behaviour of the Parallel Connected Lithium-Ion Battery Cells*. In: *Energies* 14.16 (2021), p. 4716. DOI: 10.3390/en14164716 (see pp. 11, 18).
- [69] Zilberman, I., Ludwig, S., Schiller, M., and Jossen, A.: *Online aging determination in lithium-ion battery module with forced temperature gradient*. In: *Journal of Energy Storage* 28 (2020), p. 101170. ISSN: 2352152X. DOI: 10.1016/j.est.2019.101170 (see p. 11).
- [70] Naylor Marlow, M., Chen, J., and Wu, B.: *Degradation in parallel-connected lithium-ion battery packs under thermal gradients*. In: *Communications Engineering* 3.1 (2024). DOI: 10.1038/s44172-023-00153-5 (see pp. 11, 12, 17, 18).
- [71] Klein, M. P. and Park, J. W.: *Current Distribution Measurements in Parallel-Connected Lithium-Ion Cylindrical Cells under Non-Uniform Temperature Conditions*. In: *Journal of The Electrochemical Society* 164.9 (2017), A1893–A1906. ISSN: 0013-4651. DOI: 10.1149/2.0011709jes (see pp. 11, 17, 18).
- [72] Paarmann, S., Cloos, L., Technau, J., and Wetzel, T.: *Measurement of the Temperature Influence on the Current Distribution in Lithium-Ion Batteries*. In: *Energy Technology* 9.6 (2021). ISSN: 2194-4288. DOI: 10.1002/ente.202000862 (see pp. 12, 17, 18).

- [73] Schindler, M., Jocher, P., Durdel, A., and Jossen, A.: *Analyzing the Aging Behavior of Lithium-Ion Cells Connected in Parallel Considering Varying Charging Profiles and Initial Cell-to-Cell Variations*. In: *Journal of The Electrochemical Society* 168.9 (2021), p. 090524. ISSN: 0013-4651. DOI: 10.1149/1945-7111/ac2089 (see pp. 12, 14, 17, 18).
- [74] Hust, F. E.: *Physico-Chemically Motivated Parameterization and Modelling of Real-Time Capable Lithium-Ion Battery Models - a Case Study on the Tesla Model S Battery*. Dissertation. Aachen: RWTH Aachen University, 2018 (see pp. 12, 14, 17, 18).
- [75] Hofmann, M. H., Czyrka, K., Brand, M. J., Steinhardt, M., Noel, A., Spingler, F. B., and Jossen, A.: *Dynamics of current distribution within battery cells connected in parallel*. In: *Journal of Energy Storage* 20 (2018), pp. 120–133. ISSN: 2352152X. DOI: 10.1016/j.est.2018.08.013 (see pp. 12, 14).
- [76] Sturm, J., Rheinfeld, A., Zilberman, I., Spingler, F. B., Kosch, S., Frie, F., and Jossen, A.: *Modeling and simulation of inhomogeneities in a 18650 nickel-rich, silicon-graphite lithium-ion cell during fast charging*. In: *Journal of Power Sources* 412 (2019), pp. 204–223. ISSN: 03787753. DOI: 10.1016/j.jpowsour.2018.11.043 (see p. 12).
- [77] Dubarry, M., Truchot, C., and Liaw, B. Y.: *Synthesize battery degradation modes via a diagnostic and prognostic model*. In: *Journal of Power Sources* 219 (2012), pp. 204–216. ISSN: 03787753. DOI: 10.1016/j.jpowsour.2012.07.016 (see p. 12).
- [78] Schmitt, J., Schindler, M., and Jossen, A.: *Change in the half-cell open-circuit potential curves of silicon-graphite and nickel-rich lithium nickel manganese cobalt oxide during cycle aging*. In: *Journal of Power Sources* 506 (2021), p. 230240. ISSN: 03787753. DOI: 10.1016/j.jpowsour.2021.230240 (see p. 12).
- [79] Farmann, A. and Sauer, D. U.: *A study on the dependency of the open-circuit voltage on temperature and actual aging state of lithium-ion batteries*. In: *Journal of Power Sources* 347 (2017), pp. 1–13. ISSN: 03787753. DOI: 10.1016/j.jpowsour.2017.01.098 (see p. 12).
- [80] Schindler, M., Sturm, J., Ludwig, S., Schmitt, J., and Jossen, A.: *Evolution of initial cell-to-cell variations during a three-year production cycle*. In: *eTransportation* 8 (2021), p. 100102. ISSN: 25901168. DOI: 10.1016/j.etrans.2020.100102 (see pp. 14, 15).
- [81] Rumpf, K., Naumann, M., and Jossen, A.: *Experimental investigation of parametric cell-to-cell variation and correlation based on 1100 commercial lithium-ion cells*. In: *Journal of Energy Storage* 14 (2017), pp. 224–243. ISSN: 2352152X. DOI: 10.1016/j.est.2017.09.010 (see p. 14).
- [82] Miyatake, S., Susuki, Y., Hikiyama, T., Itoh, S., and Tanaka, K.: *Discharge characteristics of multicell lithium-ion battery with nonuniform cells*. In: *Journal of Power Sources* 241 (2013), pp. 736–743. ISSN: 03787753. DOI: 10.1016/j.jpowsour.2013.05.179 (see pp. 14, 18).
- [83] Gogoana, R., Pinson, M. B., Bazant, M. Z., and Sarma, S. E.: *Internal resistance matching for parallel-connected lithium-ion cells and impacts on battery pack cycle life*. In: *Journal of Power Sources* 252 (2014), pp. 8–13. ISSN: 03787753. DOI: 10.1016/j.jpowsour.2013.11.101 (see pp. 14, 17, 18).
- [84] Pastor-Fernández, C., Bruen, T., Widanage, W. D., Gama-Valdez, M. A., and Marco, J.: *A Study of Cell-to-Cell Interactions and Degradation in Parallel Strings: Implications for the Battery Management System*. In: *Journal of Power Sources* 329 (2016), pp. 574–585. ISSN: 03787753. DOI: 10.1016/j.jpowsour.2016.07.121 (see pp. 14, 18).

- [85] Brand, M. J., Hofmann, M. H., Steinhardt, M., Schuster, S. F., and Jossen, A.: *Current distribution within parallel-connected battery cells*. In: *Journal of Power Sources* 334 (2016), pp. 202–212. ISSN: 03787753. DOI: 10.1016/j.jpowsour.2016.10.010 (see pp. 14, 17, 18).
- [86] Wu, M.-S., Lin, C.-Y., Wang, Y.-Y., Wan, C.-C., and Yang, C. R.: *Numerical simulation for the discharge behaviors of batteries in series and/or parallel-connected battery pack*. In: *Electrochimica Acta* 52.3 (2006), pp. 1349–1357. ISSN: 00134686. DOI: 10.1016/j.electacta.2006.07.036 (see p. 14).
- [87] An, F., Chen, L., Huang, J., Zhang, J., and Li, P.: *Rate dependence of cell-to-cell variations of lithium-ion cells*. In: *Scientific reports* 6 (2016), p. 35051. DOI: 10.1038/srep35051 (see p. 14).
- [88] Hosseinzadeh, E., Odio, M. X., Marco, J., and Jennings, P.: “Unballanced Performance of Parallel Connected Large Format Lithium Ion Batteries for Electric Vehicle Application.” In: *2019 International Conference on Smart Energy Systems and Technologies (SEST)*. IEEE, 2019, pp. 1–6. ISBN: 978-1-7281-1156-8. DOI: 10.1109/SEST.2019.8849060 (see p. 14).
- [89] Fill, A., Koch, S., Pott, A., and Birke, K.-P.: *Current distribution of parallel-connected cells in dependence of cell resistance, capacity and number of parallel cells*. In: *Journal of Power Sources* 407 (2018), pp. 147–152. ISSN: 03787753. DOI: 10.1016/j.jpowsour.2018.10.061 (see pp. 14, 18).
- [90] Fill, A., Koch, S., and Birke, K. P.: *Analytical model of the current distribution of parallel-connected battery cells and strings*. In: *Journal of Energy Storage* 23 (2019), pp. 37–43. ISSN: 2352152X. DOI: 10.1016/j.est.2019.02.031 (see pp. 14, 18).
- [91] Hosseinzadeh, E., Arias, S., Krishna, M., Worwood, D., Barai, A., Widanalage, D., and Marco, J.: *Quantifying cell-to-cell variations of a parallel battery module for different pack configurations*. In: *Applied Energy* 282 (2021), p. 115859. ISSN: 03062619. DOI: 10.1016/j.apenergy.2020.115859 (see p. 14).
- [92] Cordoba-Arenas, A., Onori, S., and Rizzoni, G.: *A control-oriented lithium-ion battery pack model for plug-in hybrid electric vehicle cycle-life studies and system design with consideration of health management*. In: *Journal of Power Sources* 279 (2015), pp. 791–808. ISSN: 03787753. DOI: 10.1016/j.jpowsour.2014.12.048 (see pp. 14, 18).
- [93] Srinivasan, V. and Wang, C. Y.: *Analysis of Electrochemical and Thermal Behavior of Li-Ion Cells*. In: *Journal of The Electrochemical Society* 150.1 (2003), A98–A106. ISSN: 0013-4651. DOI: 10.1149/1.1526512 (see p. 14).
- [94] Schmidt, J. P., Arnold, S., Loges, A., Werner, D., Wetzel, T., and Ivers-Tiffée, E.: *Measurement of the internal cell temperature via impedance: Evaluation and application of a new method*. In: *Journal of Power Sources* 243 (2013), pp. 110–117. ISSN: 03787753. DOI: 10.1016/j.jpowsour.2013.06.013 (see p. 14).
- [95] Taheri, P., Hsieh, S., and Bahrami, M.: *Investigating electrical contact resistance losses in lithium-ion battery assemblies for hybrid and electric vehicles*. In: *Journal of Power Sources* 196.15 (2011), pp. 6525–6533. ISSN: 03787753. DOI: 10.1016/j.jpowsour.2011.03.056 (see p. 15).
- [96] Saw, L. H., Ye, Y., and Tay, A.: *Electrochemical-thermal analysis of 18650 Lithium Iron Phosphate cell*. In: *Energy Conversion and Management* 75 (2013), pp. 162–174. ISSN: 01968904. DOI: 10.1016/j.enconman.2013.05.040 (see p. 15).

- [97] Wassiliadis, N., Ank, M., Wildfeuer, L., Kick, M. K., and Lienkamp, M.: *Experimental investigation of the influence of electrical contact resistance on lithium-ion battery testing for fast-charge applications*. In: *Applied Energy* 295 (2021), p. 117064. ISSN: 03062619. DOI: 10.1016/j.apenergy.2021.117064 (see p. 15).
- [98] Offer, G. J., Yufit, V., Howey, D. A., Wu, B., and Brandon, N. P.: *Module design and fault diagnosis in electric vehicle batteries*. In: *Journal of Power Sources* 206 (2012), pp. 383–392. ISSN: 03787753. DOI: 10.1016/j.jpowsour.2012.01.087 (see p. 15).
- [99] Wu, B., Yufit, V., Marinescu, M., Offer, G. J., Martinez-Botas, R. F., and Brandon, N. P.: *Coupled thermal–electrochemical modelling of uneven heat generation in lithium-ion battery packs*. In: *Journal of Power Sources* 243 (2013), pp. 544–554. ISSN: 03787753. DOI: 10.1016/j.jpowsour.2013.05.164 (see p. 15).
- [100] Das, A., Li, D., Williams, D., and Greenwood, D.: *Joining Technologies for Automotive Battery Systems Manufacturing*. In: *World Electric Vehicle Journal* 9.2 (2018), p. 22. DOI: 10.3390/wevj9020022 (see pp. 15, 16).
- [101] Brand, M. J., Schmidt, P. A., Zaeh, M. F., and Jossen, A.: *Welding techniques for battery cells and resulting electrical contact resistances*. In: *Journal of Energy Storage* 1 (2015), pp. 7–14. ISSN: 2352152X. DOI: 10.1016/j.est.2015.04.001 (see pp. 15, 16).
- [102] Brand, M. J., Kolp, E. I., Berg, P., Bach, T., Schmidt, P., and Jossen, A.: *Electrical resistances of soldered battery cell connections*. In: *Journal of Energy Storage* 12 (2017), pp. 45–54. ISSN: 2352152X. DOI: 10.1016/j.est.2017.03.019 (see pp. 15, 16, 29).
- [103] Brand, M. J., Berg, P., Kolp, E. I., Bach, T., Schmidt, P., and Jossen, A.: *Detachable electrical connection of battery cells by press contacts*. In: *Journal of Energy Storage* 8 (2016), pp. 69–77. ISSN: 2352152X. DOI: 10.1016/j.est.2016.09.011 (see p. 15).
- [104] Invenox: *Fortschrittliche Technologie für Lithium-Ionen-Batteriesysteme*. 2023. URL: <https://www.invenox.de/technologie/> (visited on 03/04/2024) (see p. 15).
- [105] Lee, S. S., Kim, T. H., Hu, S. J., Cai, W. W., and Abell, J. A.: “Joining Technologies for Automotive Lithium-Ion Battery Manufacturing: A Review.” In: *ASME 2010 International Manufacturing Science and Engineering Conference, Volume 1*. ASMEDC, 2010, pp. 541–549. ISBN: 978-0-7918-4946-0. DOI: 10.1115/MSEC2010-34168 (see pp. 15, 16).
- [106] Humpston, G. and Jacobson, D. M.: *Principles of soldering*. Materials Park Ohio: ASM International, 2004. ISBN: 0871707926 (see p. 16).
- [107] Schwartz, M.: *Soldering: Understanding the Basics*. Materials Park: A S M International, 2014. ISBN: 1627080589. URL: <https://ebookcentral.proquest.com/lib/kxp/detail.action?docID=3002481> (see p. 16).
- [108] Eikelboom, D., Bultman, J. H., Schonecker, A., Meuwissen, M., van den Nieuwenhof, M., and Meier, D. L.: “Conductive adhesives for low-stress interconnection of thin back-contact solar cells.” In: *Conference Record of the Twenty-Ninth IEEE Photovoltaic Specialists Conference, 2002*. IEEE, 2002, pp. 403–406. ISBN: 0-7803-7471-1. DOI: 10.1109/PVSC.2002.1190544 (see p. 16).
- [109] Zhou, Y., Gorman, P., Tan, W., and Ely, K. J.: *Weldability of thin sheet metals during small-scale resistance spot welding using an alternating-current supply*. In: *Journal of Electronic Materials* 29.9 (2000), pp. 1090–1099. ISSN: 0361-5235. DOI: 10.1007/s11664-004-0270-z (see p. 16).

- [110] Zhang, H. and Senkara, J.: *Resistance Welding*. CRC Press, 2011. ISBN: 9781466556416. DOI: 10.1201/b11752 (see p. 16).
- [111] Dickinson, DW and Franklin, JE and Stanya, A and others: *Characterization of spot welding behavior by dynamic electrical parameter monitoring*. Vol. 6. 59. *Welding Journal*, 1980 (see p. 16).
- [112] Han, Z., Orozco J, Indacochea, J. E., and Chen, C. H.: *Resistance spot welding: a heat transfer study*. Vol. 9. 68. *Welding Journal*, 1989 (see p. 16).
- [113] Gould, J. E.: *An examination of nugget development during spot welding, using both experimental and analytical techniques*. 66th ed. 1. *Welding Journal*, 1987 (see p. 16).
- [114] Olson, D. L.: *ASM handbook, volume 6: welding, brazing, and soldering*. ASM International, 1993 (see p. 16).
- [115] Shawn Lee, S., Hyung Kim, T., Jack Hu, S., Cai, W. W., Abell, J. A., and Li, J.: *Characterization of Joint Quality in Ultrasonic Welding of Battery Tabs*. In: *Journal of Manufacturing Science and Engineering* 135.2 (2013). ISSN: 1087-1357. DOI: 10.1115/1.4023364 (see p. 16).
- [116] Mostafavi, S., Hesser, D. F., and Markert, B.: *Effect of process parameters on the interface temperature in ultrasonic aluminum wire bonding*. In: *Journal of Manufacturing Processes* 36 (2018), pp. 104–114. ISSN: 15266125. DOI: 10.1016/j.jmapro.2018.09.020 (see p. 16).
- [117] Timsit, S.: “Electrical contact resistance: properties of stationary interfaces.” In: *Electrical Contacts - 1998. Proceedings of the Forty-Fourth IEEE Holm Conference on Electrical Contacts (Cat. No.98CB36238)*. IEEE, 1998, pp. 1–19. ISBN: 0-7803-4925-3. DOI: 10.1109/HOLM.1998.722422 (see p. 16).
- [118] Choi, S., Fuhlbrigge, T., and Nidamarthi, S.: “Vibration analysis in robotic ultrasonic welding for battery assembly.” In: *2012 IEEE International Conference on Automation Science and Engineering (CASE)*. IEEE, 2012, pp. 550–554. ISBN: 978-1-4673-0430-6. DOI: 10.1109/CoASE.2012.6386349 (see p. 16).
- [119] Katayama, S.: *Fundamentals and Details of Laser Welding*. Singapore: Springer Singapore, 2020. ISBN: 978-981-15-7932-5. DOI: 10.1007/978-981-15-7933-2 (see p. 16).
- [120] Steen, W. M. and Mazumder, J.: *Laser Material Processing*. London: Springer London, 2010. ISBN: 978-1-84996-061-8. DOI: 10.1007/978-1-84996-062-5 (see p. 16).
- [121] Kick, M. K., Kuermeier, A., Stadter, C., and Zaeh, M. F.: *Weld Seam Trajectory Planning Using Generative Adversarial Networks*. In: *Towards Sustainable Customization: Bridging Smart Products and Manufacturing Systems*. Ed. by A.-L. Andersen, R. Andersen, T. D. Brunoe, M. S. S. Larsen, K. Nielsen, A. Napoleone, and S. Kjeldgaard. Lecture Notes in Mechanical Engineering. Cham: Springer International Publishing, 2022, pp. 407–414. ISBN: 978-3-030-90699-3. DOI: 10.1007/978-3-030-90700-6₄₆ (see p. 16).
- [122] Grabmann, S., Mayr, L., Kick, M. K., and Zaeh, M. F.: *Enhancing laser-based contacting of aluminum current collector foils for the production of lithium-ion batteries using a nanosecond pulsed fiber laser*. In: *Procedia CIRP* 111 (2022), pp. 778–783. ISSN: 22128271. DOI: 10.1016/j.procir.2022.08.127 (see p. 16).
- [123] Grabmann, S., Kick, M. K., Geiger, C., Harst, F., Bachmann, A., and Zaeh, M. F.: *Toward the flexible production of large-format lithium-ion batteries using laser-based cell-internal contacting*. In: *Journal of Laser Applications* 34.4 (2022). ISSN: 1042-346X. DOI: 10.2351/7.0000778 (see p. 16).

- [124] Bruen, T., Marco, J., and Gama, M.: “Current Variation in Parallelized Energy Storage Systems.” In: *2014 IEEE Vehicle Power and Propulsion Conference (VPPC)*. IEEE, 2014, pp. 1–6. ISBN: 978-1-4799-6783-4. DOI: 10.1109/VPPC.2014.7007040 (see p. 17).
- [125] Bruen, T. and Marco, J.: *Modelling and experimental evaluation of parallel connected lithium ion cells for an electric vehicle battery system*. In: *Journal of Power Sources* 310 (2016), pp. 91–101. ISSN: 03787753. DOI: 10.1016/j.jpowsour.2016.01.001 (see pp. 17, 18).
- [126] Fill, A., Schmidt, T., Mader, T., Llorente, R., Avdyli, A., Mulder, B., and Birke, K. P.: *Influence of cell parameter differences and dynamic current stresses on the current distribution within parallel-connected lithium-ion cells*. In: *Journal of Energy Storage* 32 (2020), p. 101929. ISSN: 2352152X. DOI: 10.1016/j.est.2020.101929 (see pp. 17, 18).
- [127] Grün, T., Stella, K., and Wollersheim, O.: *Influence of circuit design on load distribution and performance of parallel-connected Lithium ion cells for photovoltaic home storage systems*. In: *Journal of Energy Storage* 17 (2018), pp. 367–382. ISSN: 2352152X. DOI: 10.1016/j.est.2018.03.010 (see pp. 17, 18).
- [128] Hunt, I., Zhang, T., Patel, Y., Marinescu, M., Purkayastha, R., Kovacik, P., Walus, S., Swiatek, A., and Offer, G. J.: *The Effect of Current Inhomogeneity on the Performance and Degradation of Li-S Batteries*. In: *Journal of The Electrochemical Society* 165.1 (2018), A6073–A6080. ISSN: 0013-4651. DOI: 10.1149/2.0141801jes (see pp. 17, 18).
- [129] An, F., Huang, J., Wang, C., Li, Z., Zhang, J., Wang, S., and Li, P.: *Cell sorting for parallel lithium-ion battery systems: Evaluation based on an electric circuit model*. In: *Journal of Energy Storage* 6 (2016), pp. 195–203. ISSN: 2352152X. DOI: 10.1016/j.est.2016.04.007 (see pp. 17, 18).
- [130] Dubarry, M., Devie, A., and Liaw, B. Y.: *Cell-balancing currents in parallel strings of a battery system*. In: *Journal of Power Sources* 321 (2016), pp. 36–46. ISSN: 03787753. DOI: 10.1016/j.jpowsour.2016.04.125 (see pp. 17, 18).
- [131] Gong, X., Xiong, R., and Mi, C. C.: *Study of the Characteristics of Battery Packs in Electric Vehicles With Parallel-Connected Lithium-Ion Battery Cells*. In: *IEEE Transactions on Industry Applications* 51.2 (2015), pp. 1872–1879. ISSN: 0093-9994. DOI: 10.1109/TIA.2014.2345951 (see pp. 17, 18).
- [132] Pan, Y., Feng, X., Zhang, M., Han, X., Lu, L., and Ouyang, M.: *Internal short circuit detection for lithium-ion battery pack with parallel-series hybrid connections*. In: *Journal of Cleaner Production* 255 (2020), p. 120277. ISSN: 09596526. DOI: 10.1016/j.jclepro.2020.120277 (see pp. 17, 18).
- [133] Zhang, Y., Zheng, J., Lin, S., Bai, F., Tanveer, W. H., Cha, S., Wu, X., and Feng, W.: *Nonuniform current distribution within parallel-connected batteries*. In: *International Journal of Energy Research* 42.8 (2018), pp. 2835–2844. ISSN: 0363907X. DOI: 10.1002/er.4039 (see p. 17).
- [134] Hofmann, M. H.: *Current distribution in parallel-connected battery cells*. Dissertation. München: Universitätsbibliothek der TU München, 2020 (see p. 17).
- [135] Chang, L., Ma, C., Zhang, Y., Li, H., and Xiao, L.: *Experimental assessment of the discharge characteristics of multi-type retired lithium-ion batteries in parallel for echelon utilization*. In: *Journal of Energy Storage* 55 (2022), p. 105539. ISSN: 2352152X. DOI: 10.1016/j.est.2022.105539 (see p. 18).

- [136] Mussa, A. S., Klett, M., Lindbergh, G., and Lindström, R. W.: *Effects of external pressure on the performance and ageing of single-layer lithium-ion pouch cells*. In: *Journal of Power Sources* 385 (2018), pp. 18–26. ISSN: 03787753. DOI: 10.1016/j.jpowsour.2018.03.020 (see p. 18).
- [137] Li, R., Li, W., Singh, A., Ren, D., Hou, Z., and Ouyang, M.: *Effect of external pressure and internal stress on battery performance and lifespan*. In: *Energy Storage Materials* 52 (2022), pp. 395–429. ISSN: 24058297. DOI: 10.1016/j.ensm.2022.07.034 (see p. 18).
- [138] Diao, W., Pecht, M., and Liu, T.: *Management of imbalances in parallel-connected lithium-ion battery packs*. In: *Journal of Energy Storage* 24 (2019), p. 100781. ISSN: 2352152X. DOI: 10.1016/j.est.2019.100781 (see p. 18).
- [139] Luan, C., Ma, C., Wang, C., Chang, L., Xiao, L., Yu, Z., and Li, H.: *Influence of the connection topology on the performance of lithium-ion battery pack under cell-to-cell parameters variations*. In: *Journal of Energy Storage* 41 (2021), p. 102896. ISSN: 2352152X. DOI: 10.1016/j.est.2021.102896 (see p. 18).
- [140] Schindler, M., Durdel, A., Sturm, J., Jocher, P., and Jossen, A.: *On the Impact of Internal Cross-Linking and Connection Properties on the Current Distribution in Lithium-Ion Battery Modules*. In: *Journal of The Electrochemical Society* 167.12 (2020), p. 120542. ISSN: 0013-4651. DOI: 10.1149/1945-7111/abad6b (see p. 18).
- [141] Chang, L., Wang, C., Zhang, C., Xiao, L., Cui, N., Li, H., and Qiu, J.: *A novel fast capacity estimation method based on current curves of parallel-connected cells for retired lithium-ion batteries in second-use applications*. In: *Journal of Power Sources* 459 (2020), p. 227901. ISSN: 03787753. DOI: 10.1016/j.jpowsour.2020.227901 (see p. 18).
- [142] Fill, A., Schmidt, T., Mader, T., Llorente, R., Avdyli, A., and Birke, K. P.: *New semi-analytical model approach of the current distribution within parallel-connected lithium-ion cells*. In: *Journal of Energy Storage* 40 (2021), p. 102653. ISSN: 2352152X. DOI: 10.1016/j.est.2021.102653 (see p. 18).
- [143] Kakimoto, N. and Goto, K.: *Capacity-Fading Model of Lithium-Ion Battery Applicable to Multicell Storage Systems*. In: *IEEE Transactions on Sustainable Energy* 7.1 (2016), pp. 108–117. ISSN: 1949-3029. DOI: 10.1109/TSTE.2015.2476476 (see p. 18).
- [144] Huynh, P.-L.: *Beitrag zur Bewertung des Gesundheitszustands von Traktionsbatterien in Elektrofahrzeugen*. Wiesbaden: Springer Fachmedien Wiesbaden, 2016. ISBN: 978-3-658-16561-1. DOI: 10.1007/978-3-658-16562-8 (see p. 18).
- [145] Schuster, S. F., Bach, T., Fleder, E., Müller, J., Brand, M., Sextl, G., and Jossen, A.: *Nonlinear aging characteristics of lithium-ion cells under different operational conditions*. In: *Journal of Energy Storage* 1 (2015), pp. 44–53. ISSN: 2352152X. DOI: 10.1016/j.est.2015.05.003 (see p. 18).
- [146] Schmitz, P.: *Elektrische Verbindung von zylindrischen Lithium-Ionen-Zellen zur Herstellung von Energiespeichersystemen*. Dissertation. München: Universitätsbibliothek der TU München, 2019 (see p. 19).
- [147] Holm, R.: *Electric Contacts*. Berlin, Heidelberg: Springer Berlin Heidelberg, 1967. ISBN: 978-3-642-05708-3. DOI: 10.1007/978-3-662-06688-1 (see p. 20).
- [148] Euler, J. and Nonnenmacher, W.: *Stromverteilung in porösen elektroden*. In: *Electrochimica Acta* 2.4 (1960), pp. 268–286. ISSN: 00134686. DOI: 10.1016/0013-4686(60)80025-4 (see pp. 21–23, 109).

-
- [149] Schmidt, P.: *Laserstrahlschweißen elektrischer Kontakte von Lithium-Ionen-Batterien in Elektro- und Hybridfahrzeugen*. Dissertation. München: Universitätsbibliothek der TU München, 2015 (see p. 23).
- [150] Vycital, V., Ptacek, M., Toman, P., and Topolánek, D.: “Earthing system resistance calculation using analytical approach with mutual coefficients.” In: *2017 18th International Scientific Conference on Electric Power Engineering (EPE)*. IEEE, 2017, pp. 1–6. ISBN: 978-1-5090-6406-9. DOI: 10.1109/EPE.2017.7967333 (see p. 25).
- [151] Choi, Y. and Humphrey, J. A.: *Analytical prediction of two-dimensional potential flow due to fixed vortices in a rectangular domain*. In: *Journal of Computational Physics* 56.1 (1984), pp. 15–27. ISSN: 00219991. DOI: 10.1016/0021-9991(84)90080-9 (see p. 25).
- [152] Griffiths, D. J.: *Introduction to electrodynamics*. Fourth edition. Cambridge et al.: Cambridge University Press, 2017. ISBN: 978-1-108-42041-9. DOI: 10.1017/9781108333511 (see p. 25).
- [153] Toupin, R. A.: *Saint-Venant’s Principle*. In: *Archive for Rational Mechanics and Analysis* 18.2 (1965), pp. 83–96. ISSN: 0003-9527. DOI: 10.1007/BF00282253 (see p. 25).
- [154] Love, A. E. H.: *A treatise on the mathematical theory of elasticity*. 4. ed., unabridged and unaltered republ. of the 4. (1927) ed. Dover classics of science and mathematics. New York: Dover Publications, 1990. ISBN: 9780486601748 (see p. 25).

List of Figures

1.1	Share of sales of new passenger vehicles according to the electrical energy sources. a) worldwide sales between 2010 and 2022. b) vehicle sales in Norway, Germany, the European Union, China, the United States, and worldwide for 2022. Data based on [7].	1
1.2	Worldwide battery demand and mobility share between 2020 and a prognosis up to 2030. Data based on [9].	2
1.3	Structure and overview of this thesis.	5
2.1	Example of a parallel connection. a) np connection within round cells, defined as an external parallel connection. b) electrode stack with parallel connection inside a pouch cell defined as internal parallel connection.	10
2.2	Influence of the OCV on the current distribution and resulting SoC difference for different cell technologies. All measurements are carried out at 0.5 C and 25 °C. Subfigures a), b) and c) show the voltage during CC charging. The resulting differential potential is plotted in subfigures d) e) and f). The resulting SoC differences at an inhomogeneous contact resistance in the order of about $R_{c,2} = 5 \text{ m}\Omega$ are plotted in subfigures g), h) and i). The measurements are carried out with the VPC, which is explained in Chapter 2.4.2.	13
2.3	Current distribution of 2p connection measured with a conventional test-bench and the virtual parallel connection (VPC). Between two full cycles, the cells were recontacted, and the current distribution was measured to determine the influence of recontacting. The cells are resistance welded to hilumin stripes. In the conventional test-bench these are clamped between two copper clamps. Conventional test-bench was used by [134] and is explained briefly in Fig. 2 in Chapter 4. Subfigure a) shows the current distribution cells during CC charging at 0.5 C and 25 °C. Exemplary, the influence of a faulty contact is shown. Subfigure b) presents a detail-view within the first 100 s.	17
2.4	Schematic view of a cylindrical cell with a cell connection. For the measurement of the electrical contact resistance, the cell connection is transformed into a representative replacement sample. The resistance over the lap joint consists of the sum of R_A , R_B and R_C . The figure is based on [146].	19
2.5	ECM of the LTspice simulation with two specimens, A and B, according to Figure 2.4. Each welded line is represented by a contact path, r_c .	20
2.6	Graphical analysis of the current distribution in area-based connections. The analytical solution of Euler and Nonnenmacher [148] and the reciprocal, with $k = 10\,000$, show the ratio of R_{LJ} to R_C . Contact resistances in the order of $R_C < 0.01 \cdot R_A$ results in an almost ideal parallel circuit, i.e., the ratio of R_{LJ}/R_A approaches 0.5. In contrast, contact resistance in the order of $R_C > 0.4 \cdot R_A$, both theoretical methods approach the asymptote and a linear relationship results.	23

2.7 Influence of the current injection on the equipotential lines via an FEM simulation. The current was injected at $x=7.5$ mm and $y=2$ mm. a) Top view of the sample, including the electric equipotential lines. Around the current injection point, an inhomogeneity results. b) Resulting theoretical potential through a horizontal line at the sample at 7.5 mm and a comparison considering a linear potential drop. c) Relative error between the theoretical and the linear voltage curve normalized to the longest side length of the specimen's contact area (A). Figure is based on the publication presented in Chapter 3 [14]. 24

2.8 Schematic of the VPC within a n -channel battery cyclers. Channel x corresponds to the master and is current-controlled. All other $n - 1$ channels are voltage-controlled. The figure is based on the publication presented in Chapter 4 [15]. 26

List of Tables

2.1	Specifications of the investigated cells. The measurements were carried out at 25 °C; resistance measurements were taken at 50 % SoC.	8
2.2	Current distribution according to the connection in Figure 2.5. The simulation was carried out with LTspice, and three cases were considered.	21